Microvascular models for cerebral malaria and vascular inflammation

Caitlin Howard

A dissertation

submitted in partial fulfillment of the

requirements for the degree of

Doctor of Philosophy

University of Washington

2022

Reading Committee:

Ying Zheng, Chair

Joseph Smith

Andy Shih

Program Authorized to Offer Degree:

Bioengineering

University of Washington

Abstract

Microvascular models for cerebral malaria and vascular inflammation

Caitlin Howard

Chair of the Supervisory Committee:

Ying Zheng

Department of Bioengineering

More than 90% of all malaria mortality is from infection with *Plasmodium falciparum*. Severe cases of *P. falciparum* infection can progress to cerebral malaria which is characterized by infected red blood cells sequestering in microvessels in the brain accompanied by endothelial cell dysfunction, vascular leakage, and cerebral inflammation. Microvasculature plays a key role in the progression of cerebral malaria but the specific factors which initiate progression to severe disease are not well understood, in large part because of challenges in studying the disease due to the inaccessibility of the brain and a lack of suitable models. Recent advances in vascular engineering have allowed for the development of models of vascular systems which have great potential to overcome previous challenges in studying brain microvasculature. The body of work presented here reports advances in vascular engineering strategies to create more

biologically relevant models and applications of these models to address specific questions in the pathogenesis of cerebral malaria. We first established a method for engineering capillary-scale vasculature using a combination of soft lithography and 2-photon laser-based ablation. Because infected red blood cells sequester primarily in capillaries and post-capillary venules in the brain, replicating this size scale was important and allowed for the study of the spatiotemporal dynamics of normal and infected red blood cells as they travel through a capillary. This study helped to shed light on some of the mechanisms involved in infected red blood cell sequestration and also demonstrated the feasibility of the platform for use to study other hematologic diseases. Next, we expanded on these engineering methods to develop models of complex, organ-specific microvasculature. To do this, we optimized the ablation protocol for use with various extracellular matrix components, endothelial cell and perivascular cell types, and complex 3D geometries at anatomic scale. We verified that ablation is compatible with multiple matrices and cell types and as a proof-of-concept created an endothelialized glomerulus model at anatomic scale. The ability to create perfusable vessels with significant geometric complexity at the capillary scale enables new approaches to the study of vascular biology and can provide more biologically relevant models for probing microvascular questions. We next adapted a microvascular model to use for studying the response of brain endothelial cells to various pathological stimuli implicated in cerebral malaria pathogenesis. From this, we were able to demonstrate that infected red blood cells adhere to brain endothelial cells in the microvessel model and continue to mature *in situ* throughout the blood stage parasite life cycle. This allowed us to probe the endothelial cell response at various stages of parasite maturation and highlighted that the infected

red blood cells induced unique changes to the brain endothelial cells. We also investigated how this response is affected by previous exposure to host pro-inflammatory cytokine TNFα which revealed a strong combinatorial effect from both stimuli. Because the microvessel model is perfusable, we were able to assess an immune function of the endothelial cells by perfusing with leukocytes and determined a strong functional change in the ability of parasite-stimulated endothelial cells to recruit leukocytes. This study provided new mechanistic insights into endothelial cell dysfunction in cerebral malaria. Altogether, this work introduces advances in vascular engineering allowing for more biologically relevant models of vascular disease and facilitating progress towards understanding the mechanisms of cerebral malaria pathogenesis and brain inflammatory processes.

TABLE OF CONTENTS

LIST OF FIGURES

ACKNOWLEDGMENTS

This work could not have been done without the help and support of many people. First, I would like to thank my advisor Dr. Ying Zheng for her mentorship and guidance throughout my PhD. She has always maintained enthusiasm and positivity about science and encouraged me to try new things and not to fear failure. I am also grateful for the support from Dr. Joe Smith. He has provided excellent scientific mentorship and thorough feedback which has greatly helped shape this work.

I am also immensely appreciative of the members of the Zheng lab for cultivating a supportive and positive environment throughout my graduate career. Thank you to Sam Rayner, Christian Mandrycky, Russ Whelan, Chris Arakawa, and Celina Gunnarsson for being excellent senior lab members; I learned so much from you all. Thank you to Nicole Zeinstra, Yu Jung Shin, Kira Evitts, and Ariana Frey for being helpful, motivating, and encouraging graduate students to work and spend time with.

I am extremely grateful for my friends in the BIOE graduate student community, especially Sarah Saxton, Colleen O'Connor, Emily Olszewski, and Audrey Olshefsky. I could not have made it to the end without your support. You all inspire me and I am so proud to have gone on this journey with you all.

Finally, I am forever thankful for my family and friends. Thank you to my best friends Clare Demer, Marghi Demer, and Willy Fines for all the support, even while across the country. My mom Kelly Howard and sister Emily Howard have been my lifelong greatest supporters; thank you for all the love and encouragement. I couldn't have done it without you all.

Chapter 1. ORGAN-ON-A-CHIP SYSTEMS FOR VASCULAR BIOLOGY

Parts of this chapter are adapted from the following manuscript: Mandrycky C, **Howard C**, et al. "Organ-on-a-chip systems for vascular biology." J Mol Cell Cardiol, 2021[1].

1.1. ENGINEERING VASCULAR SYSTEMS

Vasculature is the universal tissue infrastructure, known for providing nutrients, taking away waste, maintaining homeostasis, and shaping tissue and organ structure. In the developing embryo, a group of vascular progenitors, known as angioblasts, emerge to differentiate and assemble into a primitive vascular network[2–4]. As development proceeds, this primitive network remodels, presumably triggered by changes in hemodynamic forces[5,6], surrounding cell types, and microenvironment, including chemical factors and architectural features of surrounding extracellular matrix, to establish a hierarchical vascular tree with tissue-specific functionality important for the function of each organ[7,8]. The process of de novo vascular formation is known as vasculogenesis, whereas remodeling and vascular growth from pre-existing vasculature, either by sprouting or intussusception[9], has been defined as angiogenesis. Modern evidence has shown that blood vessels also provide instructive regulatory signals to surrounding non-vascular target cells[8,10]. Building vascular models and vascularized tissues has been a major thrust in biomedical research in recent decades for understanding vascular biology, regenerating tissue, modeling diseases, and testing preclinical drugs.

Among various biomedical efforts, organ-on-a-chip (OOC) technologies have gained significant research attention in recent years, with the more specific target of designing and engineering miniaturized functional units of human tissues and organs[11–13]. These miniaturized devices promise to better replicate native biological functions ex vivo and enable high-throughput techniques essential to disease modeling and drug testing. Central to this approach is the use of perfusable micro- and milli-fluidic platforms in which fluid flow both sustains the metabolic needs of OOC devices and replicates the distinct vascular compartment found in living organisms. In this review we explore recent advances in OOC technologies with a focus on this vascular component and technologies for replicating vascular structure and function in vivo. We will briefly review vascular structure and function, highlighting OOC systems that have advanced our understanding of fundamental aspects of vascular biology. We then explore OOC systems that utilize an engineered vasculature to explore tissue level functions in organ-specific models. We conclude with prospective remarks on choosing OOC systems of varying complexity and including proper cell populations to target suitable vascular biology questions.

1.2. VASCULATURE: HETEROGENOUS STRUCTURE, CELL POPULATIONS AND BLOOD FLOW

Blood vessels are organized in a hierarchical branching network in three-dimensional (3D) space and characterized by diameters ranging from arteries and veins (1 mm to 1 cm for large vessels, and 100 μm to 1 mm for small vessels), to arterioles and venules (20–100 μm) and capillaries (5–20 μm). The curvature of vessels ranges from 10^{-3} to 10^{2} mm^{-1} with the largest vessel curvature found in the microvasculature of complex vascular beds like the brain[14]. Variation in size and curvature corresponds to the difference in

vessel wall composition and blood flow, leading to heterogeneous biophysical forces on the vessel walls. As the innermost layer of cells on the vessel wall, endothelial cells also have distinct identities in arteries, veins, large and small vessels and different vascular beds in various organs to support diverse vascular function and tissue demands[15–18]. Oxygenated blood is carried in arteries and arterioles, whereas deoxygenated blood drains into venules and veins. A continuous endothelial cell layer in high density capillary networks supports the high metabolic demand of organs such as the heart and brain, whereas a fenestrated endothelium allows for filtration, secretion, and reabsorption of small molecules in kidney and guts. Sinusoidal or discontinuous endothelia are critical to support macromolecular and cellular trafficking functions in liver, bone marrow and spleen[19–22]. The endothelium provides critical signals to construct a specific vascular microenvironment and instruct organ development and maturation[8,10]. The organ-specific microenvironment (i.e. cytokines, metabolites, biophysical signals, and direct cell-cell contact from parenchyma cells) simultaneously interacts with ECs to induce unique EC functions[23]. Heterogeneity therefore is an important part of vascularization that needs to be considered for recapitulating specific tissue and organ function and may be used for promoting tissue regeneration.

1.2.1. Hemodynamics: a critical driver for vascular formation

A central process in vascular biology is sensing blood flow. Once a vascular network forms, blood flow induces mechanical stimuli that is constantly sensed by the vasculature, driving vascular growth and remodeling. As blood flows over the endothelial surface, its viscosity generates shear forces in the direction of flow. Simultaneously, pressure within the blood vessel generates a force normal to the surface of endothelial cells causing the

vessel to stretch. Vessels with different size, identity (i.e., artery, vein, or capillary), or in different organs often have different characteristic pressure and shear stress levels. Changes to shear stress level have been associated with vascular pathologies for decades, with regions of altered blood flow near vessel bends and bifurcations frequently acting as sites for atherosclerotic plaque growth or aneurysm development[24].

Endothelial cells sense these biophysical cues through a variety of mechanosensory mechanisms[25]. Numerous EC mechanosenors for wall shear stress (WSS) have been identified, including the junctional complex specific to endothelial cells consisting of VE-Cadherin, VEGFR2, and PECAM1[24,26–29]. Additional mechanosensitive complexes include G proteins, ion channels, integrins, and NOTCH1[30–35], which can be activated by WSS to induce downstream signaling to modulate vascular tone, barrier function, and proliferation. In addition to WSS magnitude, endothelial mechanosensors can also be activated by flow patterns. Physiological laminar flow activates the expression of transcription factor Krüppel-like factor (KLF2) and nuclear factor (erythroid-derived 2)-like (NRF2), and downstream anti-inflammatory pathways. Disturbed flow inhibits KLF2 and NRF2 activation and activates pro-inflammatory pathways, leading to an atheroprone phenotype[25,30]. Recapitulating the diverse flow conditions found in vivo in engineered vascular models may be key to better understanding the physiologically heterogeneous vascular response to flow mediated conditions.

Blood flow plays a key role in regulating essential endothelial functions, including the release of nitric oxide for paracrine signaling[36] and endothelial barrier function[37]. These

endothelial responses are often intimately tied to the function of perivascular cells and parenchymal tissues. Thus, the studies of vascular biology and vascular support of parenchymal function requires fine control over biophysical and biochemical processes. OOC technologies are uniquely suited to pursuing these questions as they enable control of flow parameters that are difficult to study in vivo and let researchers specify and explore the types and interactions of endothelial cells with different parenchymal populations. In this review, we will investigate these applications of OOC devices to different aspects of vascular biology, from the discovery of fundamental endothelial mechanisms to the engineering of multi-organ models health and disease.

1.2.2. Flow systems – vascular development and biology

Blood flow is a key driver for the proper vascular growth and remodeling. The study of the hemodynamic response of vessels has been focused in two areas: endothelial cell sensing of flow and network expansion via angiogenesis. Different model systems have been developed in these two distinct areas.

Flow chambers have been designed to model laminar or disturbed flow profiles and study the flow responses of cultured endothelial cell monolayers[24,26,27,38–40]. Endothelial cells respond to flow with cytoskeletal remodeling and cellular alignment in the direction of flow, changes in adherens junction complexes, and changes in gene expression and cell proliferation[27,40]. With sustained physiological shear stress under laminar flow, endothelial cells undergo elongation and alignment, strengthened adherens junctions, and lower permeability. When exposed to disturbed flow, often defined as a flow separation or recirculation with higher or lower than physiological wall shear stress, endothelial cells experience rounding, weakened adherens junctions, higher permeability, and increased

proliferation and proinflammatory expression[38,40]. Similarly, in response to defined circumferential strain endothelial cells experience cytoskeletal remodeling leading to actin stress fiber orientation perpendicular to the stretch axis[41]. Physiological circumferential strain is associated with matrix remodeling, angiogenesis, growth factor secretion, and integrin engagement[25].

The state of the art of engineering models for the study of endothelial cell responses to flow have been limited in parallel plate flow chambers, 2D substrate assays, and deformable rubber membranes for many years. Parallel plate flow chambers are 2D systems which allow for a monolayer of endothelial cells to be exposed to a defined flow allowing for the effective study of WSS on the endothelium[42,43]. Additionally, endothelial cells cultured on 2D substrates and transwell plates have been used for evaluating endothelial cell function in basic mechanistic studies[24]. To investigate circumferential strain, deformable rubber membranes have been used to apply a defined strain to a monolayer of endothelial cells[25]. These simplified models have been crucial for understanding the endothelial cell response to mechanical forces. However, endothelial cells in arteries, veins, and microvasculature experience different levels of WSS, blood flow profiles, and pressure. Additionally, there are differences in metabolic demand and transport needs across different organ systems leading to specialized endothelial cell and vascular structure and function in different vascular beds[44–46]. Thus there are significant limitations in simple flow chambers due to the lack of a physiological 3D structure, lack of tissue-specific extracellular matrix and stromal support cells, and the lack of complex flow characteristics, all of which lead to a failure to fully recapitulate the microvascular niche.

In the body, the blood vessels bend and twist through 3D space with varying levels of curvature and torsion (i.e. deviation of curvature from its osculating plane). Small vessels with low flow and high curvature and torsion have been associated with heterogeneous vascular modeling, which remains not well studied. The response of ECs to flow has been binned into either laminar or disturbed flow, which however represent the two extremes of the wide spectrum of flow profiles found throughout the vasculature. To bridge the gap and understand the flow response in small vessels with 3D curvature in a laminar flow regime, our group has recently developed a spiral microvessel system with precisely controlled diameter, curvature and torsion in 3D space (Figure 1.1)[47]. We showed small spiral vessels in laminar flow regions induced distinct changes in EC phenotype and transcriptional profiles compared to conventionally defined laminar flow in straight vessels. This new engineering model expand the control over 3D geometrical parameters to better mimic vascular structure in vivo and accurately understand the effect of 3D curvature on vascular biology. The results also point to potential flow mediated mechanism of heterogeneous vascular development and remodeling.

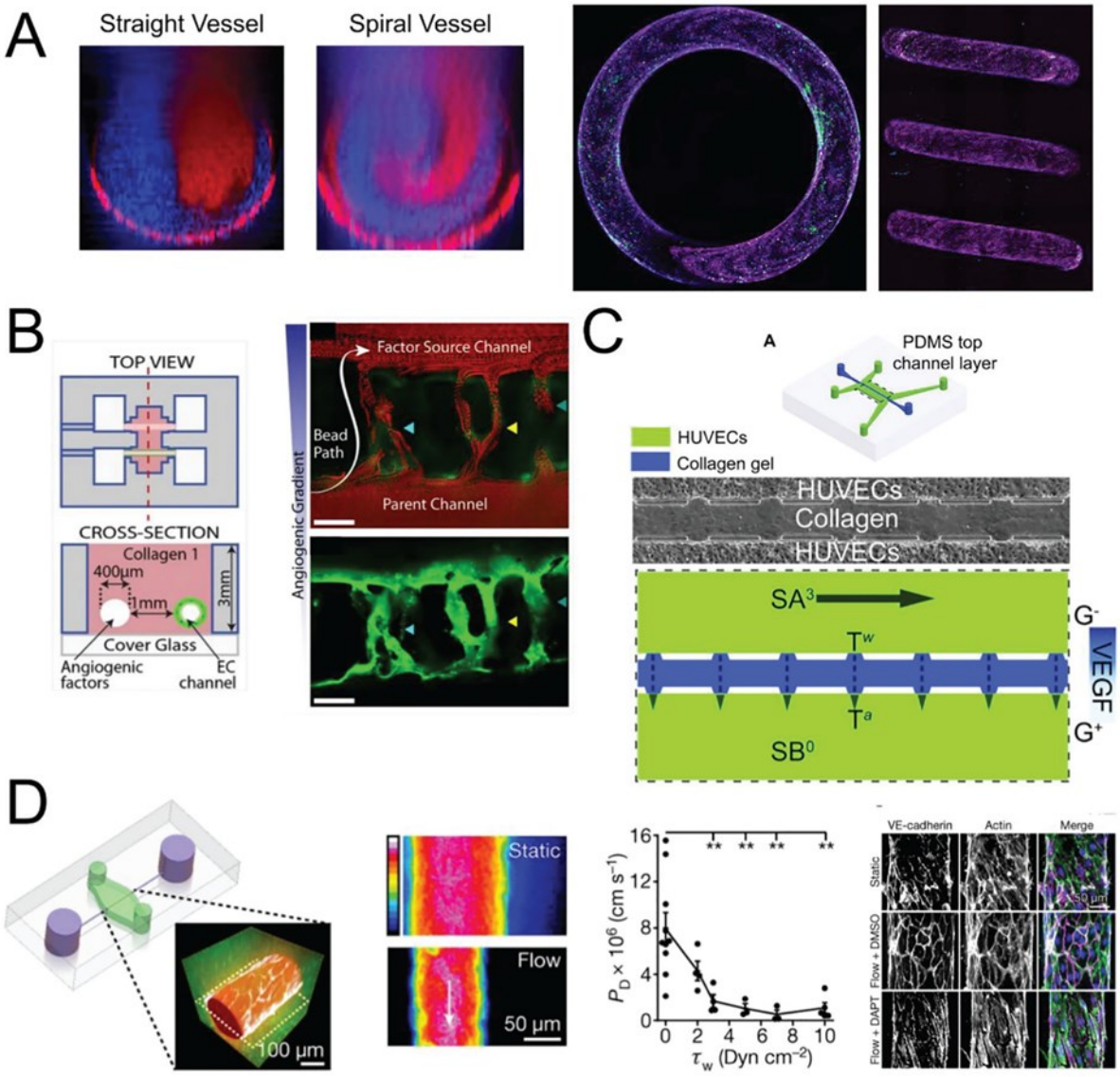

Figure 1.1 Engineering biophysical and biochemical cues in OOCs.

(A) The flow in curved geometries is characterized by secondary flows and mixing not seen in straight vessels (left) and its effect can be studied in endothelialized spiral vessels (right, VECAD, magenta; VWF, green, adapted from Mandrycky et al.[47]. (B) Endothelial cells cultured in channels can be stimulated by engineered biochemical gradients to stimulate angiogenesis and anastomosis to the factor source channel (adapted from Nguyen et al.[48]). (C) Biochemical gradients can be combined with defined biophysical forces in opposing channels to investigate the influence of shear stress and interstitial flow differences on sprouting into collagen hydrogels (adapted from Song and Munn[49]). (D) Perfusion vascularized channels leads to a decrease in vascular permeability with increasing shear stress that can be disrupted using the γ-secretase inhibitor DAPT (adapted from Polacheck et al.[50]).

1.2.3. Flow mediated sprouting angiogenesis and barrier function

Vascular networks expand through angiogenesis to establish hierarchical structure. This directed expansion of the vasculature is a critical process in normal development and wound healing, as well as in tumor progression[7]. Sprouting angiogenesis starts when ECs branch off of an existing blood vessel and extend into an avascular space, often motivated by the presence of specific chemical gradients in the tissue (e.g. VEGF)[51]. The sprouts are known to be led by a specialized “tip” cell EC, which migrates forward while trailing “stalk” cells proliferate to maintain a continuous lumen as the new vessel lengthens[52]. Much of this process has been observed in model organisms such as zebrafish and rodent models. Most engineering models have focused on biochemical factors that drive sprouting of an endothelial cell monolayer into ECM hydrogels[53,54]. The development of flow-mediated vascular model, however, is essential for a complete understanding of the underlying mechanisms and for the investigation of new therapeutic approaches. Given this, a wide variety of OOC systems have been developed for investigating angiogenesis[53–57]. Key to these designs is the patterning of an initial parent vessel, which is often achieved through casting of hydrogel around a removable mold (e.g. an acupuncture needle[55]) or carefully designed microfluidics devices where the hydrogel is confined to the space between two independently perfused channels[56]. For example, Nguyen and colleagues utilized needle subtraction method to generate two independent channels in a collagen hydrogel to study sprouting angiogenesis[48]. By seeding one channel with endothelial cells and perfusing angiogenic factors (HGF, bFGF, MCP-1, VEGF, S1P, and PMA) through the other channel to create a chemokine gradient they induced angiogenic sprouting (Figure 1.1B). The formation and maturation of these sprouts appeared to follow the mechanics of what has been observed in vivo,

representing a powerful testbed for further study of the molecular mechanisms of angiogenesis.

Other OOC models of angiogenesis have been developed to further investigate the biomechanical and biochemical regulators of angiogenesis[57,58]. Song and Munn developed a microfluidic system and showed that fluid forces can regulate angiogenesis[49]. They seeded endothelial cells into two microfluidic channels separated by a block of collagen gel and established a VEGF gradient across the two channels to stimulate EC sprouting (Figure 1.1C). They found that high shear stress attenuated VEGF induced sprouting through nitric oxide signaling and that interstitial flow through the collagen gel stimulated sprouting. This interstitial flow finding has also been replicated in additional OOC models[59]. Flow has been shown to regulate the production of matrix-metalloproteinase 1, which is an important factor for angiogenic sprouting[60]. In addition to sprouting, the use of cell-remodelable matrices provides important features for assessing vessel barrier function. For example, using single microvessel tubes, NOTCH signaling has been shown to be regulated by WSS, and further regulate vascular barrier function (Figure 1.1D)[50], promote arterial gene expression[61], and maintain junctional integrity and suppress proliferation[62].

Together, this new generation of 3D vascular microfluidic models enables the control of input flow, vessel geometry in 3D space, vessel network structure, leading to fine control of flow magnitude, flow profiles, and pressure in individual branches and networks and better recapitulation of conditions in vivo. These advances would allow for the studies of individual contribution of flow parameters in step wise fashion, to uncover new cellular behaviors and gene regulations in in vivo like vascular microenvironment. These new

models could also be used to test effects of isolated components of signaling pathways through stimulating or inhibiting (by activators, knockdowns, or cleavage methods) specific regulators and subjecting them to identical mechanical stimuli. Incorporating these new OOC technologies would provide new insights into core aspects of vascular biology at each of the stages of vessel formation and expansion, from individual cells, to lumens, and connected networks.

1.3. PATTERNING PERFUSABLE MICROVASCULAR NETWORKS – VASCULAR AND TISSUE FUNCTIONS

Beyond the fundamental study of vascular biology itself, introducing vasculature into OOC systems is critical for the development of functional tissue and the study of biologic processes including vascular-parenchymal and blood-vessel interactions[63]. Perfusion through the vasculature is necessary for the nutritional support of parenchymal tissue, with tissues generally needing to be located within a few hundred microns of a vascular lumen[64]. In addition to transport and hemodynamic-related phenomenon, vascular cells themselves guide the development and behavior of parenchymal and perivascular cells and are intimately involved in biological processes like inflammation, hemostasis, and wound healing[65–67]. The function of organs such as the heart, kidney, lungs, liver, or spleen is dependent on continuous perfusion, which is required for truly modeling the behavior of such organs.

An ideal vascularized OOC would include precise three-dimensional cellular arrangement, high vascular density, close apposition of vasculature and parenchyma, organ-specific function, cell-remodelable extracellular matrix materials, in vivo-like hemodynamics, hierarchical and multicellular blood vessels, and multiple organ-specific

cell types. Current OOC systems generally focus on a limited number of these features and achieving them all simultaneously remains an outstanding challenge for the field. Various patterning techniques have been used to generate perfusable vasculature. The prepatterned approach involves the creation of hollow lumens within a bulk material followed by the introduction of endothelial cells. Methods for prepatterning vascular channels in OOC systems range from relatively planar microfluidic approaches, to lithographic or molding approaches within cell-remodelable hydrogels, to direct-writing strategies with full 3D control such as 3D printing or laser degradation[68,69].

1.3.1. PDMS based microvascular structure

Microfluidic approaches to modeling a vascularized organ generally involve casting a biologically inert material such as polydimethylsiloxane (PDMS) over a micromachined mold with raised features, and then removing and bonding it to a glass surface or another piece of PDMS to create hollow channels. Such approaches are exemplified by the landmark design of Huh et al., consisting of two rectangular channels cast in PDMS and separated by a porous PDMS membrane[70,71]. Seeding vascular cells into one chamber and parenchymal cells into the other allows observation of transport phenomena and interactions at the tissue interface, with additional vacuum chambers on either side allowing the application of cyclical stretch/strain to mimic biological forces (Figure 1.2A). Initially used to model a breathing lung, organ functions including surfactant production were demonstrated, and processes occurring at the vascular-parenchymal interface such as neutrophil adherence and diapedesis in response to inflammation were replicated[70]. Since this initial report, this technology has been used to emulate specific functions of numerous organs. Notable examples include an anaerobic human intestine-on-a-chip

replete with a complex bacterial microbiome and a human glomerulus-on-a-chip incorporating human glomerular endothelial cells[72] and human induced pluripotent stem cell-derived podocytes while demonstrating basic filtration function[73]. Connecting similar devices cultured with different organ-specific cells into a “body-on-a-chip” and automating cell culture and imaging was demonstrated recently, highlighting exciting future possibilities for monitoring organism-level processes[74].

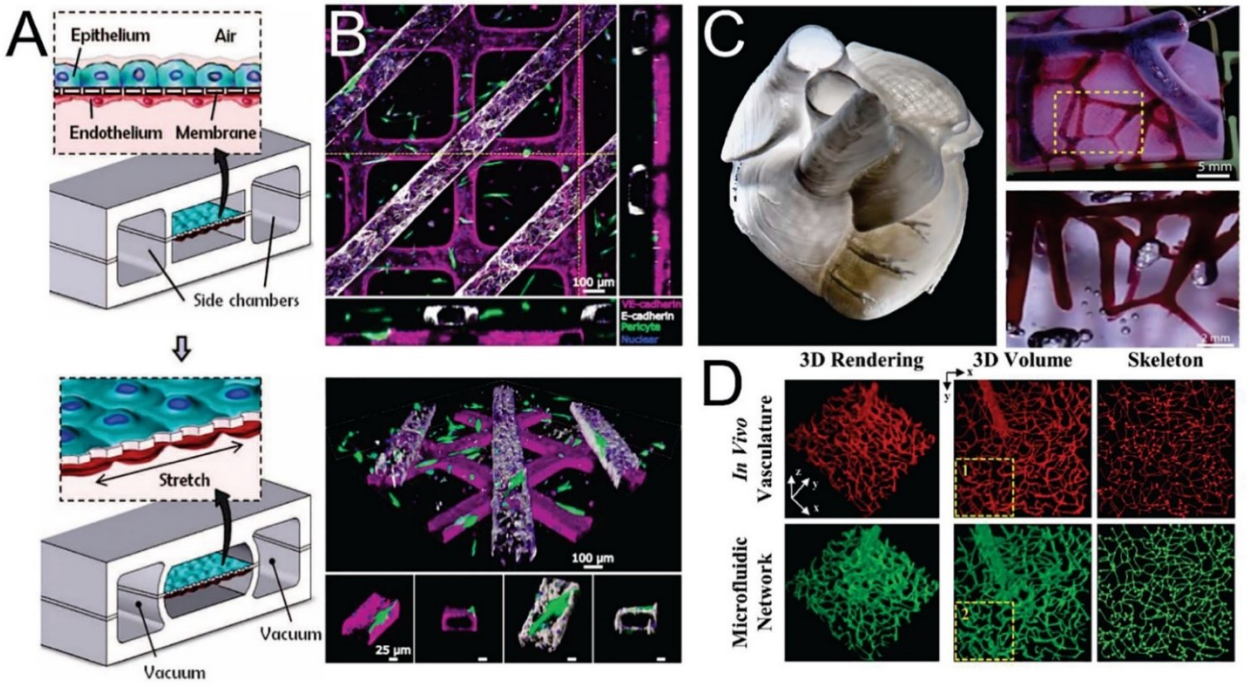

Figure 1.2 Strategies for vascularization of multicellular organ-on-a-chip platforms:

(A) A schematic for microfluidic-based approach to a vascularized lung-on-a-chip (adapted from Huh et al.[70]) (B) A human renal tubule on a chip created through soft lithography showing tubular channels overlying endothelial channels with flanking orthogonal views (top) and perspective views showing perivascular association with the vessel (bottom, adapted from Rayner et al.[75]). (C) A 3D human heart model bioprinted in collagen (left) with vessels perfused in red (top right) and highlighted area shown magnified (bottom right, adapted from Lee et al.[76]. (D) In vivo vasculature (top) was used to create a photomask for direct laser-writing of channels into a PEG-based hydrogel (bottom, adapted from Heintz et al[77]).

1.3.2. Hydrogel based microvascular structures

The PDMS based microfluidic devices often succeed at replicating specific tissue function, but are limited by their essentially planar nature, the use of non-biologic materials, and difficulty supporting multiple cell types. Lithographic and/or molding-based approaches within biologic hydrogels allow greater three-dimensionality, the opportunity to include cells in the bulk matrix material, and the ability for cells to remodel the surrounding matrix. These approaches generally have in common the use of a mold or sacrificial material around which matrix material is cast, with removal of the mold or sacrificial material then leading to channels that can be seeded with endothelial cells. One simple, yet effective, iteration of this is the use of thin needle as a mold which is removed following matrix gelation, resulting in vascular lumens within a bulk hydrogel. This approach has been used to study tissue phenomenon including the vascular invasion of pancreatic cancer[78].

Our lab has developed a technique to create geometrically complex engineered vessels by lithographically patterning PDMS molds and using them to imprint channels into liquid collagen hydrogels. Following collagen gelation PDMS molds are removed and patterned slabs are assembled against a flat piece of collagen to create rectangular lumens within a bulk hydrogel[79]. This approach has been used to model the bone marrow niche[80] and create implantable cardiac vascular patches[81]. By assembling two patterned collagen slabs across a thin collagen membrane and seeding top and bottom channels with renal tubular epithelial and endothelial cells, respectively, this approach was used to emulate the human renal vascular-tubular unit (Figure 1.2B). Incorporated cells secreted basement membrane components, remodeled the collagen membrane into an ~1 μm

exchange interface, and supported blood perfusion and albumin resorption[75]. The Radisic group has also used a stacking approach to increase vascular density and generate thick, multilayered cardiac constructs[82].

Bioprinting approaches offer the potential for full 3D control and precise cellular placement. Bioprinting can either involve the construction of sacrificial networks that leave lumens within cellularized hydrogel upon dissolution, or the direct deposition of vascular and parenchymal tissues. The intermediate step of creating sacrificial molds is appealing given the technical challenge of accurately direct-writing living cells within soft matrix materials. Using this approach, a 3D-printed dissolvable carbohydrate lattice was used to vascularize thick, cellularized Poly(ethylene glycol) (PEG)-based hydrogels, supporting the function of embedded hepatocytes[83]. Printing with a pluronic (PEO-poly(propylene)-PEO)-based ink was used to create a 3D vascularized proximal renal tubule with separate tubular and vascular channels within an engineered extracellular matrix material. This construct was shown to model both renal transport and pathophysiology related to a diseased (hyperglycemic) conditions[84]. In a recent breakthrough, direct-writing of collagen within a supportive hydrogel bath was used to bioprint a vascularized and contractile model 3D human heart with ~20 μm resolution (Figure 1.2C) [76]. Finally, an emerging related strategy is the use of subtractive patterning through direct laser-writing within hydrogels. Computer-controlled multiphoton manufacturing can pattern tissues with submicron resolution and offers the opportunity to create capillary-scale vascular beds in biologic hydrogels– a scale that is difficult to achieve with bioprinting approaches. This approach has been used to re-create human capillary geometries with PEG-based hydrogels (Figure 1.2D)[77]. While direct cell seeding cannot reliably be performed at the

capillary scale, we have had success creating cellularized capillaries by ablating capillary-sized lumens (5–10 μm) extending from a larger cellularized vessels (100–300 μm) and applying a pressure gradient to encourage migration[85]. This technology has the potential to address current challenges in creating large scale vascularized and functional tissues, which is also an ongoing effort in our lab.

1.3.3. Microvasculature for studying blood-vessel interactions

Perfusable microvessels have been useful in understanding blood vessel interactions[79,86–88], particularly in small vessels that are extremely challenging to study in vivo due to imaging constraints and structural heterogeneity. For example, we have developed microvessels with a 13 × 13 grid network in collagen hydrogel gel[79]. This large grid structure provides large range of flow velocity and wall shear stress that recapitulate both health and disease. In acute inflammation and activation, endothelia from these microvessels have been found to release von Willebrand Factor (VWF), a glycoprotein essential to hemostasis which assembles into thick fibers and 3D complex meshes under flow (Figure 1.3A)[89]. These VWF fibers appear to serve as binding reservoirs for blood cells including platelets, leukocytes, and red blood cells (RBCs). In the absence of ADAMTS13, an enzyme known to cleave VWF in normal blood, this led to vascular occlusion. The same microvessel format has been adapted to study *P. falciparum*-infected RBC interactions with primary brain endothelium[90]. This work found that iRBCs binding to the endothelium is strongly influenced by the flow shear stress and different parasite binding variants displayed different shear-dependent binding characteristics to the endothelium.

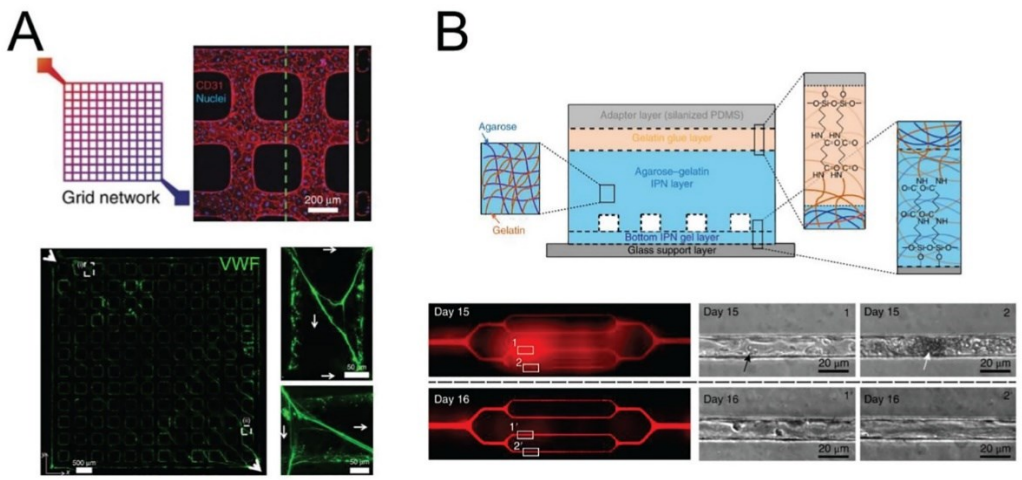

Figure 1.3 Blood-endothelial interactions in organ-on-a-chip systems.

(A) Lithographically patterned endothelialized grid networks release VWF (green) when stimulated, which form complex fiber meshes under perfusion (adapted from Zheng et al. [89]). (B) High concentrations of irreversibly sickled red blood cells perfused through patterned microvascular networks in agarose-gelatin hydrogels cause occlusions and increase vascular permeability ("Day 15") that can be recovered within 24 h with continuous perfusion (adapted from Qiu et al.[86]).

Together, these prepatterned microvessels offer full control of perfusion and vascular geometry with a large range of diameter and network complexity. These precise controls provide means to study the contribution of individual factors in a stepwise fashion and further develop potential therapies for various microvascular and blood diseases. Replicating high-density vascular networks with perfusion is crucial for the next level of tissue regeneration and the generation of functional vasculature. These pre-patterning tools could also be combined with vascular self-assembly and organoid technologies to build fully hierarchical vascular network with cellular renewal and remodeling potential.

1.3.4. Vascularized cardiac and organ-specific tissues

As the most metabolically active organ in the body, the heart requires significant vascular density to support efficient nutrient delivery. Hence, proper vascularization has been a key requirement towards engineering thick and functional cardiac constructs. Prior efforts

to vascularize cardiac grafts have often relied on the self-assembly of ECs to form connected tubes within cardiac constructs using primary ECs (e.g. HUVECs) or ECs differentiated from pluripotent stem cells[81,92]. The presence of these vessels has been found to improve cardiomyocyte maturation and tissue function; however, the formed networks lack perfusion, preventing large scale construct fabrication and culture. Following implantation, the self-assembled vessels frequently regress and the grafts, though integrated with the host, showed insufficient perfusion. Recent developments by our group and others have shown that perfusable vessels can support cardiac tissue survival both in vitro and in vivo[81,82,93].

To support organ-specific tissue and chip designs, a variety of endothelial populations have been used. Organ-specific ECs in OOC devices are often primary cells isolated from healthy or diseased donors, but stem cell differentiation protocols have enabled the generation of these cells from hPSCs. In addition to the heart, these include brain vascular cells in models of the blood brain barrier[94], tubule and glomerular ECs in models of the kidney[95,96], pulmonary ECs in models of the lung[70], and sinusoidal ECs in models of the liver[97,98]. However, some cells such as liver sinusoidal ECs have an unstable phenotype in vitro, and HUVECs are still predominantly used in liver-specific OOC devices[99,100]. These EC populations in combination with other organ-specific cell types from both primary and hPSC-derived sources have been used to improve the function and maturation of organ-specific OOC devices (Table 1).

Table 1.1 Cell types commonly used in organ specific OOC systems

Organ System	Endothelial cell types	Secondary cell types
Heart	HUVECs[82,93], hiPSC-ECs[81]	Cardiomyocytes and fibroblasts[101,102]
Brain	Brain microvascular endothelial cells[103,104], hiPSC-ECs[105]	Pericytes, astrocytes[103]
Kidney	Glomerular[84,95] and peritubular microvascular endothelial cells[106]	Podocytes[95], proximal tubule epithelial cells[84]
Lung	Pulmonary microvascular endothelial cells[70]	Alveolar epithelial cells[70], bronchial epithelial cells[107]
Liver	HUVECs[99,100], Liver sinusoidal endothelial cells[97,98]	Hepatocytes[97–99], stellate cells[97,99], Kupffer cells[97,100]

1.4. Future directions – choosing biomechanical, biochemical, and cellular complexity

OOC devices have been applied to a wide range of research questions, spanning basic endothelial biology to disease modeling and drug discovery. Essential to these approaches is the extent to which different vascular features and compartments are modeled and the tailoring of device designs to the research question at hand. In the slow progression from simple to complex models, simplified systems targeting only some biophysical or biochemical cues have provided great insight into core aspects of

endothelial biology. Laminar flow chambers, for example, have revealed fundamental mechanisms of endothelial mechanotransduction. Similarly, cell-in-gel OOCs provided new insights into the mechanisms of angiogenesis and potential strategies to induce vascular growth (or inhibit it in the case of tumorigenesis) in living or engineered tissues. In totality, however, these works as well as a variety of in vivo studies have demonstrated a wide range of factors which may influence vascular function. Recent work has increasingly reinforced the concept of vascular heterogeneity, going beyond long appreciated organ-specific or vessel-size-specific identities. Single cell transcriptomics have recently been used to identify at least 6 distinct endothelial cell types within the mouse brain[108]. Determining which populations are most important to incorporate into a given OOC device will be critical and depend on the study goals. Developing highly accurate tissue OOCs for disease modeling and drug testing, for example, may be sensitive to the presence of the full complement of native vascular phenotypes.

The question of what level of complexity to model extends beyond the varieties of endothelial cells to include. Recent work by our lab and others have highlighted additional levels of heterogeneity in the vasculature resulting from differences in hemodynamic factors. Laminar fluid flows with secondary flow characteristics can induce unique transcriptional profiles in endothelial cells[47]. This finding suggests the complex 3D geometries found in the native vasculature may lead to more diverse endothelial responses to flow than were previously thought. The functional consequences of these differences and their role in health and disease, if any, remain an open question which OOC systems are poised to provide new insight into. In addition, blood flow is pulsatile, and the pulsatility introduces temporal accelerations and decelerations which can

combine with complex 3D vascular architectures to yield a continuum of complex flows. How these flows translate to vascular function is an intense area of research, particularly in hemodynamically sensitive pathologies like cerebral aneurysms[109]. On the other hand, many critical vascular phenomena occur at the smallest vessels – capillaries of 5–10 μm, which scale remains an engineering limit since most existing OOC technologies have resolution at the order of 100 μm or more. The development of robust capillary scale engineered vessels has enabled new investigations into the dynamics of vascular interactions like those between malaria infected red blood cells and endothelial cells when exposed to controlled flow. The inclusion of these capillary structures in OOC platforms may be crucial for studies of vascular interactions with different blood components, including altered RBCs, immune cells, platelets, and others. In these capillary vessels, the blood cells and blood vessels are of nearly the same caliber. Such close interactions may contribute to disease progression and their modulation may be core to a variety of therapeutic approaches.

There are several additional important elements in constructing appropriate organ-on-a-chip devices. One is to recapitulate the extracellular matrix (ECM) microenvironment that is found in vivo. ECM has a complex composition and function and is a regulator of vascular and tissue functions. Unlike in vivo, many OOC designs have used very simplified ECM forms. Endothelial cells are highly sensitive to different matrix molecules and the composition of the endothelial basement membrane is a mediator in the process of vascular growth and angiogenesis[110]. Hydrogels from decellularized extracellular matrices (dECM) have been developed to add back some of this biological complexity and create more organ-specific microenvironments[111]. We have previously shown that

kidney dECM promotes kidney microvascular EC maturation and quiescence, supporting the need for carefully considered matrices in engineered systems[112]. The heterogeneous matrix microenvironment of site-specific ECMs, however, remains challenging to fully replicate. Future development in ECM protein design and spatial patterning would provide new tools to better model vascular and tissue functions.

Another important element is the original source of cells. Cell lines or isolated primary cells have so far been the predominant cell source in OOCs, but advances in stem cell technology have made a greater variety of cell types available to researchers. As a result, the prospect of patient-specific OOC systems populated with cells differentiated from patient-derived stem cells for applications in precision medicine has become more tenable[113,114]. Protocols for the differentiation of the many different endothelial subtypes are not yet available[115], but recent advances in vascular organoids[116] suggest renewable sources of these cells may be on the horizon. Incorporating these patient-derived cells into disease modeling OOC may provide new insight into the mechanisms of disease and the safety and efficacy of new therapeutic approaches.

In addition, blood proteins and cellular components would be crucial to incorporate in OOCs to optimize the culture system. We have recently shown that platelet rich plasma significantly enhanced vessel barrier and improve endothelial cell metabolism towards maturation[117]. These blood-derived components could be an alternative to replace current growth media and further improve OOCs. The incorporation of these components also enables the study of blood-endothelial interactions in healthy and diseased conditions. It appears that engineered microvessels have minimal interactions with normal human blood, suggesting normal vascular function. These perfusable vascular networks could

be appropriate platforms for stepwise investigations of the interactions of various blood, cell, and protein components with the vessel wall during vascular activation, blood disorders, and even infectious disease progression.

In summary, existing vascular engineering technologies allow us to build vasculatures over the full range of diameters, curvatures, and potentially densities of blood vessels found in living organisms. Incorporating those technologies into a single engineered system encompassing the entire range of structures and cell types, however, remains an immense outstanding challenge. It is then important to define the goal of research projects, and wisely choose the appropriate OOC for approaching biological questions as well as drug and disease modeling. This approach has proven fruitful, but future advances are poised to further add to OOC device complexity and their ability to accurately replicate human physiology to gain a deeper understanding of vascular biology and to serve as powerful testbeds for modeling diseases and developing novel therapeutics.

Chapter 2. BIOENGINEERING 3D MICROVESSELS FOR INVESTIGATING *PLASMODIUM FALCIPARUM* PATHOGENESIS

Parts of this chapter are adapted from the following manuscript: Bernabeu M, **Howard C**, et al. "Bioengineering 3D Microvessels for Investigating *Plasmodium falciparum* Pathogenesis." Trends in Parasitology, 2021[118].

2.1. CEREBRAL MALARIA

Globally there were an estimated 241 million cases of malaria resulting in 627,000 deaths in 2020[119]. The majority of these deaths are caused by infection with *Plasmodium falciparum*, the deadliest species of human malaria parasites, which is responsible for an estimated 90% of all malaria deaths. However, most infections with *P. falciparum* do not lead to severe disease, and the differences between cases which result in recovery and cases which progress to severe disease are not well understood. In order to improve patient outcome, there is a need to identify the causes of progression to severe disease.

A severe complication of *P. falciparum* malaria is cerebral malaria (CM) which is defined clinically as having peripheral parasitemia and a coma without an explainable secondary cause[120]. A key feature of CM is the sequestration of infected red blood cells (iRBCs) in the capillaries and postcapillary venules of the brain[121]. Often associated with sequestered iRBCs are ring hemorrhages and coagulopathies, indicating vascular dysfunction[122,123]. These vascular abnormalities can lead to neurological complications including swelling of the brain which is likely a key feature leading to death. However, the mechanisms responsible for these vascular abnormalities are not completely understood.

Parasites sequester to host endothelial cells as a method to avoid splenic clearance through receptor-ligand interactions. Parasites remodel the erythrocyte membrane to include protrusions from the surface, called knobs, and the display of surface antigens such as *P. falciparum* erythrocyte membrane protein-1 (PfEMP1). PfEMP1 is encoded by a family of *var* genes in which one copy is expressed per cell. Each PfEMP1 contains binding domains which have different receptors on host endothelial cells including intercellular adhesion molecule 1 (ICAM-1) and endothelial protein C receptor (EPCR)[124–128].

Sequestration is thought to have an effect on cerebral vasculature due to a localized inflammatory response and direct interactions between parasites and the host. During infection, markers for endothelial cell activation including ICAM-1, V-CAM, and E-selectin are upregulated in patient plasma and on cerebral microvascular endothelium[129]. Some in vitro studies have demonstrated that iRBC binding alone can induce increased expression of ICAM-1 on brain endothelial cells[130]. Additionally, some studies have shown there is a reduction of EPCR and thrombomodulin on endothelial cells near sequestered iRBCs[125,131]. EPCR and thrombomodulin are two important receptors in the protein C pathway which functions as a regulator of inflammation, coagulation, and barrier function[132]. After iRBCs adhere to endothelial cells, they continue to mature and eventually rupture, releasing pro-inflammatory factors which are concentrated near endothelial cells and can lead to endothelial cell activation and barrier disruptions[120,133–135].

Together, there is evidence that iRBC sequestration, host inflammatory factors, dysregulated coagulation pathways, and parasite factors are all likely contributors in the

progression of CM. Much of what is known about CM comes from post-mortem autopsy studies and clinical studies using MRI and evaluating patient serum for various factors[120,122,126,136]. Due to the inaccessibility of the brain, studies on binding interactions of iRBCs and molecular pathways of disease have been challenging. Therefore there is a need to develop in vitro models which recapitulate the geometric constraints of native vasculature and the interactions between iRBCs and host endothelium.

2.2. The Interplay between *Plasmodium falciparum* and Blood Vessels

Malaria parasites have a complex and intimate relationship with blood vessels through multiple stages of their life cycle. Sporozoites are introduced into the human body via a mosquito bite into the dermis. Sporozoites migrate by gliding motility in the skin and traverse blood vessels to enter the blood circulation[137]. Once in the bloodstream, sporozoites travel to the liver, arrest, and cross the liver sinusoidal barrier to invade hepatocytes[138]. After undergoing asexual replication, hepatocyte-derived vesicles containing merozoites, known as merosomes, bud through endothelial cells[139] and are released into the blood circulation[140]. Merosomes become trapped in small blood vessels, such as lung capillaries[141], and are thought to release merozoites to initiate the blood stage of infection.

Malaria symptoms appear after repeated rounds of parasite replication in red blood cells (RBCs). Among the human malaria species, *P. falciparum* is unique for having highly cytoadhesive infected red blood cells (iRBCs) that bind to the endothelial lining of blood vessels and cause microvascular obstruction. Sequestration is thought to have evolved for iRBCs to avoid spleen-dependent clearance mechanisms and is associated with organ-specific complications when parasites reach high burdens. During the blood stage,

sexually committed gametocyte–iRBCs develop within the bone marrow sinuses before returning to the blood circulation for uptake within a new mosquito blood meal[142]. These multiple interactions with the vasculature reveal that *P. falciparum* has evolved a set of complex and sophisticated strategies in synergy with blood vessels and distinct microvascular niches. Although cytoadhesion is central to *P. falciparum* disease, animals are non-natural hosts for *P. falciparum* and may not be fully optimal for studying all endothelial binding interactions or organ niches. Novel vascular bioengineering approaches could provide new opportunities for studying *P. falciparum* and human vessel interactions in a more physiological way.

2.2.1. Vasculature: A Heterogeneous System

The blood circulatory system provides nutrients and oxygen to all tissues and takes away waste and metabolites for disposal. Blood vessels are organized in a hierarchical branching network, ranging in size from large-caliber arteries (from 100 μm to ≤ 1 cm internal diameter) to arterioles (15–100 μm) to a dense capillary plexus (4–12 μm) where transport interchange takes place. Deoxygenated blood drains into venules (10–100 μm) and veins (from 100 μm to ≤1 cm in diameter). These variations in blood vessel sizes correlate to variations in vascular wall composition, blood flow, and pressure, leading to heterogeneous biophysical forces on the vessel walls. In addition, the microvasculature in different organs has diverse functions to meet the unique demands of the tissue. Endothelial cells line the innermost layer of vessels and have heterogeneous phenotypes and functions to regulate the transport between the blood and the surrounding tissue. In dermis, heart, and brain, endothelium forms a continuous layer with low permeability, whereas endothelium in the kidneys is fenestrated to allow for filtration and reabsorption

of small solutes. Endothelial cells in liver, bone marrow, and spleen are sinusoidal and present large gaps in endothelial junctions that facilitate macromolecular and cell diffusion. These heterogeneous organ-specific vessels provide unique interactions with *P. falciparum* and facilitate different stages of the infection as the parasites enter the skin, move to the liver, and exploit multiple organ niches throughout the vascular system. To better understand *P. falciparum* pathogenesis, or how it progresses through its life cycle in humans, future research needs to take vascular heterogeneity into account.

The endothelium is a dynamic organ. It shifts from an anti-inflammatory and anticoagulant phenotype in health to a proadhesive, procoagulant, and complement-activating phenotype in response to infection and injury. Most malaria infections are asymptomatic, with low parasite burdens and limited vascular activation[143]. Only a subset of infections has high parasite burdens with extensive microvascular obstruction, widespread endothelial activation, and endothelial dysfunction. Although PfEMP1s encode diverse binding phenotypes, it is unknown whether the parasite cytoadhesion strategy adjusts to the differing microvascular environments in asymptomatic and symptomatic hosts. Hemodynamic forces are a major driver of endothelial cell phenotypes. Shear stress lowers vascular permeability, and the mechano-activated transcriptional programs, such as Kruppel-like factor 2 (KLF2), confer a barrier-strengthening, anti-inflammatory and antithrombotic phenotype on endothelial cells[144]. Flow forces have been categorized into laminar flow (where vessel geometry is linear, or with smooth curvature) and disturbed flow (where vessels bifurcate, have high curvature, or occurring after microvascular obstruction). Vessel geometry and microfluidic forces play an important role in thrombosis. For instance, vWF fibers preferentially form near vessel bifurcations, and

vWF assembly is influenced by 3D vessel architecture, fluid shear stress, and flow acceleration[89]. Exposure of 3D human microvessel models to physiological flow forces will enable us to study how microvascular endothelial cells respond to inflammatory, procoagulant, and hemodynamic forces, as well as to explore the progression to endothelial dysfunction in malaria.

2.2.2. Small Blood Vessels and P. falciparum Cytoadhesion

Cytoadherent asexual iRBCs predominantly sequester within small blood vessels with internal diameters smaller than 50 µm. *P. falciparum* exports proteins into the erythrocyte cytoplasm, and many of these proteins are involved in erythrocyte cytoskeletal modifications and induce knob-like cytoadhesive platforms on the RBC surface[145–147]. The main cytoadhesion ligand is *P. falciparum* erythrocyte membrane protein 1 (PfEMP1), encoded by a family of approximately 60 *var* genes per parasite genotype. PfEMP1 proteins are expressed in a mutually exclusive fashion and endow different binding properties to iRBCs[148]. The protein family is classified into three main groups (A, B, C) that encode distinct binding properties for CD36[149,150] endothelial protein C receptor (EPCR)[151,152], and intercellular adhesion molecule 1 (ICAM-1)[127,153]. CD36 and EPCR are mutually exclusive binding traits[148], and have ancient origins because they are also encoded in the related *var*-like gene family in the chimpanzee malaria parasite, Plasmodium reichenowi[154]. EPCR-binding PfEMP1 variants are enriched in severe malaria infections[155,156] and are linked to brain swelling in cerebral malaria (CM)[127,157], even though they represent only a minor subset of the PfEMP1 repertoire (~11–15%).

Besides controlling blood-tissue exchanges, endothelial cells have a major function in vascular hemostasis by maintaining an antithrombotic and anti-inflammatory surface[65].

Endothelial cells respond to inflammatory cytokines by upregulating procoagulant and proinflammatory pathways. The barrier properties of blood vessels are regulated by both barrier-disruptive and barrier-restorative signaling pathways[158]. Chronic activation or hyperinflammation can result in endothelial dysfunction, an alteration in endothelial state from a resting or 'calm' phenotype to a highly activated phenotype where it is unable to perform its normal functions. iRBCs in high parasite biomass are procoagulant and interfere with anticoagulant pathways. Sequestered iRBCs release products that activate endothelial cells and induce barrier disruption in endothelial cell monolayers[159,160]. They also interfere with EPCR function, which normally counteracts coagulation and induces anti-inflammatory and barrier-restorative pathways in endothelial cells[152,161]. Moreover, in vitro assays provide evidence that products released by schizont-stage *P. falciparum*–iRBCs interact with thrombin to prolong barrier disruption in endothelial cell monolayers[162,163]. A better understanding of how endothelial cells integrate inflammatory signals may guide new approaches to treat endothelial dysfunction and vascular leak in severe malaria.

2.2.3. The Blood–Brain Barrier and CM Pathology

The blood–brain barrier (BBB) presents the lowest permeability coefficient in the human vasculature and is thus essential to preserve brain function. Brain microvascular endothelial cells present a strong barrier phenotype, which is accomplished by elevated expression of tight junction proteins, low levels of transcytosis, and controlled traffic of molecules through specific efflux pumps and solute transporters. The unique properties of the BBB are acquired by its structure and interactions with brain parenchyma cells[164]. Brain pericytes are thought to contribute to the mechanical stability of the capillary wall[165].

In addition, astrocytic end-feet contact and support the vascular bed and secrete factors that enhance the expression of endothelial tight junction proteins, such as claudin-5 and occludin, and specific transporters, such as glucose transporter-1 (GLUT-1) (Figure 2.1) [166]. The key role of the BBB in maintaining brain function makes cerebral microvasculature a highly pathogenic site of sequestration.

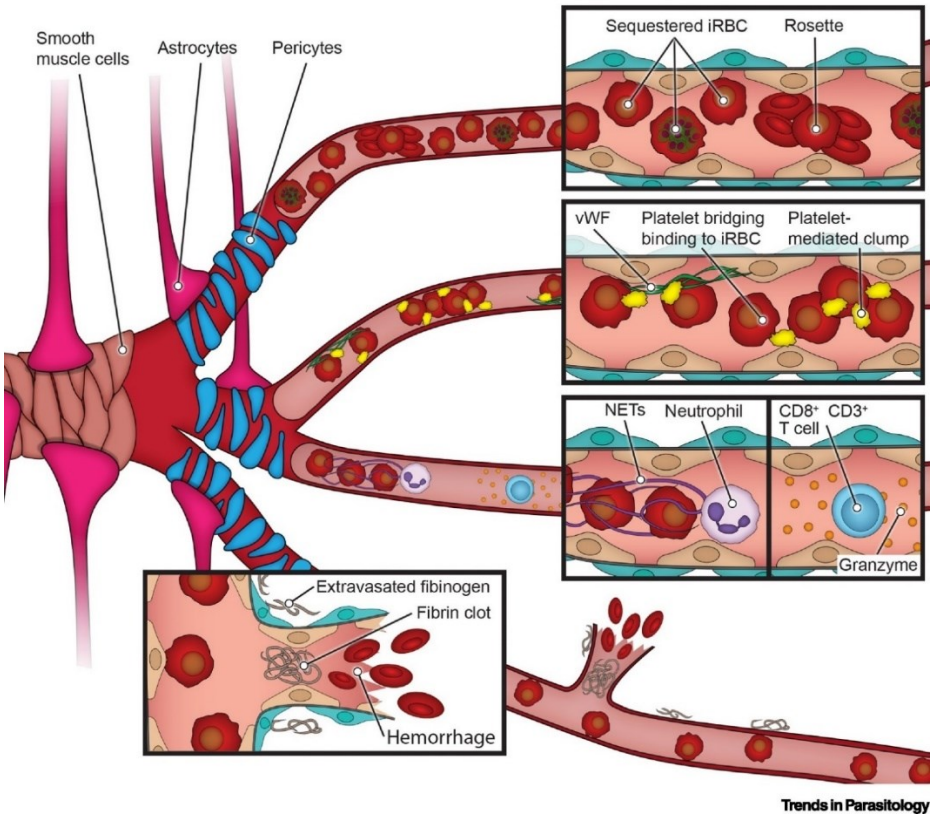

Figure 2.1 Pathogenesis of Cerebral Malaria (CM).

The unique properties of the blood–brain barrier (BBB) are achieved through interactions between endothelial cells, perivascular cells (smooth muscle cells in larger vessels and pericytes in the microvasculature), and astrocytes. *Plasmodium falciparum* sequestration in the brain microvasculature is a hallmark of CM and contributes to microvascular

obstruction, probably along with 'rosettes' – aggregates of infected red blood cells (iRBCs) and uninfected red blood cells. In autopsy studies, BBB disruption is exemplified by ring hemorrhages or fibrinogen deposition in the extravascular space. Platelets might also contribute to CM pathogenesis by bridging between iRBCs and von Willebrand factor (vWF) or endothelium, or causing platelet-mediated iRBC clumps. Other cell types implicated in disease complications are neutrophils and CD8+ T cells. These pathogenic findings are sometimes localized in distinct regions of the brain, such as the white and gray matter[167]. Abbreviation: NETs, neutrophil extracellular traps.

Our knowledge of CM has been acquired through examination of autopsy samples and, more recently, through neuroimaging studies. Magnetic resonance imaging (MRI) has indicated that severe brain swelling is associated with fatality in pediatric CM[123]. Although the pathophysiological changes leading to brain swelling in CM are incompletely understood, venous congestion and vascular engorgement are common findings, and MRI has found strong evidence for vasogenic edema in children[168,169]. Brain swelling also occurs in adult CM, although at milder levels[170,171]. Fatality in adults has been recently associated with severe hypoxia, which might be triggered by *P. falciparum* microvascular obstruction[170]. In both children and adults, the neurovascular pathology on MRI is compatible with posterior reversible encephalopathy syndrome (PRES), a neurological disorder that is characterized by vasogenic edema and endothelial dysfunction, including breakdown of the BBB. PRES is reversible, and survivors recover from brain swelling in 48–72 h[168,169].

Histological examination of pediatric brain autopsies has confirmed evidence of BBB breakdown. Fatal pediatric CM cases are divided into two groups: dense sequestration

only (CM1) and dense sequestration accompanied by extraerythrocytic pigment, ring hemorrhages, and evidence of systemic activation of coagulation (CM2)[172,173]. Both groups have fibrinogen leakage to brain parenchyma, indicating BBB breakdown (Figure 2.1)[172,174]. In addition, high levels of extracellular histones and plasma cell-free DNA are associated with brain swelling on MRI[134,175]. Accumulation of iRBCs is common in both white and gray matter of the brain. Sequestration is highest in capillary beds or marginalized in postcapillary venules[174,176]. The same pattern is evident in retinal imaging, with higher accumulation in smaller vessels and on the venular side of circulation (small venules > postcapillary venules > large venules > precapillary arterioles > small arterioles > large arterioles)[177]. This pattern may arise in part because cells experience deacceleration and lower shear stress as they exit the capillaries into the larger postcapillary venule spaces. Collectively, these findings suggest interactions between sequestration, coagulation, and BBB dysregulation in CM, albeit the extent of brain coagulopathy varies in fatal cases.

Both CM1 and CM2 cases show perivascular brain activation and pathology, including myelin damage in cortex, subcortex, white matter, and brain stem, and reactive astrocytes in all brain regions except the cortex[172]. Ring hemorrhages are concentrated in the white matter and watershed areas where blood supply is decreased. It has been hypothesized that biophysical and biological components may account for these brain regional differences[167,178]. White-matter vasculature presents longer and less ramified small blood vessels and is more prone to upstream occlusive damage. By comparison, gray-matter small vessels are organized in a dense and sponge-like network with multiple anastomosis and collateral pathways, which might prevent local increase in flow

resistance after occlusion and hemorrhages[174]. In addition, it has been hypothesized that differences in perivascular cell composition might account for different responses between white and gray matter that could confer diverse barrier properties or influence the localized response to sequestered iRBCs (reviewed in[167]).

2.3. Host Response and CM Pathogenesis

A procoagulant and hyperinflammatory host response might additionally contribute to vascular dysfunction in CM patients. For example, fibrin deposits are common in pediatric brain autopsies upstream of ring hemorrhages (Figure 2.1). Moreover, low circulating platelet levels have been linked to fatal brain swelling in pediatric CM[157]. Whereas thrombocytopenia might have multiple systemic causes, platelet accumulation in the brain vasculature might have pathogenic consequences[179,180]. Platelets have both immunogenic and procoagulant functions, which might lead to a dual protective or damaging effect on blood vessels. Activated platelets secrete proinflammatory cytokines, including tumor necrosis factor alpha (TNF-α)[181], transforming growth factor (TGF)-β1, and interleukin-1β (IL-1β)[182], that enhance the local inflammatory milieu. They also release microparticles that potentially inhibit parasite growth[183]. Platelets can bridge the binding of iRBCs without tropism to the brain endothelium[184] and may promote microvascular obstruction by platelet-mediated clumping of iRBCs[185] or iRBC binding to platelet–von Willebrand Factor (vWF) multimers secreted upon endothelial activation or injury[186] (Figure 2.1).

2.3.1. Organ-Specific P. falciparum-iRBC Cytoadhesion

Children who die from CM have massive sequestration of iRBCs in the brain, but also in the vasculature of the gastrointestinal tract and/or subcutaneous adipose tissue of the

skin. Other sites of sequestration include the heart, lung, spleen, and, to a lesser extent, the kidney[187]. Despite evidence of a broad sequestration[187], parasite tropism for most organ/vascular sites remains terra incognito.

2.4. Engineered 3D Microvessels: Advantages of a Versatile System and Applications in Malaria Pathogenesis Research

2.4.1. Controlled Vessel Size and Geometry

The fabrication of 3D microvessel networks is not limited to previously published 13 × 13 grids or parallel channels connected by capillary-size vessels. The combination of soft lithography, injection molding, and laser photoablation allows the design of custom-made geometries. This provides control of vessel length and diameter, number of branches, branching angle, and vessel curvature. The 3D microvessel network will determine microfluidic properties which regulate (i) endothelial cell phenotype, including gene expression and transcriptional profile, and (ii) how blood cells interact with the vessel wall. These systems can be used to study parasite sequestration in engineered blood vessels that precisely mimic the shape and curvature of natural organ-specific microvessels, as well as to explore how vessel geometry might determine parasite-mediated vascular damage.

2.4.2. Fabrication of Organ-Specific Cell Types and Vasculature

These fabrication technologies support the growth and development of new vascular-specific microvasculature models, including human kidney fenestrated peritubular microvascular endothelial cells[106] or even models that combine two microfluidic networks, an endothelial and an epithelial, that recapitulate the vascular–tubular renal interface in the kidney[75]. Additionally, patient-specific cells can be used, either primary cells or iPSC-

differentiated cells. This offers controlled experimental conditions to study parasite–vessel tropism and investigate disease mechanisms leading to specific endothelial damage in different regions of the brain or in other organs.

2.4.3. Controlled Perfusion of Blood Components

Attaching the 3D microvessel network into a flow pump allows for precise control of biological and biomechanical parameters in a step-wise fashion. For example, different blood cells or molecules (e.g., cytokines, clotting factors, patient blood samples) can be perfused independently, sequentially, or in combination at controlled microfluidic conditions to dissect how human or *P. falciparum* factors contribute to severe disease, individually or in synergy.

2.4.4. Modeling P. falciparum Cytoadhesion in Vitro

The factors that determine iRBC–organ sequestration patterns are incompletely understood. The simplest assay and workhorse for investigating parasite binding is the static cytoadhesion assay[149,153]. In this assay, iRBCs settle on cells or spotted proteins and then are gently washed. This technique has the significant advantage that it is easy to implement, even in a low-tech field research setting, and therefore has seen abundant usage for characterizing receptor and endothelium-specific interactions[188–191]. For instance, this approach has shown that the same parasite variants can bind to primary human brain, lung, and heart microvascular endothelial cells[192]. However, a major disadvantage is that this assay mostly measures the strength of iRBC attachment during washing steps and provides limited insights into iRBC capture from flow and other flow-based considerations that may be important for vascular tropism. To account for this limitation, flow-based microfluidic systems have been applied[193,194]. While much more

difficult to implement in a field setting, a recent study using commercial linear flow chambers found that an increased number of iRBCs from CM patients could bind to a primary brain endothelial cell monolayer under flow compared with iRBCs from uncomplicated malaria cases[128], suggesting an expansion of brain-tropic parasites in CM patients. While significant mechanistic insights have been gained from static and flow-based binding assays, 2D monolayer formats lack important microvascular parameters, such as lumen dimensions, branching architecture, and vessel curvature, that influence microfluidic parameters and endothelial transcription and behavior. New in vitro vascular engineering models will pave the way for more physiological studies in malaria pathogenesis research.

2.5. New Avenues in Vascular In Vitro Engineering

Recent advances in tissue engineering have allowed for the development of various modeling strategies to study vascular diseases and have great potential to push the frontier of malaria research. Different vascular models have been generated with varying complexities. While vascular networks can be generated via self-assembly – either as cells in a gel[195,196] or vascularized organoids[197] from stem cells – the lack of control on vascular structure and perfusion has limited their usage in studies that require refined flow control. Recent advances have been focused on the creation of 3D perfusable microvascular models through a variety of manufacturing techniques. These methods offer different levels of cellular, structural, and physiological complexity to investigate the interaction of molecular and cellular processes in different organ environments.

2.5.1. PDMS-Based Microfluidic Channels and Networks

Twenty years ago, soft lithography technology was developed to transfer the silicon-based microfabrication technology into silicone-based materials, such as polydimethylsiloxane (PDMS). This technology has been exploited to fabricate microchannels and transparent networks that can be studied under precise microfluidic flow when connected to a flow pump. PDMS microchannel networks extended the horizon of malaria research by providing tools to study the rheology of *P. falciparum*-iRBCs through geometries that mimicked capillary constrictions or splenic endothelial slits in PDMS models (reviewed in[198]). However, limitations exist in the use of PDMS and similar materials due to the high chemical absorbability and its rigidness, which is far from recapitulating the biomechanical properties of the vessel wall or the lubricating properties of endothelial cells. Additionally, this platform imposes difficulties in studying the effect of the perivascular cell's extracellular matrix on endothelial cell phenotype and heterogeneity.

2.5.2. Hydrogel-Based Microvascular Networks

To better mimic the microvascular environment, soft lithography techniques were later extended into hydrogel platforms to build microfluidic networks in cell-compatible biomimetic extracellular matrices, such as collagen and fibrin. The resultant channels can be seeded with organ-specific endothelial cells in channels with different branching architecture, and perfused with defined flow conditions[79] (Figure 2.2). Conventional soft lithography techniques can generate robust vessels at diameters of 50–500 μm in collagen but they tend to collapse at smaller sizes[89]. An advantage of the hydrogel format is that perivascular cells, like pericytes, can be seeded into the biomatrix and directly

interact with endothelial cells[79]. Other advantages of hydrogel-based vascular engineering platforms are described in Figure 2.2.

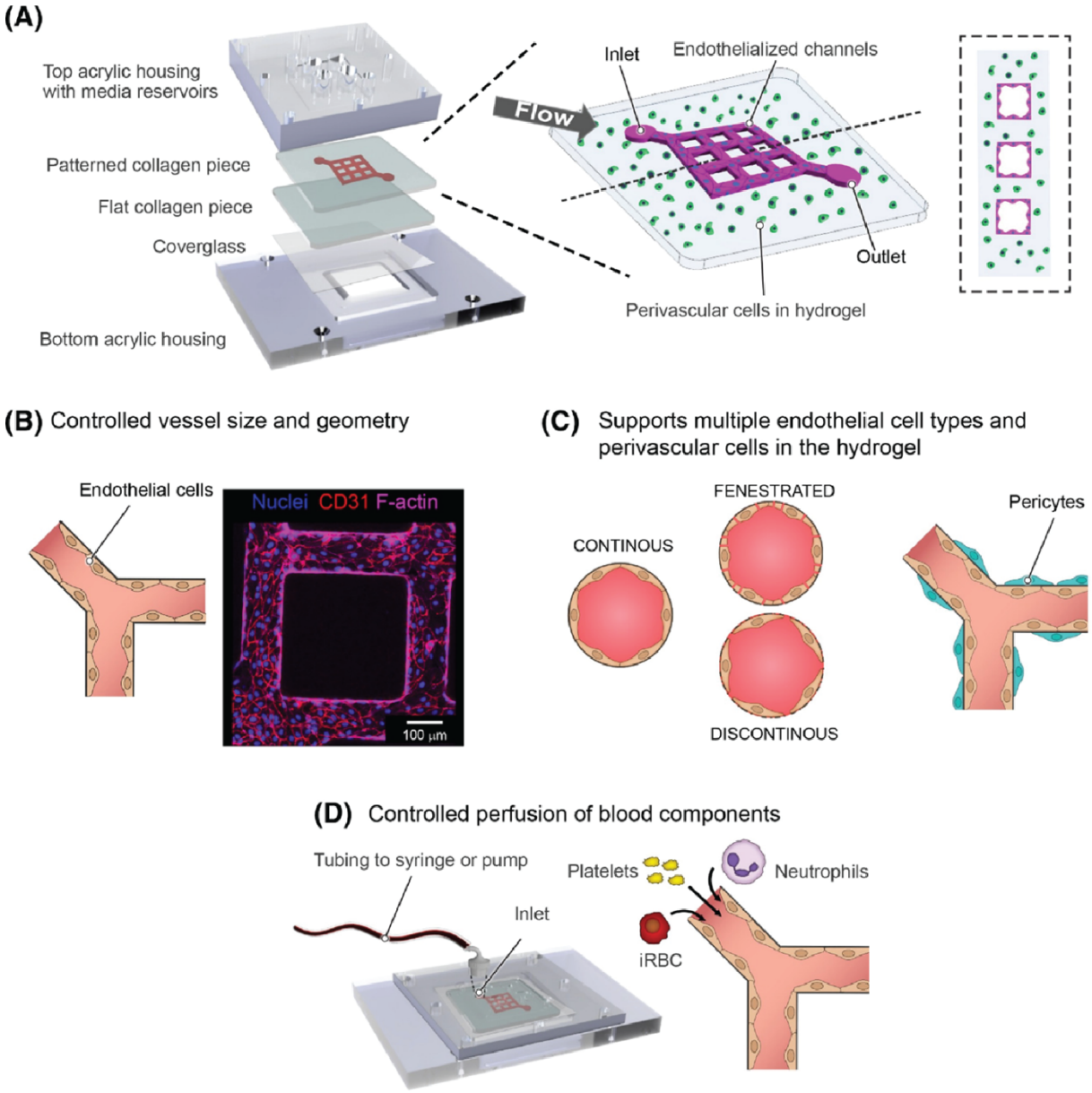

Figure 2.2 Bioengineered in Vitro Vascular Models.

(A) Rendering of device components (left), and schematic representation of 3D microvessels with a 3 × 3 grid microfluidic network (right). Bioengineered 3D microvessels are a versatile model. (B) Engineered microvessels have controllable vessel size, diameter, and network geometry. (C) Engineered 3D microvessels are compatible with multiple endothelial cell types, including continuous, fenestrated, and sinusoidal endothelium, and support the growth of perivascular and parenchyma cells within the hydrogel. (D) The use of a predetermined network provides refined control over microfluidic properties when

connected to a flow pump. Perfusion of different blood components through the device can be independent, sequential, or combined to understand the independent or synergistic contribution of parasite and host components in cerebral malaria (CM). Abbreviation: iRBC, infected red blood cell.

The microvessel format has been used in several recent studies for investigating vessel wall interactions that are relevant for malaria research. For example, a 13 × 13 grid network design, based on human umbilical vein endothelial cells, was used to create a large range of physiological and pathological flow velocities that have been used to study flow-driven interactions of vWF and platelets[89]. This analysis showed that the ability of vWF to assemble into thicker fibers and more complex meshworks was influenced by vessel geometry and microfluidic properties. The same grid-based 3D microvessel format was adapted to study *P. falciparum*-iRBC interactions with primary brain endothelial cells[90]. This study found that iRBC binding to 3D brain microvessels is strongly influenced by physiological differences in flow shear that exists within the brain microcirculation, and that parasite adhesion strength is highly sensitive to changes in EPCR and ICAM-1 expression levels on the endothelial cell surface caused by TNF-α activation. Some PfEMP1-clonal parasite lines presented increased sequestration, while no difference was found in others, depending on their combinatorial binding properties[90]. These findings suggest a highly tuned strategy for parasite sequestration under different conditions experienced during human infection.

Endothelial-only 3D microvessel models have also been used to understand changes in endothelial permeability during malaria infections. For instance, the endothelial-cell-only 3D microvessel 13 × 13 model has been used to study barrier function in response to human CM sera[199]. In a different endothelial-cell-only model, built from a crosslinked agarose–gelatin interpenetrating polymer-network (IPN) hydrogel, iRBCs caused

occlusion of 20 μm microvessels followed by an immediate increase of permeability. Two days after occlusion, the microvessels recovered baseline permeability levels, and endothelial cells were found to have engulfed the malaria pigment, hemozoin[86]. To better mimic brain pathogenic events in CM patients, future models might incorporate hypoxia.

Alternatives approaches to build perfusable tubes and networks in hydrogels include subtractive molding[200] and bioprinting[83,201,202]. Success was demonstrated via subtractive molding to remove a needle from a hydrogel after gelation and form a hollow lumen for endothelial cell seeding and culture. Bioprinting has been demonstrated in either the direct printing of highly viscous biomaterials or sacrificial materials [83,201] that can be removed after the surrounding hydrogel or scaffolds are crosslinked, followed by endothelial cell seeding and culture. This highly automated process has shown success in generating thick, complex 3D channels for endothelial cell seeding and culture to form defined networks. These approaches allow the integration of perivascular and extravascular cells, and controlled perfusion, but are restricted to relatively large-diameter vessels (100 μm or larger) which are larger than the capillary and postcapillary venules where parasite sequestration usually occurs[172,177].

2.5.3. BBB Models

These new bioengineered microvessel models have shown promise in revealing new vascular biology phenomena and have provided molecular insights into molecular, microfluidic, and geometric factors that promote microvascular obstruction in malaria. Future CM models need to better recapitulate the unique cellular environment and barrier properties of the BBB. Many efforts have focused on the development of 3D BBB models with different degrees of success. Two promising models that combine PDMS and

hydrogel-based microfluidic fabrication methods have achieved physiological low permeability rates similar to human BBB[203,204]. Both models incorporate endothelial cells, differentiated from induced pluripotent stem cells (iPSCs) and primary astrocytes and pericytes, that increase the expression and strength of tight junctions and BBB specific transporters. These models have outstanding potential for studying barrier function. However, they present some limitations as either they do not reproduce the dimensions and branching architecture of the brain microvasculature[204]. or do not offer a reproducible flow control which makes difficult the generation of biological replicates[203]. As flow has an important role in tuning endothelial cell transcriptional networks[144] or BBB properties[205], future CM in vitro vascular models need to achieve low BBB permeability rates and consistently reproduce brain branching networks and flow properties.

2.6. Concluding Remarks

P. falciparum sequestration is broadly distributed in diverse microvasculature beds in fatal CM cases[187]. Vascular dysfunction contributes to the complex array of multisystem organ complications that malaria patients can suffer. Along the circulatory system, the endothelial lining of blood vessels presents differences in receptor expression, and organ-specific microvessels present distinctive branching architectures and flow properties that may influence parasite sequestration burdens. Likewise, the unique functions of each microvascular bed, given by distinct perivascular cell composition and endothelial cell phenotype, might influence how blood vessels react to parasite, inflammatory stimuli, and immune cells. To better understand organ-specific disease mechanisms in malaria, and evaluate therapeutic interventions, in vitro models need to mimic disease mechanisms

found in patients and recapitulate functional and structural heterogeneity of organ-microvessel beds.

Altogether, engineered in vitro 3D microvessels offer a versatile opportunity to consistently reproduce and understand the heterogeneous pathology of a complex disease such as malaria. Hydrogel-based methods provide an extracellular matrix that supports the growth of multiple cell types. Some of these methodologies allow control over network branching, microfluidic properties, and internal lumen dimensions with regulated perfusion of different parasite and blood components that, independently or collectively, might cause CM pathogenesis. In the past decade multiple organ-specific vascular models have been developed by using endothelium of primary origin or differentiated from iPSCs, including kidney[75,106], brain[90], or BBB models[203,204]. These models hold great promise to gain a better understanding of the organ-specific disease mechanisms in CM patients. Likewise, although less explored, future models of the skin, liver, or bone marrow microvasculature might reveal new findings in the biology of pre-erythrocytic and transmission stages in malaria.

Chapter 3. BIOPHYSICAL AND BIOMOLECULAR INTERACTIONS OF MALARIA-INFECTED ERYTHROCYTES IN ENGINEERED HUMAN CAPILLARIES

Parts of this chapter have been published in the following manuscript: Arakawa C*, Gunnarsson C*, **Howard C***, Bernabeu M*, et al. “Biophysical and biomolecular interactions of malaria-infected erythrocytes in engineered human capillaries.” Science Advances, 2020[91]. *equal contribution

3.1. INTRODUCTION

Microcirculatory disorders are associated with both infectious and noninfectious diseases, including *Plasmodium falciparum* malaria[121], sickle cell disease[206], and type 2 diabetes[207]. Sequestration of *P. falciparum*–infected red blood cells (IRBCs) in the microcirculation has been recognized as a critical event in severe malaria pathogenesis and associated life-threatening complications, leading to approximately 500,000 deaths per year[208,209]. During the blood stage of infection, *P. falciparum* parasites extensively modify the host erythrocyte cytoskeleton and membrane, resulting in altered red blood cell (RBC) deformability and new adhesive properties. In particular, IRBCs display knob-like surface protrusions that stiffen the erythrocyte membrane[210,211] and present the *P. falciparum* erythrocyte membrane protein 1 (PfEMP1) ligands that mediate cytoadhesion to the vascular endothelium[212,213]. Both knobs and PfEMP1 are thought to contribute to IRBC sequestration, giving rise to enhanced disease severity through small vessel occlusion, tissue ischemia, and eventual organ failure[121,212,214–217]. In addition, sequestered IRBCs may localize host or parasite-derived products that contribute to endothelial dysfunction

and organ damage[161]. Worldwide deaths attributed to malaria remain high, even after the introduction of more effective, faster-acting, antimalaria drugs[218]. Investigating disease mechanisms and new therapeutic approaches to combine with antimalaria drugs has proven challenging as *P. falciparum* is a human tropic pathogen with complications focused at the capillary and postcapillary venule[172,177]. As no proper in vitro human capillary model exists, inferences must instead be drawn from postmortem analysis or studies in non-natural hosts [primate infections[219] or ex vivo rat microcirculatory models[216]], in which host receptors are not the natural binding partners for *P. falciparum* ligands.

Within the microcirculation, RBCs (diameter dAVG = 7.5 μm) deform as they traverse capillaries (dAVG = 3 to 10 μm) that are often narrower than their resting-state diameters. To understand how the altered deformability of *P. falciparum*–IRBCs contributes to microcirculatory obstruction, the mechanics of RBC flow have been modeled in vitro using narrow glass tubes or wedge-shaped, rigid PDMS (polydimethylsiloxane)–based microfluidic devices[220–224]. While these approaches have demonstrated geometric thresholds for mechanical trapping of IRBCs[221,225], they do not account for either the lubricating properties of the endothelial glycocalyx or the adhesive contributions of endothelial cells[226,227]. Conversely, flow-based, endothelial monolayer models have investigated the role of different host receptors in parasite cytoadhesion[128,228,229], yet they are unable to capture the geometric constraints that govern IRBC flow through narrow capillary constrictions or the flow rate transitions encountered as cells traverse different-size microvessels. The altered adhesive and mechanical properties of IRBCs and the alterations in flow dynamics experienced by IRBCs within microvessels likely all

contribute to sequestration in a mutually dependent manner. Without an adequate human capillary model, the contributions of these biophysical and biochemical factors of IRBC sequestration cannot be explored.

We addressed these challenges by developing a three-dimensional (3D) arteriole-capillary-venule (ACV) microvessel unit, in which endothelial cells are grown in a native extracellular matrix. After optimizing the design parameters of 3D capillary fabrication and endothelialization, we used the ACV unit to identify the distinct spatiotemporal dynamics of RBC capillary transit and dissect the individual contributions of cytoadhesion and mechanical stiffening to IRBC sequestration. Our study sheds light on the mechanisms underlying IRBC sequestration during severe malaria infection and provides a unique platform to study the cellular, microfluidic, and geometric factors that give rise to microvascular obstruction in hematologic diseases.

3.2. Results

3.2.1. Generation of perfusable capillary microchannels via collagen photoablation

To create an efficient capillary model, we first fabricated an acellular 3D ACV microvessel unit via a two-step process. First, large arteriole or venule-sized microchannels (lumen diameter d = 200 μm, spaced 450 μm apart) were lithographically fabricated in collagen hydrogels (7.5 mg/ml, ~200 to 500 Pa), as previously described[230]. Then, an array of capillary-sized microchannels or features of arbitrary user-defined geometries[231] were generated between the two main channels using multiphoton microscopy–guided femtosecond laser photoablation. Ablated regions were confirmed using second harmonic imaging of collagen fibers. Arrays of channels ranging from 5 to 20 μm in diameter were rapidly produced (~75 channels/hour) with high density and robust

perfusability by 0.22-μm fluorescent beads. The density generated (~11,600 channels/mm2 for 5-μm arrays) can reach a similar or higher level than that observed in the human heart [1100 capillaries/mm2 in vivo[232]].

Endothelialization of this ACV model posed substantial challenges as conventional methods of cell seeding after microvessel fabrication[79] led to sparse endothelial coverage within the microchannel arrays and nonperfusable vessels even after 7 days of culture. Successful endothelialization was achieved by leveraging the precise yet destructive nature of photoablation to simultaneously incur local endothelial cell injury while generating capillary-sized void spaces between two preformed main microvessels (Figure 3.1A). This methodology encouraged endothelial cell migration and ingrowth into the ablated channels (Figure 3.1B). Stable endothelial coverage was observed in the capillary-sized channels as early as 18 hours following photoablation (Figure 3.1C), and complete endothelialization of 20-μm channels was observed after 4 days of culture under gravity-driven flow across the microvessels (Figure 3.1B).

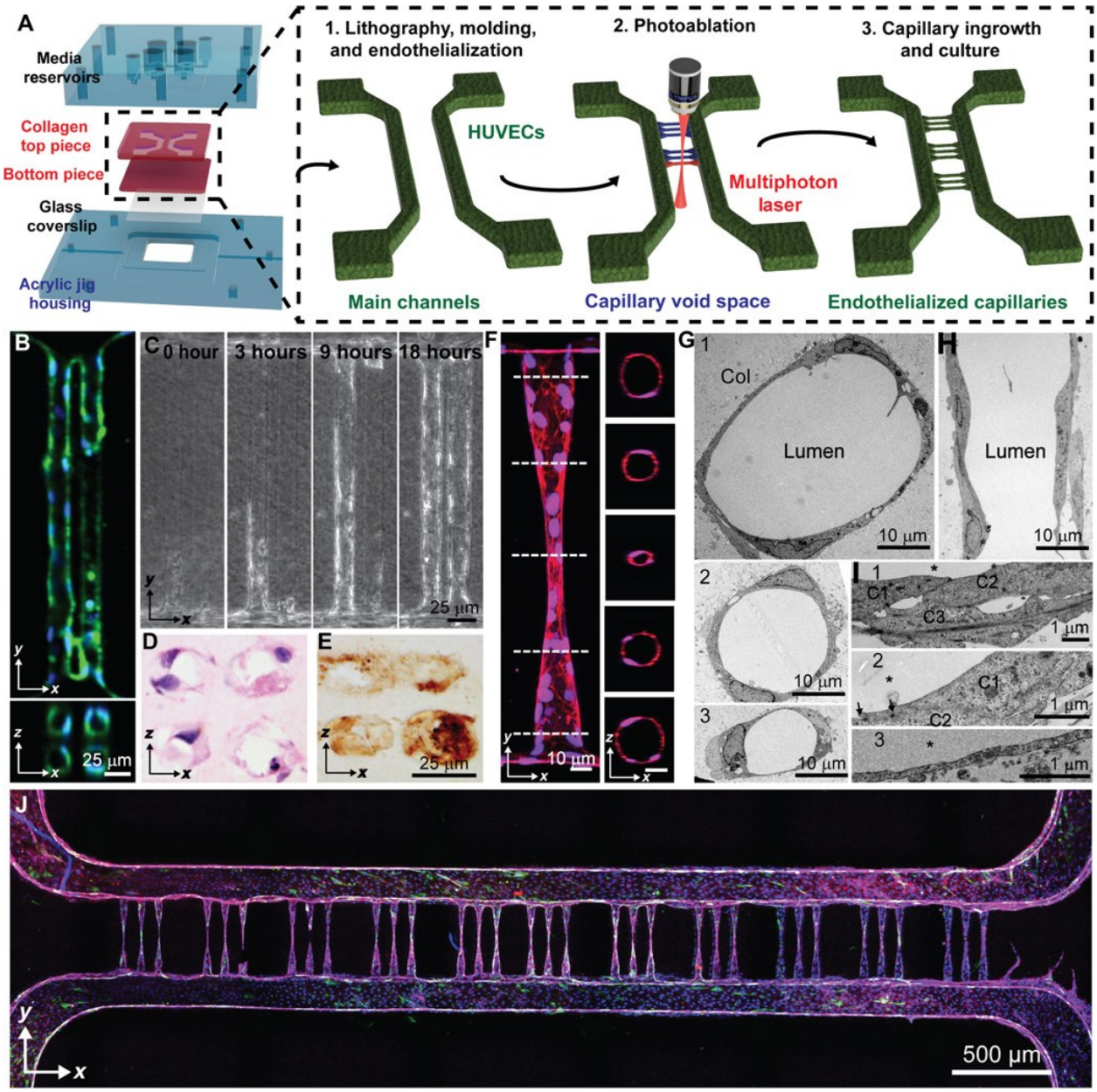

Figure 3.1 Photoablation-guided capillary growth in lithography-based microvessel devices.

(A) Diagram of device assembly and capillary fabrication. Main channels were generated by soft lithography in acrylic jigs followed by capillary generation by photoablation and endothelial ingrowth. (B) Array (2 × 2) of 20-μm-diameter vessels demonstrates stable vessel lumens. Green: F-actin; blue: nuclei. (C) Endothelial ingrowth over 18 hours demonstrates complete vessel formation. (D and E) Cryosectioned capillaries were stained with (D) hematoxylin and eosin as well as (E) type IV collagen, demonstrating lumen formation by single endothelial cells and robust basement membrane deposition. (F) Constriction vessel design allows for the generation of sub–10-μm-diameter capillaries shown in both projected and cross-sectional views. Red: VE-cadherin; blue: nuclei. (G to I) Ultrastructural analysis of capillary vessel regions by transmission electron microscopy (TEM) shows vessels at varying diameters (from 40 to 10 μm) in cross-sectional (G and I) and longitudinal (H) views and varying wall thicknesses and junctions at cell-cell contact in zoomed views (I). Cross-sectional views of vessel regions near the connection. Col: collagen substrate; *: lumen;

C: cells. (J) Stitched confocal image demonstrates complete vessel network consisting of 33 capillaries. Green: von Willebrand factor; blue: nuclei; red: VE-cadherin; purple: F-actin.

3.2.2. Photoablation-guided cellular ingrowth establishes robust capillaries in an ACV unit

In vivo, capillary lengths range from 150 to 500 μm[233]. To determine the vessel patency at high vessel density, 2 × 2 arrays of straight channels, consisting of either 10- or 20-μm lumen diameters spaced 5, 10, or 20 μm apart, were photoablated between two preformed main microvessels of 200-μm diameter. Microchannels that were initially separated by only 5 or 10 μm demonstrated partial or complete fusion after endothelial cell ingrowth from the two main microvessels, leading to a larger vessel diameter. By comparison, microchannels of 20-μm diameter separated by a 20-μm distance maintained high vessel diameter fidelity (Figure 3.1B), Whereas 10-μm diameter channels exhibited incomplete endothelialization and patchy endothelial coverage, vascularization was more efficient in 20-μm channels. The average length of continuous endothelium in 10-μm diameter channels was approximately 126.7 ± 60.2 μm, corresponding to an aspect ratio [AR = length (l): lumen diameter (d) of 12.7 ± 6.0]. In contrast, 20-μm-diameter vessels demonstrated near-complete endothelialization (365 ± 105.4 μm) (AR = 18.3 ± 5.3). Moreover, 20-μm-diameter vessels exhibited clear lumens upon histological staining and deposited abundant type IV collagen, suggesting the generation of a robust basement membrane (Figure 3.1, D and E). Together, these data suggest geometric constraints for small vessel size formation (a minimum distance of 20 μm between two parallel small channels and maximum AR of approximately 12 to 18) to maintain vessel patency, which has consistent range with human in vivo measurements for the length-to-diameter ratio[232].

In vivo, RBCs experience changes in velocity as they traverse different-sized microvessels within the ACV unit[234]. To build a robust capillary model at smaller diameters (5 to 10 μm) that more accurately mimics the in vivo vascular tree, we designed a constriction-shaped ACV geometry with a gradual change of diameter and a reduced AR for the capillary regions. This design consisted of five distinct regions that combine to form a symmetric hourglass shape: a precapillary arteriole and a postcapillary venule mimicking vessels with constant width (w = 40 μm, l = 80 μm, thereby AR = 2), which were connected to a capillary-sized region (w = 5 μm, l = 80 μm, AR = 16) by two flanking narrowing/expanding transition regions (w = 40 to 5 μm, l = 105 μm). This vessel design decreased the length of the capillary-sized region and increased the width or diameter of the sections that connected with the two main larger-sized microvessels, therefore promoting endothelial cell ingrowth and capillary patency (Figure 3.1, F to J).

Two cell seeding approaches were tested for endothelialization efficiency and perfusability: (i) direct cell seeding of fully acellular channels followed by 7 days of culture and (ii) photoablation-guided capillary ingrowth for 4 days from two large preformed main vessels after 3 days of culture (7 days total). The hourglass-shaped ACV unit design supported robust endothelial cell ingrowth throughout the capillary-sized channels using both seeding approaches. While successful endothelialization could be achieved using either of the seeding methods (65 ± 1% versus 77 ± 7%, mean ± SEM), the percentage of perfusable capillaries was significantly higher when endothelial cells grew into the photoablated channels from preformed microvessels (57 ± 12% versus 17 ± 7%, mean ± SEM, **P < 0.002). Implementation of photoablation-guided capillary ingrowth resulted in robust, consistent, and perfusable capillary-sized microvessels of 5- to 10-μm diameter,

measured via confocal microscopy (Figure 3.1, F to J). Similar to the two main vessels, the endothelium within the ACV regions was positive for vascular endothelial (VE)–cadherin (a marker of intercellular junctions) and von Willebrand factor (a marker of Weibel-Palade bodies) (Figure 3.1, F to J). We further measured the diameter at the narrowest region of the capillary constriction zones, which ranged from 7.5 to 13.6 μm (10.9 ± 1.8 μm, mean ± SD, n = 25 capillaries) in confocal microscopy and 5.6 to 13.2 μm (8.6 ± 2.1 μm, mean ± SD, n = 15 capillaries) in two-photon microscopy.

Electron microscopic analysis confirmed the gradual changes of vessel diameter along the longitudinal direction (Figure 3.1, G to I). Ultrastructure of vessel regions with cross-sectional diameters larger than 20 μm was often formed from two or more endothelial cells, connected with focal contacts and junctions between surrounding cells (Figure 3.1, G1 and G2). By comparison, at regions of 10 μm or smaller in diameter, lumens appeared to be enclosed by a single endothelial cell, which formed extensive focal contacts and complex junctions with overlapping cell peripherals from one or two neighboring cells (Figure 3.1, G3). The lumenal wall displayed heterogeneous thickness, ranging from approximately 100 nm to several micrometers at the regions of cell bodies or overlapping cell regions. This also led to varying vessel diameters in both longitudinal and circumferential directions across the ACV unit, although vessels remained intact and continuous across almost all planes examined (Figure 3.1, G and H). Together, our data suggest an efficient approach to fabricate a continuous, endothelialized, perfusable ACV unit with high fidelity and patency.

3.2.3. Normal and infected RBCs display different mechanics of motion and deformation across the capillary region

When normal RBCs were perfused through the completely endothelialized ACV devices at full hematocrit, the presence of endothelium appeared to facilitate the smooth perfusion of RBCs through the capillary constriction region. By comparison, in acellular collagen microchannels with the same hourglass geometry, RBCs accumulated upstream before entering the narrowest region, leading to local increases of hematocrit, as well as intermittent jetting of RBCs into the capillary constriction zones and much lower hematocrit further downstream. This comparison of acellular and endothelialized microvessels reinforces the importance of the endothelium in understanding the interaction of RBCs and capillaries.

We next exploited this endothelialized capillary model to study the biomechanical and functional differences between normal and infected RBCs under flow. To allow visualization of individual cells as they traverse the ACV units, RBCs were perfused at a low hematocrit. When normal RBCs were perfused through ACVs at low hematocrit and velocities similar to in vivo capillary flow rates (≈250 to 1500 μm/s)[233–235], they displayed in vivo–like stretching in the capillary region and tumbling behavior in the pre- and postcapillary regions (Figure 3.2, A and B). Normal RBCs readily traversed the capillary regions down to 5 μm in diameter and assumed a variety of deformations, including parachute-like, slipper-like, and discocyte shapes (Figure 3.2C), in agreement with previous in vivo observations[220], computational simulations[236,237], and microfluidic studies in narrow glass tubes[237]. Using edge detection–based image analysis, we tracked the position, velocity, shape, and orientation of individual RBCs throughout the capillaries (Figure 3.2D). Normal RBCs showed two major modes of motion in the capillary regions:

elongation, characterized by stretching along the major axis by up to twofold (Figure 3.2D (i)), and tumbling, characterized by oscillations in major axis orientation (Figure 3.2D (ii)). Compared with normal RBCs, *P. falciparum*–IRBCs present increased rigidity due to knob-like modifications to the erythrocyte cytoskeleton[210,211] and modest changes in RBC volume and its biconcave shape due to the growing intracellular parasite[238], which might change the IRBC mechanics through capillary-sized vessels. To understand how the intracellular parasite body contributes to the biomechanics of IRBC traversal through the microcirculation, independently of knob rigidification and cytoadhesion, we perfused a clonally derived parasite variant called 2G2, which has been selected for lack of knobs by gelatin[239]. Although not statistically different compared with normal RBCs, 2G2-IRBCs presented minimal elongation and mostly tumbled through the capillary region despite being perfused at similar velocities to normal RBCs (Figure 3.2E). Because rolling and tumbling along the microvascular endothelium enhance cytoadhesion and increase the probability of ligand-receptor interaction at high shear stress[240], we expect that these differences in tumbling motion may enhance the ability of malaria-infected RBCs to both be mechanically trapped and cytoadhere in capillaries.

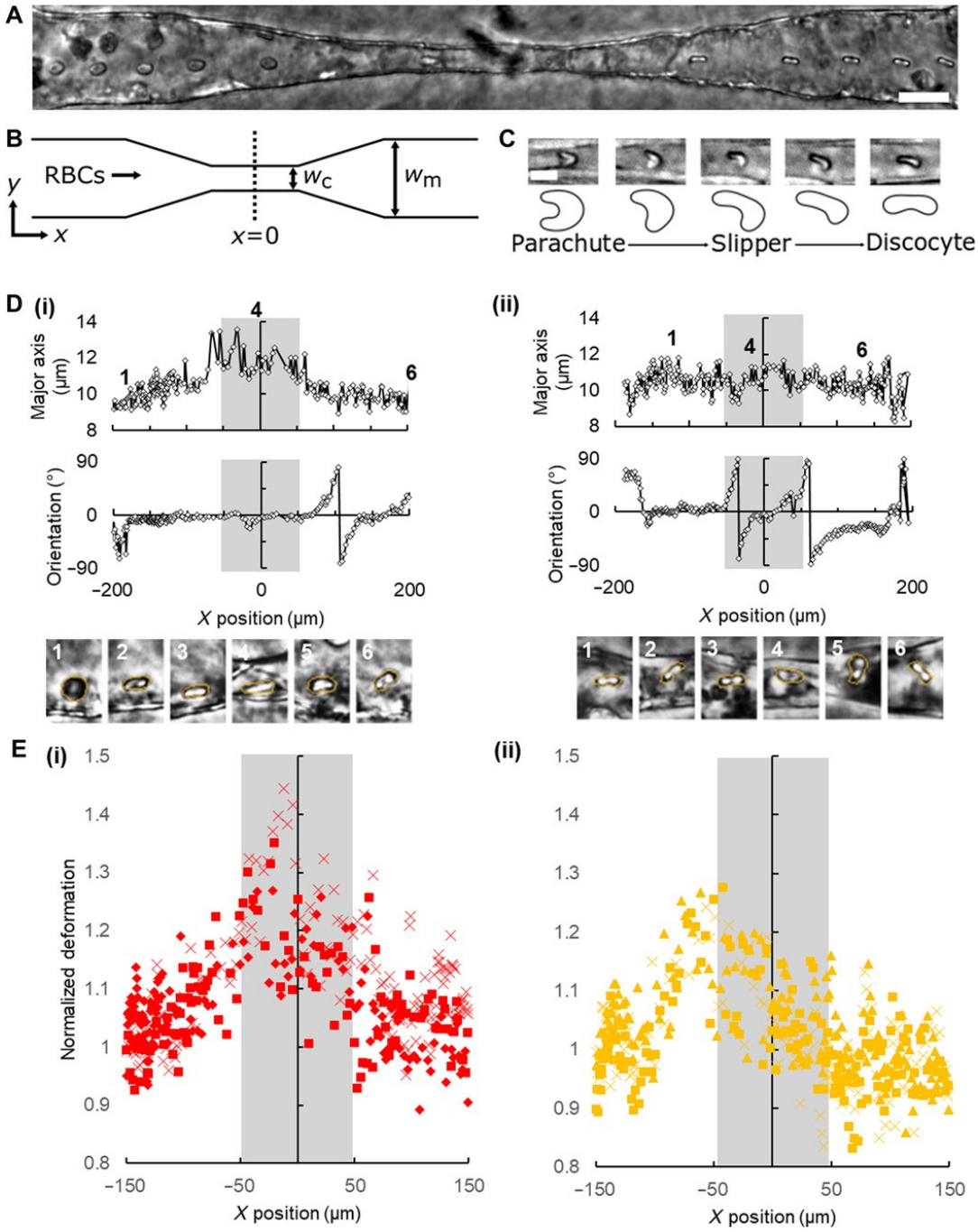

Figure 3.2 Motion and deformation of RBCs while traversing capillary constriction zones.

(A) Superimposed time lapse image series of RBC motion through an endothelialized vessel. Time lapse interval: 0.1 s. Scale bar, 25 μm. (B) Schematic showing RBC perfusion through constriction-shaped vessel. wc = 10 μm; wm = 40 μm. (C) Representative examples of parachute-, slipper-, and discocyte-like RBC deformations in capillary constrictions. Scale bar, 10 μm. (D) Representative traces of RBC major axis length and orientation for (i) stretching and (ii) tumbling RBCs, where x = 0, y = 0 is the center of the capillary; gray boxes: capillary extents. (E) Normalized extent of deformation, defined as the ratio of major axis length at a given position to the average major axis length in the precapillary region for (i) normal RBCs

and (ii) knobless malaria-IRBCs (n = 3; each biological replicate is represented by one symbol, ■, ♦, ×, or ▲).

3.2.4. P. falciparum–IRBCs occlude the capillary region at physiological hematocrit conditions

In the microcirculation, hydrodynamic forces encourage separation and margination of IRBCs from their uninfected RBC counterparts toward the vessel wall, enhancing cytoadhesive interactions with endothelial cells[241,242]. To investigate whether IRBCs sequester at physiological hematocrit concentrations (Figure 3.3A), fluorescently labeled IRBCs (0.4 to 4% parasitemia) or normal RBCs were perfused at 40% hematocrit using gravity-driven flow, leading to an average flow rate at approximately 0.002 µl/min in each capillary during the first 30 min of perfusion. The cell accumulation was assessed at 1, 4, 7, and 20 min by fluorescence imaging and was compared with flow modeling to relate predicted flow dynamic changes across the microvessels to retention and occlusion events (Figure 3.3, B and C). Normal RBCs traversed the entire constriction zone with minimal sequestration in any vessel region (Figure 3.3, C to I). Both labeled and unlabeled normal RBCs deformed as necessary to pass through the narrowest regions, suggesting that the membrane-labeling procedure did not significantly increase sequestration potential. By comparison, IT4VAR19, a knob-positive (K+) and cytoadherent parasite variant (PfEMP1+)[192] displayed steady accumulation (Figure 3.3C (ii)). Kinetic video analysis demonstrated sequestration throughout the capillary constriction zone with highest accumulation in the first half. Complete occlusion of the capillary region could be observed within minutes after initiation of flow, followed by accumulation of fluorescent IRBCs upstream of the blockage. At end point, K+PfEMP1+ IRBCs demonstrated high fluorescent signals centered in the capillary region and extending into the post- and precapillary regions. Ultrastructural analysis showed that the capillary regions contained

a mixture of both infected and normal RBCs, suggesting that occluded vessels may trap normal RBCs. By transmission electron microscopy (TEM), IRBCs were found in close apposition to lumenal walls, even following perfusion washing. Moreover, some IRBCs were trapped or encircled by the endothelial cell membranes or appeared to have been fully engulfed by an endothelial cell, as observed previously in monolayer assays with immortalized endothelial cells[243].

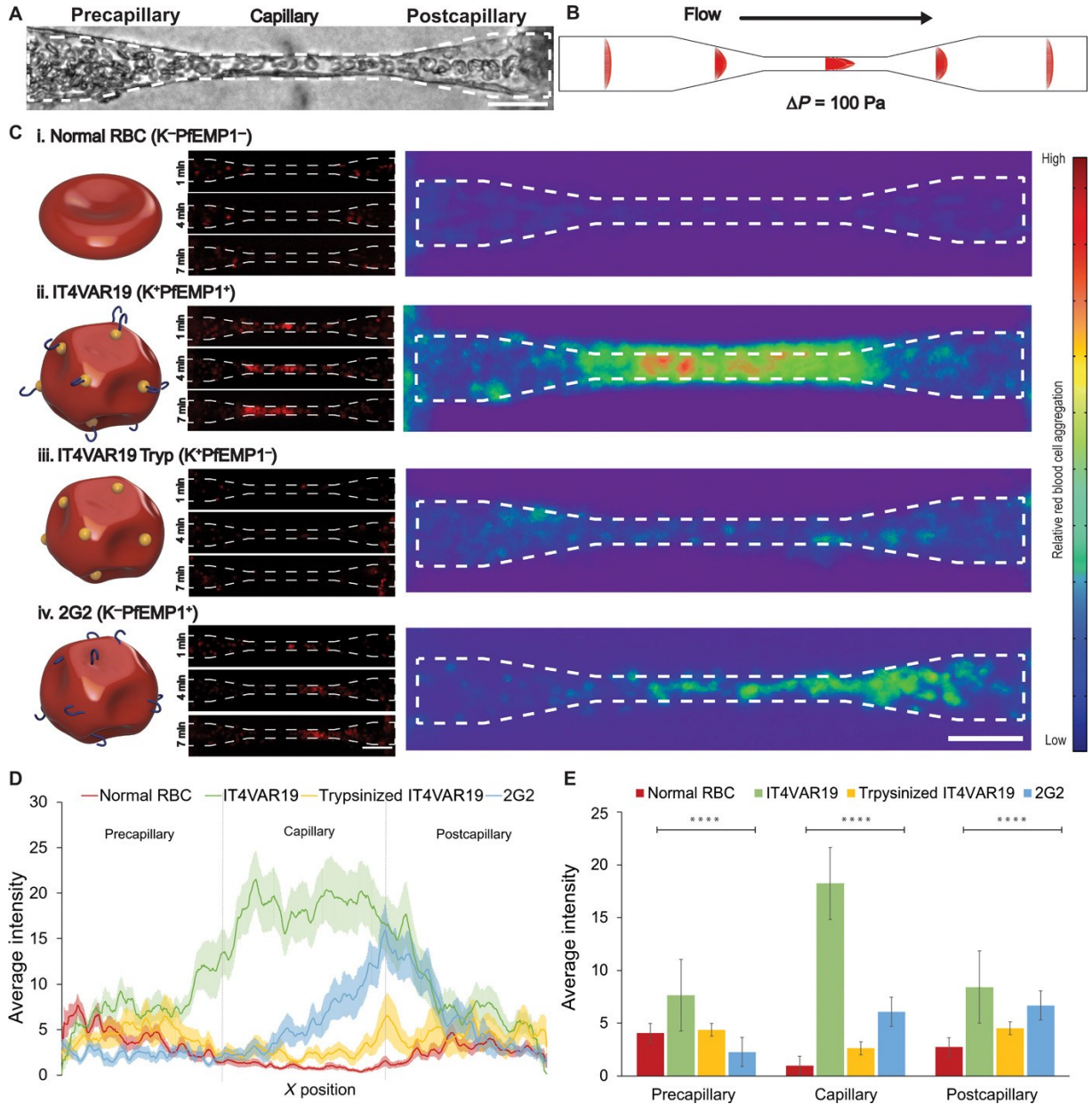

Figure 3.3 Population dynamics analysis of RBC flow and accumulation within constriction capillaries.

(A) Bright-field image of RBCs flowing through a constriction vessel. Dotted lines demonstrate capillary outline trace. (B) Flow velocity model of a single capillary based on fabrication dimensions. (C) Left: Schematic illustrations of the different types of perfused RBCs and IRBCs. Middle: Representative image of binding kinetics within the capillary constriction zones. IRBCs are shown in red. Right: Spatial distribution of accumulation after 20 min of perfusion represented by a combined heat map of average fluorescence from multiple experiments. Normal RBC (n = 24), IT4VAR19 (n = 26), trypsinized IT4VAR19 (n = 19), and 2G2 (n = 19). (D and E) Quantification of average intensity as a measure of x position (D) and comparison among precapillary, capillary, and postcapillary regions (E). n = 24, 26, 17, and 19 ACV units quantified from N = 4 independent experiments for each condition of perfusion: normal RBC, IT4VAR19, trypsinized IT4VAR19, and 2G2, respectively. Analysis of variance (ANOVA) F = 11.61, P < 0.00001 for precapillary

region, ANOVA F = 47.83, P < 0.00001 for capillary region, and ANOVA F = 6.41, P < 0.001 for postcapillary region.

3.2.5. Parasite-induced knobs and cytoadhesion ligands make independent and distinct contributions to P. falciparum–IRBC accumulation in capillary regions

To elucidate the relative contributions of altered adhesive and mechanical properties in IRBC microvessel obstruction, we trypsinized IT4VAR19 IRBCs to remove the surface presentation of PfEMP1s while leaving the knobs intact (K+PfEMP1−). Previous work by atomic force microscopy has established that *P. falciparum* knobs are unaffected by trypsin treatment[244]. Following trypsinization, there was a marked loss of antibody recognition with two polyclonal antibody reagents against the first and fourth DBL domains in the IT4VAR19 PfEMP1 variant. Perfusion of K+PfEMP1− IRBCs demonstrated minimal sequestration throughout the constriction zone, with binding levels similar to normal RBCs in all vessel regions (Figure 3.3, C to E). These findings suggest that while mechanical stiffening may contribute to IRBC margination toward the vessel wall in the postcapillary regions[242], surface-active PfEMP1 is necessary to cause IRBC sequestration. Furthermore, despite the geometric confinement in capillaries, mechanical stiffening on its own is insufficient to induce the same trapping in the 5- to 10-μm capillary-sized constrictions observed with the K+PfEMP1+ IRBCs.

We next perfused 2G2 (K−) to better understand the contribution of knobs to cytoadhesion[239], as they are thought to enhance PfEMP1-mediated adhesion[213,216,245] and increase the mechanical stiffening of IRBCs[246]. Notably, both IT4VAR19 and 2G2 express endothelial protein C receptor (EPCR)–binding var transcripts[152], but 2G2 exhibits much weaker cytoadhesive capabilities under flow conditions[90]. Although the weakly adherent 2G2 parasites (K−) exhibited higher sequestration rates than the

trypsinized IT4VAR19 (K+PfEMP1−), cell accumulation was concentrated to the second half of the capillary constriction zone, where cells would experience deacceleration and less flow shear as they transition into the larger-diameter region (Figure 3.3, C and D). Together, this analysis identifies distinct and independent contributions of the microcirculatory hemodynamics and parasite-induced modifications to RBCs in microvascular obstruction.

3.3. DISCUSSION

Cytoadhesion of *P. falciparum*–IRBCs is a major virulence determinant, but knowledge gaps exist in how parasites cause microvascular obstruction, and the ability to study important human microcirculatory disorders in vitro has been limited to nondeformable glass or microfluidic chamber platforms. Here, we describe an efficient fabrication approach for engineering robust and patent capillary arrays in an ACV unit. Our studies exploited this model to investigate normal and malaria-infected RBCs under perfusion and to identify sequential events of biomolecular and biophysical interactions between RBCs and capillary walls that led to parasite sequestration and microvascular occlusion.

Whereas normal RBCs readily traversed the narrow capillary constriction zones, *P. falciparum*–IRBCs rapidly accumulated in these regions. Our study identified distinct contributions of parasite-induced knobs and cytoadhesion ligands in cell accumulation by perfusing IRBCs with different knob structures and trypsinized IRBCs to preserve the knob structure while eliminating the cytoadhesion effects[244]. Although trypsinized IRBCs with cleaved parasite cytoadhesion ligands exhibited limited accumulation in the capillary constriction regions, parasites lacking knobs accumulated at the capillary-venule transition where flow rates were deaccelerating. The efficient traversal of trypsinized

IRBCs through narrow constrictions is consistent with previous microfluidic studies, which demonstrate mechanical trapping of IRBCs only in nondeformable channels below 4 μm in diameter[221]. Knob membrane stiffening more likely contributes to splenic elimination, where interendothelial slits are as narrow as 3 μm[247,248]. The knob-like protrusions anchor both the PfEMP1 cytoplasmic tail and erythrocyte cytoskeleton components, and previous work has established that they contribute to both parasite cytoadhesion strength[213] and the altered mechanical properties of *P. falciparum*–IRBCs[246] and thereby provide mechanical stability to the interactions between PfEMP1 and endothelial cells. In addition, by positioning the PfEMP1 cytoadhesion ligands above the cell body[249], knobs may also facilitate adhesion. With the distinct spatiotemporal binding of knobless parasites, our findings suggest that PfEMP1 physiological display in knobs facilitates IRBC capture from circulation, particularly in regions of higher flow shear in the capillary constriction area. This is consistent with previous work in ex vivo rat microcirculatory models and primate studies[216,245]. Moreover, our findings reinforce the importance of cell deceleration and lower shear stress as cells exit from the capillaries, in mediating IRBC capture from flow. Postmortem autopsy studies have revealed higher IRBC accumulation rates at the postcapillary region (~3-fold increase as compared with precapillary regions)[177]. Thus, our capillary model provides the means to dissect the interdependent interactions of microcirculatory hemodynamics and parasite modifications to malaria obstruction mechanisms.

The differences in pre- and postcapillary sequestration have been thought to arise from arterial-venous differences in flow rates or host receptor expression[250]; nonetheless, this question has been difficult to study. In an ex vivo rat mesoappendix model, IRBC

sequestration initiated in venules and sometimes extended upward by retrograde aggregation into the capillaries and arterioles[216]. Although the rat mesoappendix model has been valuable to explore parameters influencing IRBC sequestration, recent work has also shown that severe malaria is linked to EPCR[152,156,251], which is highly divergent between humans and rats. Notably, both parasite lines used in this study (IT4VAR19 and 2G2) express EPCR-binding PfEMP1; thus, our human capillary constriction model has advantages in investigating the cytoadherence of severe malaria isolates in an in vitro human model.

A limitation of this model is the use of human umbilical cord endothelial cells (HUVECs), a cell type from large-vessel origin. However, HUVECs are commonly used to develop new 3D vascular platforms, and future studies can build on our design principles to incorporate different endothelial cells to develop organ-specific ACV units. In addition, the study of single-cell dynamics is challenging because of the lack of precise flow control in individual capillaries, owing to the parallel nature of many capillaries between the two main vessels in our system and the varying diameters in each capillary, similar to vessels found in vivo. Nevertheless, our ACV unit mimics physiological flow transitions within the microcirculation and could distinguish spatial and temporal binding differences between normal RBCs and IRBCs, as well as between wild-type parasites and parasites lacking PfEMP1 or the knob-like protrusions. Notably, parasite knob densities differ widely between fresh ex vivo parasites[252] and may also be modified in severe malaria infections[253], but it is unknown whether these variations modify IRBC cytoadhesion efficiency or influence disease severity. Our ACV model provides a fundamentally new approach to investigate microvascular obstruction in an in vitro human model. The

success sheds light for future therapeutic development in treating blood-stage malaria and provides a potential platform for the studies of other microvascular disorders, such as sickle cell anemia, or in the context of transfusion medicine of blood products.

3.4. MATERIALS AND METHODS

3.4.1. Multiphoton ablation for the generation of acellular ACV unit

First, two parallel microchannels were fabricated via lithography and injection molding–based techniques in collagen gel, as described previously[79], to mimic arteriole- and venule-sized vessels. Next, multiphoton photoablation was performed in collagen gel between these two parallel microchannels using a Mai Tai DeepSee Ti:S laser (maximum power, 2.57 W) coupled with an Olympus FV1000MPE BX61 microscope fitted with a water immersion objective lens (25×, numerical aperture = 1.05). Microchannels and surrounding collagen regions were first identified by imaging of second-harmonic generation signals produced by collagen microfibers at excitation wavelength λex = 860 nm and detection wavelength λdetector = 420 to 460 nm. Individual capillary-sized channels were designed within the collagen matrix by designating 3D regions of interest using the Olympus Fluoview software and then ablated by laser rastering (λ = 800 nm, I = 100%, pixel dwell time = 2 μs, 10 to 15 line repeat scans). Laser scanning in the X, Y, and Z dimensions were performed at ~1-μm step sizes. After the ablation, 0.22-μm-diameter fluorescent microbeads were perfused from one side of the main channels across the newly created capillary-sized channels to the other side at a pressure drop of 1 cmH2O for 10 min, followed by imaging for evaluation of perfusability.

3.4.2. Endothelializing ACV unit

Two different procedures were investigated to form the endothelialized ACV units: (i) direct cell seeding of acellular channels and (ii) endothelial cell ingrowth after photoablation. In the first approach, the acellular ACV unit is first fabricated by photoablation, followed by seeding cells into the fully acellular device through the inlets of the two main parallel channels with 10-µl perfusions of HUVECs (Lonza, passages 3 to 7, with EBM basal medium supplemented with EGM endothelial cell growth medium) at a density of 8 × 106 cells/ml. Once the cells were attached, the devices were cultured under gravity-driven flow across the capillaries between the two main channels for 7 days. To create a gravity-driven flow, 200 and 180 µl of culture media was placed in the two main channel inlets to set the initial pressure drop at approximately 1 cmH2O, leading to a peak velocity of approximately 1 mm/s across the ACV unit between the two main channels. The pressure drop was reset every 12 hours to maintain flow in the capillary regions.

In the second approach, the two main microchannels were first seeded with 10-µl perfusions of HUVECs at a density of 8 × 106 cells/ml and cultured for 3 days to form robust endothelialized lumens. Multiphoton photoablation was then performed to create microchannel void spaces that tapered down to 5 µm in diameter within the collagen scaffold between the lumenal wall of the two main vessels and ablate endothelial cells at the two end connections. Cellular and collagen ablation was confirmed by imaging identical areas after ablation using transmitted light and by second-harmonic generation imaging. The ablated vessels were then cultured for an additional 4 days to allow for

endothelial cell ingrowth. The culture was maintained at the same pressure drop as the first approach and replenished twice a day with fresh culture media.

3.4.3. Parasite culture

P. falciparum parasite lines were cultured using anonymized human O+ type RBCs (Valley Biomedical) in RPMI 1640 (Gibco) supplemented with 10% human type A+ serum in a gas mixture of 90% N2, 5% CO2, and 5% O2. The knobless parasite line 2G2 was previously derived by lack of gelatin floatation followed by limited dilution cloning[239], while the IT4VAR19 line was generated after repeatedly panning on transformed human brain microvascular endothelial cells followed by limited clonal dilution[188,254]. Mature-stage IRBCs were enriched to 60 to 90% parasitemia by magnetic separation (MACS Cell Separator, LD Columns, Miltenyi Biotec) before perfusion for single-cell and population dynamics experiments. Both parasite lines predominantly express a single var gene and were derived from the IT4/FCR3 parasite genotype.

3.4.4. Monitoring RBC perfusion through capillaries at the single-cell scale

Magnetic enriched mature-stage *P. falciparum*–IRBCs or packed RBCs were resuspended in 10% fetal bovine serum (FBS)–containing EGM at 5 × 106 cells/ml, allowing the visualization of individual cells as they traverse the ACV devices. The dilute cell suspension was placed in the inlet and outlet of one microchannel at a maximum initial pressure drop of approximately 1 cmH2O, creating a hydraulic gradient between the two microchannels and establishing gravity-driven flow across the capillaries. The peak velocity of the RBCs across the center capillary zone was approximately 1 mm/s. In single-cell dynamics studies, the pressure drop and resulting velocity rate were maintained and slightly adjusted over the course of the assay by removing or adding a

small volume (~5 µl) of cell suspension from the inlet to maintain the RBC velocity in this range and allow for video capture of single-cell dynamics. The motion of individual RBCs within one of the capillary constriction channels was visualized with a Nikon TiE inverted widefield microscope, and videos were acquired at 20× and 250 to 500 frames/s using an Orca-Flash4.0V2 Digital CMOS camera (Hamamatsu). After acquisition, videos were analyzed using custom MATLAB scripts. For experiments with 2G2, videos were previously inspected, and only IRBCs with hemozoin were used in the downstream analysis. Briefly, individual frames containing RBCs were smoothed using a Wiener filter, inverted, then background subtracted using a mean filter. RBCs were detected by applying a Canny edge detection operator. Small gaps in RBC outlines were closed automatically using an edge-linking algorithm or manually. Individual RBC outlines were linked into trajectories based on displacement between outlines in different frames. Out-of-focus and overlapping RBCs were excluded from the analysis. Biological replicates were taken in at least two different days.

3.4.5. Monitoring RBC perfusion at physiological hematocrit

Magnetic enriched mature-stage *P. falciparum*–IRBCs or packed RBCs were fluorescently labeled according to the PKH26 Red Fluorescent Cell Linker Kit (Sigma-Aldrich). To simulate blood with physiological parasitemia, labeled cells (normal RBCs or IRBCs) were added to unlabeled normal RBCs at a final parasitemia of 0.4 to 4% (iRBC/total RBC) and then diluted to 40% hematocrit in EGM (containing 5% FBS). RBCs were encouraged to flow across the device driven by a pressure drop of approximately 1 cmH2O for 20 min, leading to a peak velocity of approximately 1 mm/s, mimicking measured physiological velocities within the capillaries[233]. The perfusion of RBCs was

monitored and imaged at different fields of view (three capillary channels in each field of view) and continuous time frames. At the beginning of the perfusion, devices were quickly scanned to identify perfusable channels. Videos were taken for 10 s for each perfusable channel in the same order at each time point to determine the location and extent of binding after 1, 4, 7, and 20 min of perfusion. Each condition was repeated in independent days.

3.4.6. Population dynamics analysis

Quantification of population dynamics was performed on fluorescent images taken after 20 min of perfusion. Images were normalized between average background values and peak fluorescent intensity values, and a two-pixel radius median filter was used to remove speckle noise using MATLAB. Masks were manually drawn to outline individual capillary constriction channels using ImageJ. Average fluorescent intensity was calculated at each x position as the sum of intensity values across the y dimension divided by the diameter of the vessel at this position. The central point of each capillary region was determined, and the average intensity maps were lined up across all images at this central point.

3.4.7. Trypsin treatment and flow cytometric analysis

IT4VAR19 trophozoite-stage enriched IRBCs were treated with a trypsin (66.67 μg/ml; Sigma-Aldrich) solution in 1× phosphate-buffered saline for 30 min at 37°C, followed by an inhibition with an equal volume of FBS before perfusion of capillary devices. To determine PfEMP1 surface expression after trypsinization, an IT4VAR19 culture was incubated for 30 min at 37°C with a trypsin solution (10 μg/ml). Surface PfEMP1 was recognized with rat polyclonal antibodies against IT4VAR19 DBLα2 and DBLγ6 (1:10) for 30 min at 4°C, followed by an incubation with goat anti-rat immunoglobulin G–Alexa Fluor

488 (1:400, Molecular Probes) for 30 min. Infected erythrocytes (parasite nuclei) were detected with ethidium bromide (2 μg/ml; Invitrogen). Stained cells were washed in phosphate-buffered saline and analyzed on an LSRII fluorescence-activated cell sorter machine (BD Biosciences). Analysis was performed using FlowJo 10 (Tree Star Inc., Ashland, OR).

3.4.8. Statistical analysis

All results are presented as means ± SE and assumed to be distributed approximately normally. The sample number represents the number of microvessel devices (ACV units) fabricated and analyzed unless otherwise noted. Single variable analysis with two-tailed t test assuming unequal variance was used to determine statistical significance between two samples for analysis of perfusability and endothelialization efficiencies. Two-way analysis of variance (ANOVA) was used to determine significance in population dynamics data, followed by Dunnett's multiple comparisons test.

Chapter 4. MULTIPHOTON-GUIDED CREATION OF COMPLEX ORGAN-SPECIFIC MICROVASCULATURE

Parts of this chapter have been published in the following manuscript: Rayner S*, **Howard C*,** Mandrycky C*, et al. "Multiphoton-guided creation of complex organ-specific microvasculature." Advanced Healthcare Materials, 2021[255]. *equal contribution

4.1. INTRODUCTION

Engineered tissues hold remarkable promise for both disease modeling and regenerative medicine[256,257]. The successful creation of functional tissues in vitro depends on adequate vascularization and perfusion. In vivo, tissues are supported by blood perfusion from interconnected three-dimensional (3D) capillary networks with diameters down to 5–10 μm[258]. Adding additional complexity, each human organ relies on structurally distinct microvasculature to support its unique hemodynamic and functional needs. As examples, the brain and heart contain a dense 3D network of thousands of capillaries per cm3 to support their high metabolic activity[259], kidneys filter blood via tortuous glomerular capillaries within a spherical space, and in the lung a thin sheet-like capillary network encircles spherical alveoli to maximize gas exchange[260].

Current technology faces challenges in replicating the scale, density, organ-specific complexity, and 3D curvature of native human capillary networks. Methods to create perfusable, cellularized vascular networks have included the casting of a hydrogel around a supportive material such as a needle[261], a lithographically defined mold[79,86], or a dissolvable material[83,262]. After hydrogel gelation, removal or dissolution of this supportive

material results in void spaces within the material into which cells can be introduced to form vascularized lumens. This can generate precise patterning but does not easily allow full 3D control over vascular geometry. Bioprinting addresses the need for complex 3D patterning[76,263], but lacks the resolution to create vascular lumens below ≈100 μm in diameter in cell-remodelable materials.

Multiphoton ablation is an emerging technique capable of patterning biomaterials with both high resolution and precise 3D control. By focusing ultrashort laser pulses within a hydrogel, high-energy multiphoton events occur principally at the focal point, leading to finely controlled material removal in 3D space. This technique has led to recent advances in the patterning of biomimetic vascular structures in multiple cell-compatible materials including collagen[91,264], poly (ethylene glycol)-based materials[77,265], silk fibroin[266], and specialized photodegradable polymers[231,267,268]. Degradation of these materials proceeds through different mechanisms depending on material composition and level of two-photon absorption[269]. Prior works have demonstrated creation of void-spaces with the diameter and geometry of human capillaries and the partial cellularization of larger photoablated lumens[77]. Despite these achievements, the endothelialization of 3D microvessels at the capillary scale is extremely challenging. Direct cell seeding into capillary-sized structures generally leads to luminal occlusion and patchy cell coverage. Drawing inspiration from previous reports on the directed migration of fibroblasts, cancer cells, or neural cells into ablated void spaces[264,268,270] we recently developed a technique, here termed “laser-guided angiogenesis,” where multiphoton ablation of linear channels extending from a pre-cellularized parent vessel guide endothelial cell growth and lead to perfusable endothelialized capillaries[91]. Here, we use multiphoton ablation approaches to

successfully create organ-specific microvascular structures that are cellularized, perfusable, and exhibit significant geometric complexity at anatomic capillary scale. Highlighting how our techniques enable new approaches to the study of vascular biology, we also demonstrate creation of proof-of-concept hierarchical and multicellular microvessels.

4.2. RESULTS

4.2.1. Multiphoton-guided creation of organ-specific vascular structures at anatomic scale.

Using a two-photon microscope, we first evaluated the ablation characteristics of three different materials commonly used for tissue engineering: collagen (7.5 mg mL−1), fibrin (10 mg mL−1), and a hydrogel containing 2% (w/v) each of agarose and gelatin. Two channels were formed lithographically within hydrogels and parallel conduits ablated between them using delivered laser powers at a wavelength (λ) of 800 nm ranging from 107 mW up to two exposures at 244 mW. Fluorescent beads were then perfused to evaluate patency (Figure 4.1a). In collagen and fibrin, laser powers of 157 mW or above led to complete ablation and the formation of a patent lumen with beads adherent only to the vessel wall. Agarose–gelatin gel required a power of 203 mW to generate perfusable structures, however hydrogel material remained incompletely ablated, as perfused beads were seen adherent throughout intraluminal spaces. For successive experiments we chose to use 7.5 mg mL−1 collagen, a laser power of 244 mW and two exposures to ensure full ablation. At these settings we ablated rectangles of decreasing width into collagen, demonstrating precise control down to at least 1 μm in resolution, consistent with previous reports[264,268].

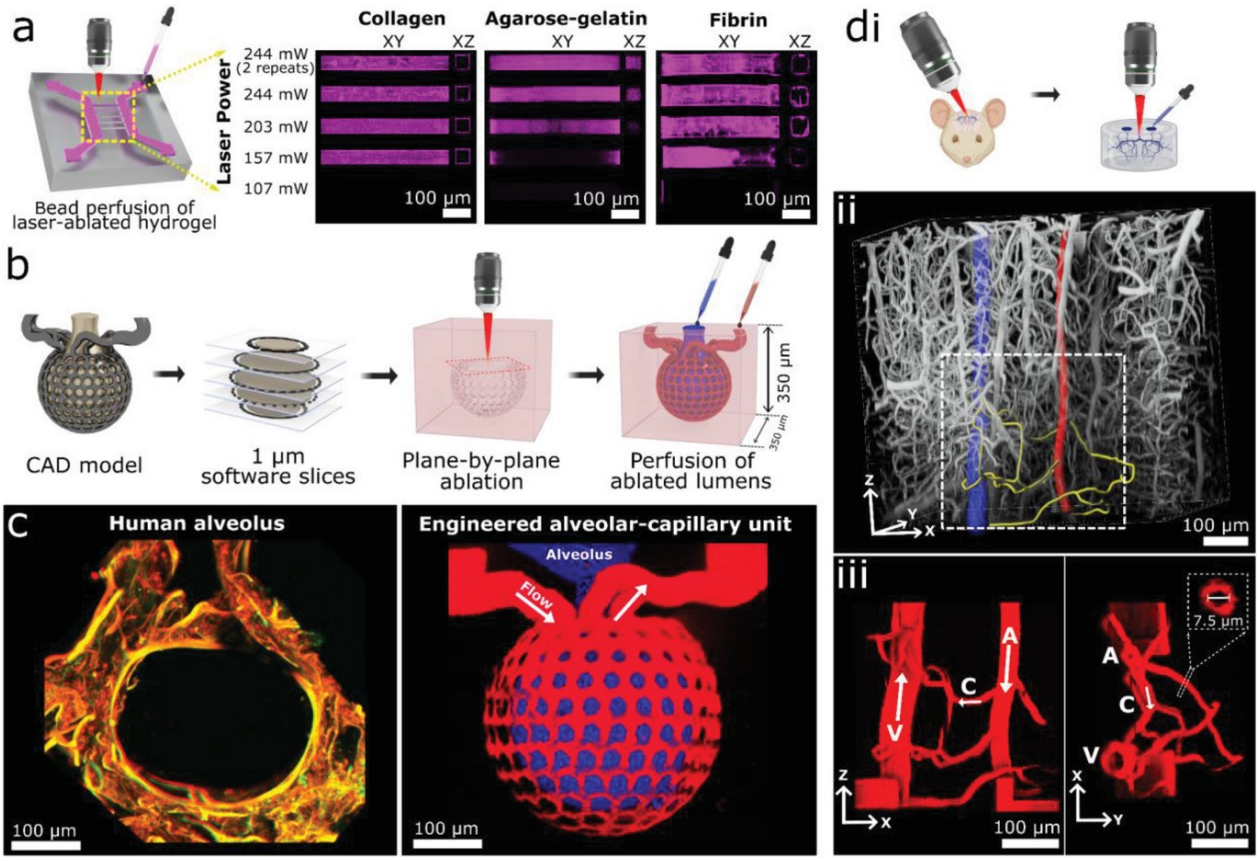

Figure 4.1 Multiphoton-guided creation of organ-specific vascular structures at anatomic scale.

a) Hydrogel photoablation. Images shown following perfusion of beads (magenta). b) Schematic of ablation and perfusion process. c) Two-photon images of a human alveolus (left), and an engineered alveolar-capillary unit after bead perfusion of capillary (red) and alveolar (blue) compartments (right). d) Recreation of mouse brain microvasculature. i) Schematic of using in vivo imaging data as a mask for ablation. ii) 3D microvascular image traced to isolate an arteriole (red), venule (blue), and capillaries (yellow). iii) Projection images of a replica microvascular unit ablated into collagen and perfused with beads (red). Orthogonal projections and capillary cross-section shown. Arrows delineate flow from arteriole (A), to capillaries (C), and venule (V).

We next developed a customizable process to use graphical data as a mask to guide the photoablation of complex 3D microvasculature in vitro (Figure 4.1b). This process allows facile control over laser intensity, pixel dwell time, and line-repeats for thousands of polygons bounding hundreds of thousands of XYZ points. Using this process, we demonstrated successful ablation of microvascular structures with increasing complexity into collagen hydrogel (Figure 4.1). Structures created in computer-aided design (CAD)

software were ablated either directly between an inlet and outlet or between a lithographically determined arteriole–venule unit[91]. We chose a helical pattern to demonstrate continuous curvature and smooth walls, and a meshwork pattern that highlights the achievement of two closely interwoven but separately perfusable channels. Ablation of each structure was completed in 10–30 min using the above-listed microscope settings, and faster speeds would likely be possible using a single scan, or a microscope with faster galvonometers and software to allow dwell times < 2 μs (the lower limit of our microscope)—using a laser with higher peak power if necessary to compensate for the reduction in dwell time. When perfused with fluorescent beads, the meshwork structure displayed its intended geometry, including a diameter of 10 μm for individual channels, and a separation of 15 μm between the two interwoven networks. Expanding on this approach, we then created a model of the lung alveolar-capillary unit at physiologic scale, consisting of a network of capillaries of 10 μm in diameter encircling an alveolus-like void space with a diameter of 300 μm. When perfused with fluorescent microbeads, the capillary and alveolar compartments remained distinct and separately perfusable (Figure 4.1C).

In vivo microvascular images have been used previously as masks to guide photoablation of lumens into PEGDA hydrogels with the density of human capillary beds, though to our knowledge perfusion of these structures at this scale has not been shown[77,271]. We extended this technique here into collagen hydrogels, and demonstrate controlled perfusion of a single microvascular unit. Using a multiphoton microscope, we imaged microvasculature in the cerebral cortex of a live mouse down to the capillary scale following perfusion of fluorescent dextran (Figure 4.1D). Obtained 3D images were used

as a mask for spatial control of laser ablation, leading to partial replication of the in vivo microvascular structures in collagen hydrogel. We then isolated a single microvascular unit from the above imaging data, consisting of an arteriole, capillaries, and a venule defined through filament tracing in Imaris software (Bitplane). Filaments were represented as cylindrical polygons, with a diameter of 7.5 μm used for capillaries. Using this as a mask, a replica microvascular unit was ablated into collagen and perfused with fluorescent beads (Figure 4.1D), demonstrating patent lumens and faithful recreation of the desired geometry.

4.2.2. Vascularizing a 3D glomerulus

We next combined these multiphoton ablation techniques with laser-guided angiogenesis to successfully vascularize a 3D kidney-specific microvascular structure—the glomerulus (Figure 4.2A). First we formed two parallel microvessels through established lithographic techniques and cellularized these structures with human umbilical vein endothelial cells (HUVECs)[79,91]. We then ablated a model glomerulus between these structures, consisting of channels (diameter = 10 μm) spherically encircled by an empty cavity modeling Bowman's space. Afferent and efferent channels were ablated to connect the glomerulus to the pre-formed parallel vessels. A pressure differential (≈1 mmHg) was applied across the glomerulus and maintained throughout culture. HUVECs were found to migrate into the lumens of the glomerulus within 24 h following ablation, and fully endothelialized the glomerular lumens by day 5–7 (Figure 4.2B). These vascular structures displayed an endothelial monolayer with VE-Cadherin junctions typical of healthy endothelium (Figure 4.2B). Perfusion of red blood cells demonstrated patent lumens, with single-cell transit observed in smaller capillaries (Figure 4.2B). Perfusion of FITC-labeled 500 kDa dextran

showed that the endothelialized glomerulus exhibits barrier function similar to that of the parent vessel. Future work is necessary to fully recapitulate the selective barrier function of the human glomerulus and this may require using glomerular endothelial cells, suitable hemodynamic conditions, establishing a glomerular basement membrane, and/or incorporating podocytes.

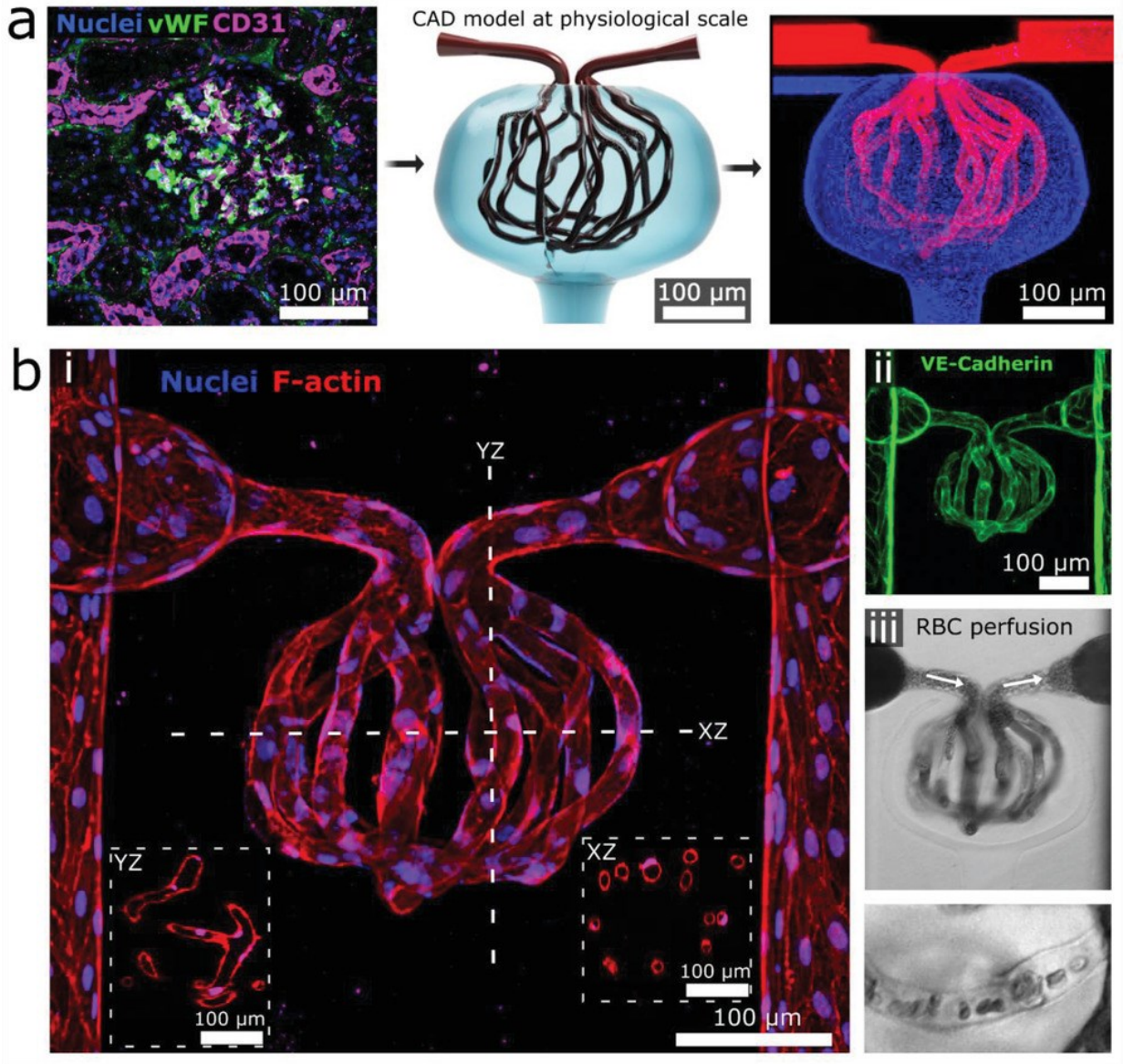

Figure 4.2 Creation of 3D cellularized microvessels.

a) A human glomerulus (left) informed creation of a CAD photomask (middle) for collagen ablation. Image (right) shows ablated structure following bead perfusion of capillaries (red) and Bowman's space (blue). b) Cellularized glomerular structure. i) 3D projection of glomerulus with inset cross-sectional views through the YZ and XZ plane, respectively; ii) VE-cadherin staining; iii) RBC perfusion, with magnified view showing single-cell transit (bottom).

4.2.3. Creation of heterogeneous, hierarchical, and multicellular vasculature

We next demonstrate how these fabrication methods can be used to create increasingly complex vasculature to explore long-standing vascular biology questions. This includes studies of vascular heterogeneity, the creation of hierarchical vessels, the vascularization of pre-cellularized tissues, and the patterning of human-derived matrix materials. Vascular heterogeneity is a key feature of human blood vessels. Even within a single vascular bed, discrete populations of cells exist in close proximity and interact while maintaining unique cellular phenotypes[19]. To demonstrate the potential of recreating and studying this phenomenon, we fabricated a six-compartment “color wheel” structure in collagen hydrogel. Compartments were cellularized with HUVECs labeled with one of six combinations of membrane dyes, grown for 48 h, and then connected via ablation to create one perfusable vascular structure with discrete (separately colored) segments. Cells grew into the area of ablation within 24 h and each segment remained patent without significant cell invasion into adjacent segments over the following 48 h (Figure 4.3A). Next, to re-create muscularized hierarchical microvasculature, a parallel arteriole and venule were first fabricated and cultured with primary human coronary artery smooth muscle cells labeled with mCherry (mCherry-SMCs) for three days, with media manipulated in a manner previously reported to encourage SMC quiescence[272]. Then a microvascular “grid” was ablated between the arteriole and venule and GFP-labeled HUVECs seeded throughout all channels, forming a robust endothelium after three further days of culture. This process led to the formation of a hierarchical microvascular unit

consisting of a muscularized arteriole and venule, connected by an intervening microvascular network lined only by an endothelial monolayer (Figure 4.3B). These structures provide a platform for future studies of microvascular tone and hierarchy.

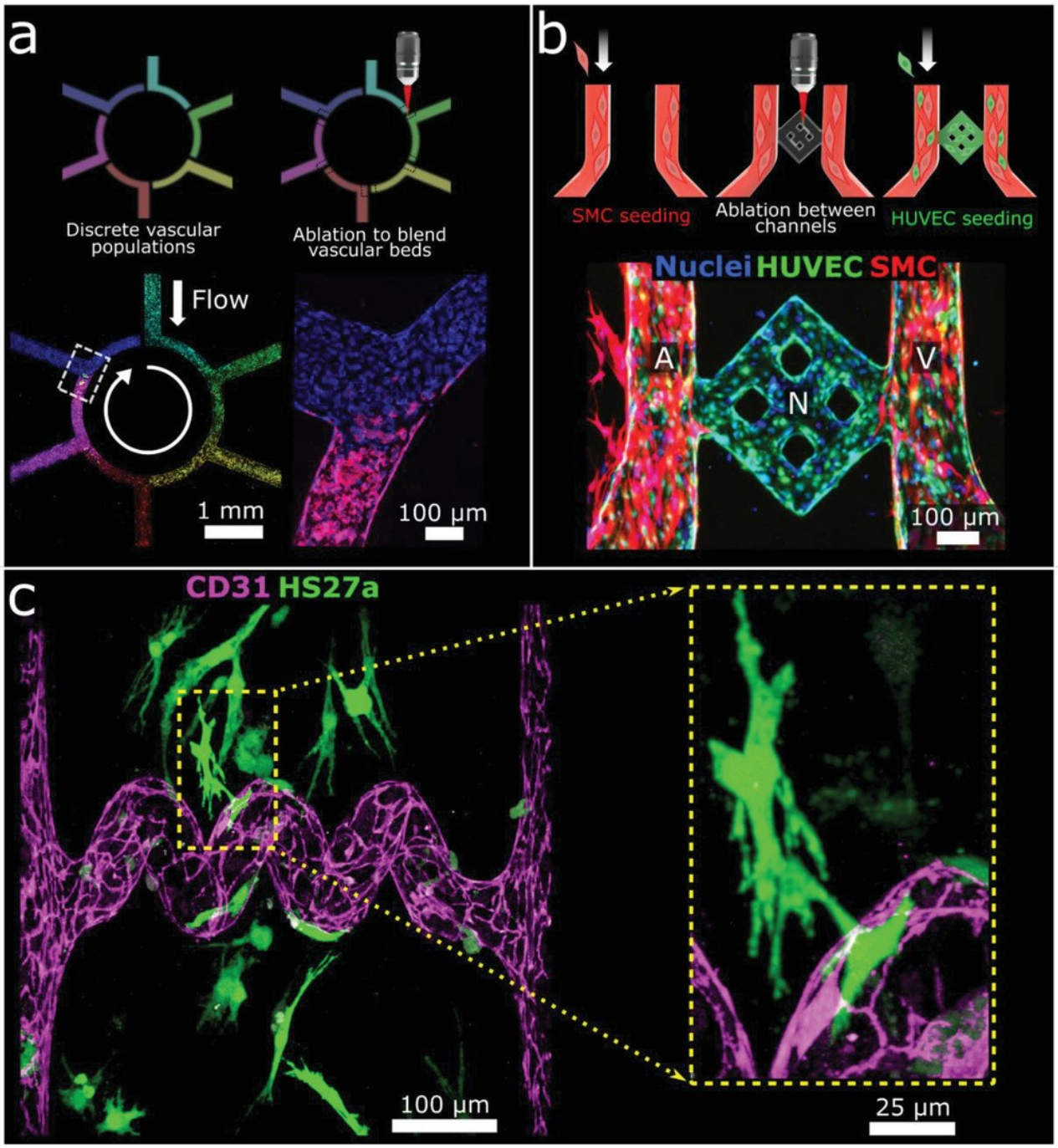

Figure 4.3 Creation of heterogeneous, hierarchical, and multicellular vasculature.

a) Heterogeneous vasculature fabrication. Images 24 h post-ablation (bottom) show a continuous vessel containing heterogeneous endothelial cell populations. b) Hierarchical vasculature creation. Image 72 h after HUVEC seeding (bottom) show a muscularized arteriole (A) and venule (V) connected by a microvascular network (N) lined by a HUVEC monolayer. c) Vascularization of cellularized tissue. Projection image following ablation of a “spiral” lumen into collagen containing HS27a-mCherry stromal cells (shown here in green) followed by seeding of HUVECs. Inset shows magnification of stromal cell/HUVEC association.

We then assessed whether ablation is compatible with the survival of cells embedded within matrices, with a focus on the future creation of vascularized parenchymal tissues. We showed that fluorescently labeled stromal cells (HS27a-mCherry) embedded within collagen matrices remain viable following ablation. In addition, HS27a cells near ablated channels appear to associate with newly created microvessels post-ablation (Figure 4.3C). As human tissue is composed of complex heterogeneous extracellular matrices, we sought to show that native human matrices could be ablated and used to create endothelialized microvessels. Our lab has previously derived and characterized human kidney extracellular matrix (kECM) as a material for microvessel fabrication[112]. Here, we ablated a grid structure extending from cellularized parent vessels within a blended hydrogel consisting of collagen (6 mg mL−1) and kECM (1 mg mL−1). Following ablation, HUVECs migrated into ablated lumens and were observed to remodel the ablated square structures into rounded vessels. The presence of kECM within the bulk matrix was verified via staining for collagen IV.

4.3. Discussion

Overall, we demonstrate the successful use of multiphoton ablation and laser-guided angiogenesis to create complex 3D cellularized microvessels in biological hydrogels with the scale and geometry of human capillaries. To our knowledge, the presented structures are unique in their combination of caliber, complexity, and cellularity, and could not easily be made via other techniques. All structures took less than 90 min to ablate, with no observed adverse effects on cell viability related to the duration of manufacturing when performed in a temperature-controlled environment. We demonstrated the ablation of several materials with relevance for the re-creation of human microvessels. In addition to

agarose–gelatin and fibrin, we have shown success using collagen and human decellularized matrices. Collagen is the most abundant protein in the human body, is cell-remodelable, and has been shown to support cellular growth in complex tissue constructs previously[75,230]. Collagen at 7.5 mg mL−1 has a Young's modulus of ≈500 Pa[273], within the range of human soft tissue/organs which have moduli from ≈100 Pa to hundreds of kPa[274]. We also provide multiple examples showing how multiphoton ablation can be used to replicate key features needed to develop microphysiologic models of increased complexity: cellularization at the capillary scale, perfusability, cellular heterogeneity, vascular hierarchy, and vascularization of pre-cellularized tissue. Cells within our models show expected behavior including barrier function and interaction with newly created lumens.

The ability to rapidly make perfusable, cellularized microvessels with customizable geometry will have immediate utility for organ-on-a-chip research and tissue engineering for regenerative medicine and disease modeling. Future work will be necessary to reach the eventual goal of patterning complex functional microvessels in dense tissue. Combining photoablation with bioprinting is an especially intriguing possibility for the rapid creation of vascularized organ tissue.

4.4. Materials and Methods

4.4.1. Microscope System and Settings

A 2.5 W titanium-sapphire laser (Mai Tai HP, Newport) with a pulse duration of < 100 fs and repetition rate of 80 Mhz attached to a multiphoton microscope (FV1000, Olympus) and focused through a 25×1.05 NA objective (XLPlan N, Olympus) was used for ablation experiments. Dwell time 2 μs per scan and λ = 800 nm were used for ablation, with pixel

size set to 497×497 nm for most experiments. Maximum power exiting the objective was 244 mW at 800 nm.

4.4.2. Ablation and Perfusion

CAD models (Fusion 360, Autodesk) or in vivo volumetric imaging data were converted to 3D meshes, sliced into 1-μm-thick layers (Netfabb, Autodesk), and exported as vector graphics. Custom R[30] script (https://git.io/JfXFi) imported vector graphical data and ablation parameters into Fluoview software (Olympus) to drive multi-area microscope scanning. Lithographically determined microvessels were created as previously described[79,91]. Collagen and kECM matrix were manufactured in house from rat tails or human kidney, respectively[112,275]. Bead perfusion was with 100 nm beads (FluoSpheres, ThermoFisher) and blood for perfusion was obtained from healthy volunteers. Cells were used from passages 4–6. For dextran perfusion, 1 μм) 500 kDa FITC-dextran (Sigma) was perfused into microphysiological systems under real-time imaging, using a perfusion pressure of 1 cm H2O. For the “color wheel,” HUVEC aliquots were stained with membrane dyes (Sigma Aldrich): green (PKH67), red (PKH26), claret (“Cellvue Claret”), or a combination.

4.4.3. Tissue Staining and In Vivo Experiments

Human renal cortex (LifeCenter Northwest) was stained for von Willebrand Factor and CD-31 and imaged. Rejected donor lungs (National Disease Research Interchange) were imaged for tissue autofluorescence. Cerebral cortical microvasculature in a live 4-month-old C57Bl6 mouse was imaged following fluorescent dextran perfusion, via chronic cranial

window[276]. Using filament tracing (Imaris, Bitplane), a microvascular unit was traced, with capillary filaments represented as cylinders (diameter = 7.5 μm). Animal studies were approved by Seattle Children's Research Institute IACUC (IACUC00396). Human blood samples were approved by the Institutional Review Board of the University of Washington (#45624-EA).

4.4.4. Statistics

Laser power determinations were made on two separate occasions and averaged. All cellularized structures were made in at least triplicate, with representative images shown.

Chapter 5. INFLAMMATORY AND IMMUNE RESPONSE OF ENGINEERED HUMAN BRAIN MICROVESSELS TO *PLASMODIUM FALCIPARUM* BINDING

5.1. INTRODUCTION

Malaria is a global burden with 241 million cases occurring worldwide and over 627,000 deaths annually[119]. Over 90% of the world's malaria mortality is caused by infection with *Plasmodium falciparum*. Severe cases of *P. falciparum* infection can progress to cerebral malaria (CM), characterized by infected red blood cells (iRBCs) sequestering in the brain microcirculation, endothelial cell dysfunction, vascular leakage, and cerebral inflammation[121,277] Vascular dysfunction contributes to brain swelling and localized hypoxia which can lead to neurological problems, coma, and in the most severe cases death[278,279]. While brain microvasculature plays a key role in cerebral malaria, the specific events which initiate pathological progression are not well understood.

P. falciparum iRBCs adhere to brain endothelial cells through interactions between *P. falciparum* erythrocyte membrane protein 1 (PfEMP1) ligands and endothelial cell surface receptors such as endothelial protein C receptor (EPCR) and intercellular adhesion molecule 1 (ICAM1)[90,124,127,128,152,157]. Histological examination of fatal pediatric cerebral malaria cases has revealed sequestered iRBCs, ring hemorrhages, microthrombi, fibrin deposits, and the presence of infiltrating monocytes, some of which have phagocytosed malaria pigment[278,280]. In addition to microvascular obstruction, CM is associated with systemic inflammation and widespread endothelial cell activation[129]. Several pro-inflammatory cytokines and chemokines correlate with CM severity including tumor necrosis factor α (TNFα)[136], interferon-γ (IFN- γ)[281] and CXCL10[282]. Under these inflammatory conditions systemic activation of endothelial cells has been demonstrated

through increased serum levels of soluble adhesion molecules VCAM-1 and ICAM-1[129]. Endothelial activation may promote leukocyte binding and accumulation in cerebral microvasculature and can also lead to increased permeability and the induction of the coagulation cascade.

Additionally, the close juxtaposition of adherent iRBCs and endothelial cells may promote localized pro-coagulant and pro-inflammatory processes and lead to focalized barrier leakiness. Postmortem studies have shown there is a localized deposition of fibrin near sequestered iRBCs and the reduction of EPCR and thrombomodulin on endothelial cells[283], two important receptors in the protein C pathway which functions as a regulator of coagulation, inflammation, and barrier function. In a normal vessel, thrombin initiates activation of protein C which binds to EPCR and triggers protective anticoagulant and anti-inflammatory pathways[132]. EPCR-binding parasite variants compete with activated protein C for this binding which leads to unimpeded procoagulant and barrier disruptive effects from thrombin[151,152,229,284]. As adherent iRBCs mature in situ and during iRBC rupture, they release pro-inflammatory factors, such as extracellular vesicles[133], hemozoin pigment (a polymer of heme that accumulates as a byproduct of parasite digestion of hemoglobin)[120], parasite histones[134], and histidine-rich protein 2[135]. These factors are concentrated near endothelial cells in areas of sequestered iRBCs and some have been shown to act directly on endothelial cells leading to endothelial cell activation and barrier disruptions. There are strong correlations between microthrombi, sequestered iRBCs, and vascular leakage of fibrinogen implying that multiple factors may contribute to endothelial cell activation and dysfunction in cerebral malaria[277].

Together, there is evidence that iRBC sequestration, parasite factors, host inflammatory factors, and dysregulated coagulation pathways are all likely contributors in the progression of CM. As endothelial cells are critical moderators of these signals, there is a need for better understanding the effects of these stimuli on brain endothelial cells. Previous studies using endothelial cell monolayers have demonstrated that iRBC binding alone can directly induce ICAM-1 expression on human brain microvascular endothelial cells (HBMECs)[130], increase permeability[159], and induce numerous immune and inflammatory pathways[285]. However, there has been limited examination of the endothelial cell response to adherent iRBCs as they mature *in situ* and how the endothelial cell response is affected by previous exposure to host proinflammatory cytokines. Previously, we demonstrated the utility of 3D engineered microvessels for determining the roles of host receptor interactions to parasite binding in a model which replicates appropriate 3D geometry and flow[85,90]. We optimized this model to allow for iRBCs adhered to the brain endothelial cells to mature through rupture over 24 hours of co-culture. By probing the endothelial cell response at multiple stages of parasite maturation and following perturbations with thrombin or TNFα, we have gained novel insight into the early morphological, transcriptional, and functional effects that iRBCs and host pro-inflammatory factors induce in engineered 3D human brain microvessel models.

5.2. RESULTS

5.2.1. An engineered human 3D brain microvessel model for studying different densities of parasite-vessel wall interaction

To be able to evaluate the response of brain endothelium to various stimuli, we employed the use of a microvessel model with a 13-by-13 grid geometry and a diameter of 100 μm at each segment. The vessel is fabricated using a combination of soft lithography to create

positive-feature molds of the network out of polydimethylsiloxane (PDMS) which are then used to imprint into a collagen hydrogel using injection molding (Figure 5.1A). The networks are housed in acrylic pieces with inlet and outlet reservoirs allowing for perfusion through the system using a pressure differential in the reservoirs. The channels are seeded with primary human brain microvascular endothelial cells (HBMECs) which adhere to the walls and form a confluent lumen over 2-4 days of tissue culture. The geometry of the network allows for a large surface area of HBMECs with robust junctions as seen by staining for VE-cadherin (Figure 5.1B). As the 3D microvessel forms, the HBMECs remodel the collagen matrix to form rounded channels (~100-120 μm internal diameters) which are confluent in 3D as shown by cross-sectional slices (Figure 5.1B). The 3D vessel provides an *in vivo* mimicking platform for evaluating pro-inflammatory and pathological stimuli on brain endothelial cell activation and function.

The bifurcating 13 X 13 grid design also allows for a range of flow velocities and wall shear stresses to be present in a single vessel. With one inlet and one outlet, at each bifurcation and subsequent increasing branching order the flow rate and wall shear stress decreases from the previous branch until reaching a minimum at the corners of the grid opposite to the inlet and outlets. Previous work has demonstrated that *P. falciparum*-iRBCs have flow-dependent binding patterns in this system leading to higher densities of parasite binding in the corners and lower binding levels towards the inlets and outlets where wall shear stresses are higher[90]. Because having a range of levels of iRBC binding within one vessel would allow for the screening of the effects of iRBC binding density on endothelial cells, this flow-dependent binding pattern is advantageous. Here, we studied IT4var19, a clonal parasite line that was originally selected on brain endothelial cells and

expresses a PfEMP1 variant that binds to endothelial protein C receptor (EPCR), a receptor linked to cerebral malaria. We confirmed that perfusing IT4var19 iRBCs through a branching brain microvessel under gravity-driven flow for 1 hour followed by a media rinse resulted in a flow-dependent pattern of binding (Figure 5.1C). By counting the number of adhered iRBCs in each straight segment (l = 300-350 μm, d = 90-120 μm) or branching node (l = 130-150 μm, d = 90-120 μm) a heatmap of average number of bound iRBCs per vessel region across N=3 replicates shows the distribution (Figure 5.1C, right). Towards the corners, there are ~80-120 bound iRBCs per segment compared to ~0-30 bound iRBCs per segment towards the inlet and outlet. This equates to an average range of around 0.7-2 iRBCs per endothelial cell in the highest binding regions and 0-0.4 iRBCs per endothelial cell in the lowest binding regions. However, within regions there is also a heterogeneous distribution of binding and a single endothelial cell can often have its entire surface covered by bound iRBCs (5-10 iRBCs per endothelial cell) (Figure 5.1C). From an autopsy study examining the number of parasites per capillary in patients with clinical cerebral malaria, a range of 0-7 parasites per capillary cross-section, defined as a cross-section with no more than one endothelial cell nucleus per region, was found[173]. This indicates that the density of iRBCs in the highest-binding regions of the grid results in a ratio of iRBCs::endothelial cells that is on the same order as is seen in patients.

Ultrastructural evaluation by scanning electron microscopy at 1 hour after iRBC perfusion reinforced the two patterns of iRBC binding (Figure 5.1D). The vessel wall appears slightly bumpy with infolds/outfolds in the membrane lining (Figure 5.1D, i). The iRBCs bound either in a scattered pattern along the length of the vessel segment (Figure 5.1D, ii and iii) or in a cluster with many bound iRBC cells in contact with each other (Figure 5.1D, iv).

From videos, the clusters start as a single bound cell and grow one iRBC at a time over the course of the perfusion.

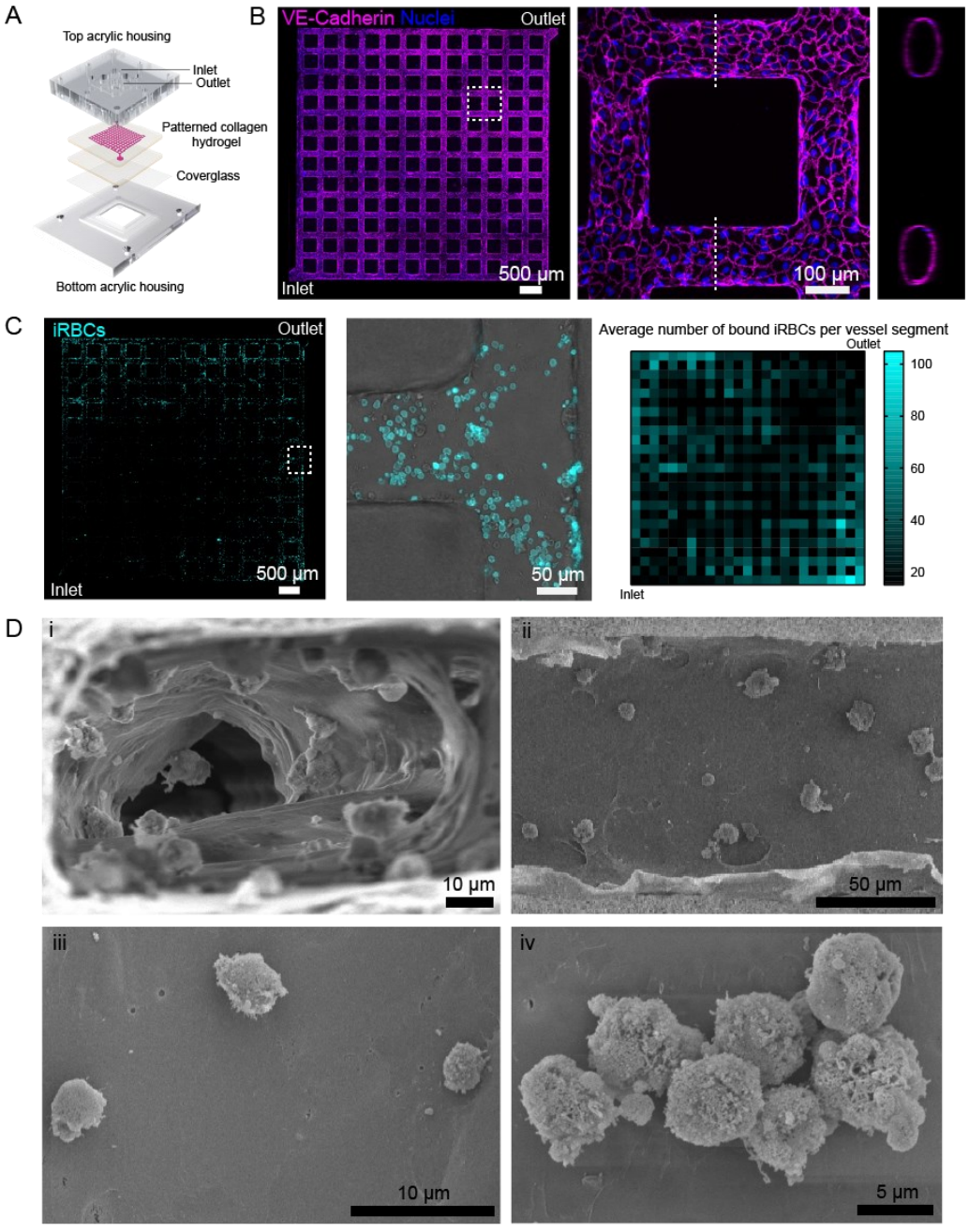

Figure 5.1: Engineered human 3D brain microvessels permit study of *P. falciparum* infected red blood cell (iRBC) binding at different densities across a 13 X 13 grid design.

(A): 3D brain microvessels are fabricated by injection molding of a collagen hydrogel forming a 13 X 13 grid network of empty channels (d = 100-120 μm). Channels are housed between acrylic pieces with inlets and outlets and allow for the perfusion of HBMECs which adhere to the vessel walls. **(B)**: Left: HBMECs form

confluent lumens with robust junctions as shown by VE-cadherin staining. Right: HBMECs remodel to form rounded lumens as depicted in cross-sectional view. **(C):** Right: Representative image of the binding distribution of fluorescently labeled iRBCs adhered to the HBMECs in the microvessel after 1 hour of perfusion followed by a media wash. Middle: Brightfield image showing vessel outlines with overlay of fluorescent iRBCs. Right: Heatmap showing the spatial distribution of bound iRBCs as the average number of iRBCs adhered in each vessel segment (n=3). **(D):** Representative scanning electron microscopy images of a brain microvessel after 1 hour of iRBC perfusion. (i): Cross sectional view of vessel lumen has a bumpy endothelial cell surface with infolds/outfolds and many bound iRBCs. (ii and iii): Top down longitudinal view of vessel lumen shows scattered binding of iRBCs. (iv): Top down longitudinal view of iRBCs adhered to vessel wall in an aggregate.

5.2.2. P. falciparum iRBCS undergo maturation in situ

To evaluate how endothelial cells respond to iRBC binding over time, we optimized co-culture conditions to promote *in situ* maturation. The average blood stage lifecycle of *P. falciparum* iRBCs is 48 hours (Figure 5.2A). During infections, immature ring-stage iRBCs circulate in peripheral blood for approximately 8-20 hours post-invasion (hpi) and then adhere to endothelial cells to avoid splenic clearance while continuing to mature[286]. To mimic this, we isolated trophozoite-stage iRBCs from a suspension culture between 25-33 hpi before perfusing them through the 3D brain microvessels. To promote parasite maturation, we supplemented the 3D microvessel culture media with 5% human serum. We evaluated the vessels at 1, 8, and 24 hours post-perfusion to confirm the adherence of iRBCs and the continuation of maturation *in situ*.

At 1 hour post-perfusion, iRBCs adhered to the vessel wall in a scattered or clustered pattern as shown by brightfield microscopy (Figure 5.2B, ii, left). By collecting the effluent from the outlet of the vessel after rinsing with media at 1 hour and Giemsa staining, the presence of mid trophozoite stage parasites with enlarged cytoplasm and a single nuclei was confirmed. At 8 hours post-perfusion, the adhered iRBCs have continued to mature to late stage trophozoites. By brightfield microscopy stained with Hoescht, some parasites have begun segmentation of nuclei (Figure 5.2B, ii, middle) and Giemsa staining of the effluent from the outlet following a media rinse (Figure 5.2B, i, middle) showed iRBCs

have grown in size and brown hemozoin pigment from digestion of hemoglobin is evident. By 24 hours post-perfusion, some iRBCs have matured to rupture. By collecting the effluent at the outlet and Giemsa staining, loose merozoites can be seen indicating that the iRBCs have ruptured (Figure 5.2B, i, right). By brightfield microscopy with Hoescht staining, clusters of small nuclei not within an obvious membrane are often seen, indicating a rupture has released loose merozoites (Figure 5.2B, ii, right).

Scanning electron microscopy confirms the *in situ* iRBC maturation. At 1 hr post-perfusion, iRBCs are rounded with small attachment points to endothelial cells (Figure 5.2B, iii and iv left). At 8 hours post-perfusion, iRBCs have flattened membranes at the attachment points with increased surface area directly in contact with endothelial cells (Figure 5.2B, iv, middle). By 24 hours post-perfusion, fragments of ruptured ghost iRBC membranes remain attached to the endothelium, often with loose merozoites nearby (Figure 5.2B, iv, right). Collectively, this analysis indicates that iRBCs grew and matured over the first 8 hours and many iRBCs progressed until rupture at 24 hours.

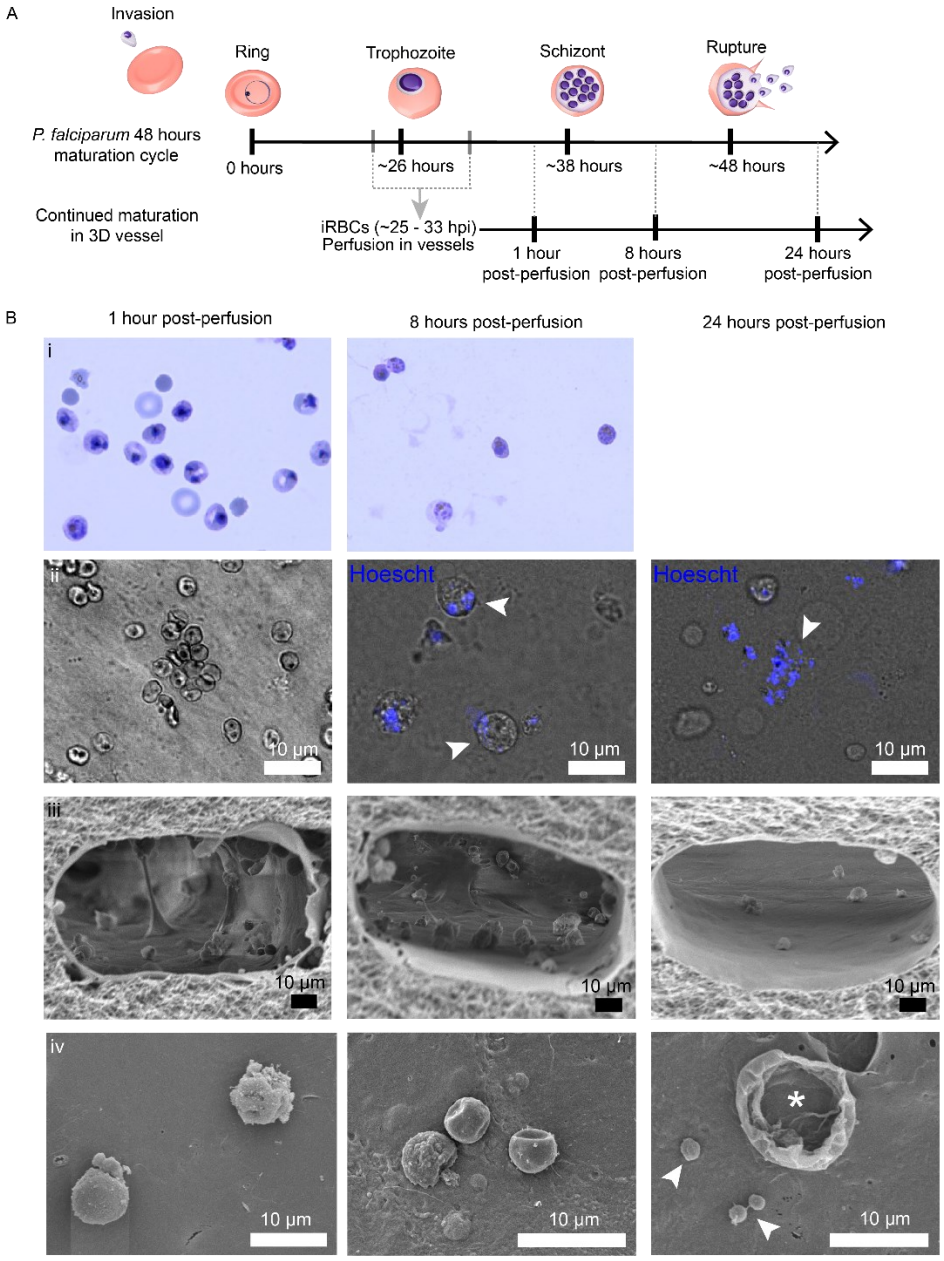

Figure 5.2*: P. falciparum* infected red blood cells undergo in situ maturation in 3D microvessels.

(A): Timeline of *P. falciparum* iRBC maturation cycle. Trophozoite-stage iRBCs between 25 and 33 hpi were perfused through the brain microvessels where they adhere to the endothelium and continue to mature *in situ*. **(B)**: Representative images showing progression of parasite maturation at 1 hour, 8 hours, and 24 hours post-perfusion. (i): Representative smears of the effluent collected at the outlet of the vessels at each time point. Left: At 1 hour, many mid trophozoite stages are present. Middle: At 8 hours, iRBCs have matured and brown hemozoin pigment is present. Right: At 24 hours, some iRBCs have ruptured leading to many free merozoites. (ii): Representative brightfield images at each time point. Left: At 1 hour, many iRBCs have bound. Middle: At 8 hours, iRBCs have matured and some have segmented into multiple nuclei as shown by Hoechst staining (arrowhead). Right: At 24 hours, some iRBCs have ruptured leading to the presence of clusters of loose merozoites (arrowhead). (iii) Representative scanning electron microscopy of

cross sectional views of vessel lumen at each time point. (iv): Scanning electron microscopy images of infected erythrocytes bound to vessel wall at each time point. Left: iRBCs bound to endothelial cells after 1 hour of perfusion. Middle: bound iRBCs at 8 hours have flattened membrane contact with endothelial cells. Right: At 24 hours, remnants of a ruptured iRBC with fragments of ruptured membrane still bound to endothelial cells (asterisk) and loose merozoites nearby (arrowheads).

5.2.3. Brain endothelial cells have ultrastructural changes due to stimulation by thrombin, TNFα, and P. falciparum iRBCs

Multiple host and parasite factors likely contribute to endothelial cell dysfunction and disruptions in the blood brain barrier. To begin evaluating the endothelial cell host-response, we looked at the ultrastructural changes of brain endothelial cells to treatment with three stimuli: (1) thrombin, an enzyme in the coagulation cascade which cleaves fibrinogen to fibrin and promotes disruption of endothelial cell junctions, (2) TNFα, an inflammatory cytokine which can induce endothelial cell activation and immune cell recruitment and is increased in patients with malaria, and (3) *P. falciparum* iRBCs at 1, 8, and 24 hrs after attachment.

Treatment with thrombin induced dramatic changes in barrier integrity and limited changes in endothelial cell surface phenotype. By 15 minutes of treatment, endothelial cell junctions had pulled apart and gaps formed between many but not all contact points between endothelial cells (Figure 5.3A). Large gaps and fissures up to 50 to 100 μm in length and between 1-3 μm in width appeared between cells exposing the underlying collagen matrix. Despite the obvious disruption to the barrier, the endothelial cell surface remained smooth. By 2 hours of treatment with thrombin, the endothelial cell junctions had further deteriorated. Gaps between cells were longer, often making up most of the cell circumference (Figure 5.3B, left) and gaps were wider, ranging up to 5-10 μm in width (Figure 5.3B, right).

By contrast, treatment with TNFα induced more substantial changes in endothelial cell surface phenotype than barrier integrity. By 8 hours post-treatment, the endothelial cell surface appeared slightly bumpy (Figure 5.3C, left). The surface of the endothelial cells had the appearance of many microparticles, and at the junctions there were filamentous cellular extensions ranging up to 5 μm in length (Figure 5.3C, right). Additionally, the luminal surfaces remained intact but there were areas which had small punctate holes <1 μm in diameter which were often near the junctions between endothelial cells, potentially indicating a focal barrier disruption, though not as drastic as treatment with thrombin.

Parasites induced distinct endothelial cell phenotypes from the two host pro-inflammatory stimuli. By 8 hours of iRBC adherence in the vessel, the endothelial cell surface phenotype had changed with many similar features seen from TNFα treatment. The appearance of the endothelium looked bumpy (Figure 5.3D, i). Some endothelial cells had the appearance of many microparticles as well as the filamentous cellular extensions, similar to TNFα treated vessels (Figure 5.3D, ii). However, where the TNFα treatment caused a homogeneous phenotype, the iRBC stimulated vessels had a heterogeneous and patchwork appearance with some cells displaying microparticles and filamentous extensions and adjacent cells often appearing smooth and without alterations. While the cellular extensions appeared in areas with or without iRBCs adhered, there were numerous examples of adherent iRBCs with multiple endothelial filamentous extensions in direct contact (Figure 5.3D, iii and iv). Like the TNFα-treated microvessels, the luminal vessel walls were largely intact. However, occasional punctate gaps either within cell bodies (Figure 5.3D, iii) or along the junctions between endothelial cells (Figure 5.3D, v) were present. These focal disturbances were sometimes but not always present directly

next to iRBCs. By 8 hours, many of the adhered iRBCs had more surface area of their membranes in direct contact with the endothelial cells and often would look flattened (Figure 5.3D, vi), indicating a possible tighter adherence or more protein-protein interactions between the cells.

By 24 hours of iRBC cytoadherence, the endothelial cell phenotype changes became more pronounced. The patchwork pattern of microparticles on the surface of endothelial cells remained, with the microparticles sometimes looking denser and larger than at 8 hours (Figure 5.3E, i). Many iRBCs have ruptured leaving behind ghost iRBC membrane fragments attached to the endothelial cells (Figure 5.3E, i, iv, v, and vi). Loose merozoites which have flattened spherical shapes between 1-2 μm in diameter are often seen near the remnants of ruptured membranes (Figure 5.3E, i. vi). Remaining intact iRBCs were larger, sometimes closer to 10 μm in diameter with irregular shapes (Figure 5.3E, i, ii, iii, and vii). Cellular extensions reaching towards or directly contacting iRBCs were still present (Figure 5.3E, ii, iii, vii, and ix). Unique to the 24 hour timepoint were the appearance of many apoptotic endothelial cells characterized by the bulging of their membranes (Figure 5.3E, ii, iii, viii, and ix). The apoptotic endothelial cells were sometimes in direct contact with an iRBC (Figure 5.3E, ii, ix) but not always (Figure 5.3E, iii, viii). The appearance of small punctate holes in the endothelium were again present, sometimes along the junctions between cells (Figure 5.3E, vii), near an apoptotic endothelial cell (Figure 5.3E, viii), or beneath bound ruptured ghost iRBC membrane fragments (Figure 5.3E, v). Together, these morphological changes indicate that the endothelial cells are responding to the bound iRBCs at both 8 and 24 hours with some phenotypic similarities to stimulation by TNFα treatment (microparticles, punctate gaps,

and cellular extensions) but in a more heterogeneous pattern. Additionally, by 24 hours the bound iRBCs have triggered an apoptotic response with many apoptotic endothelial cells appearing which weren't seen at the 8 hour timepoint or in any other treatment condition.

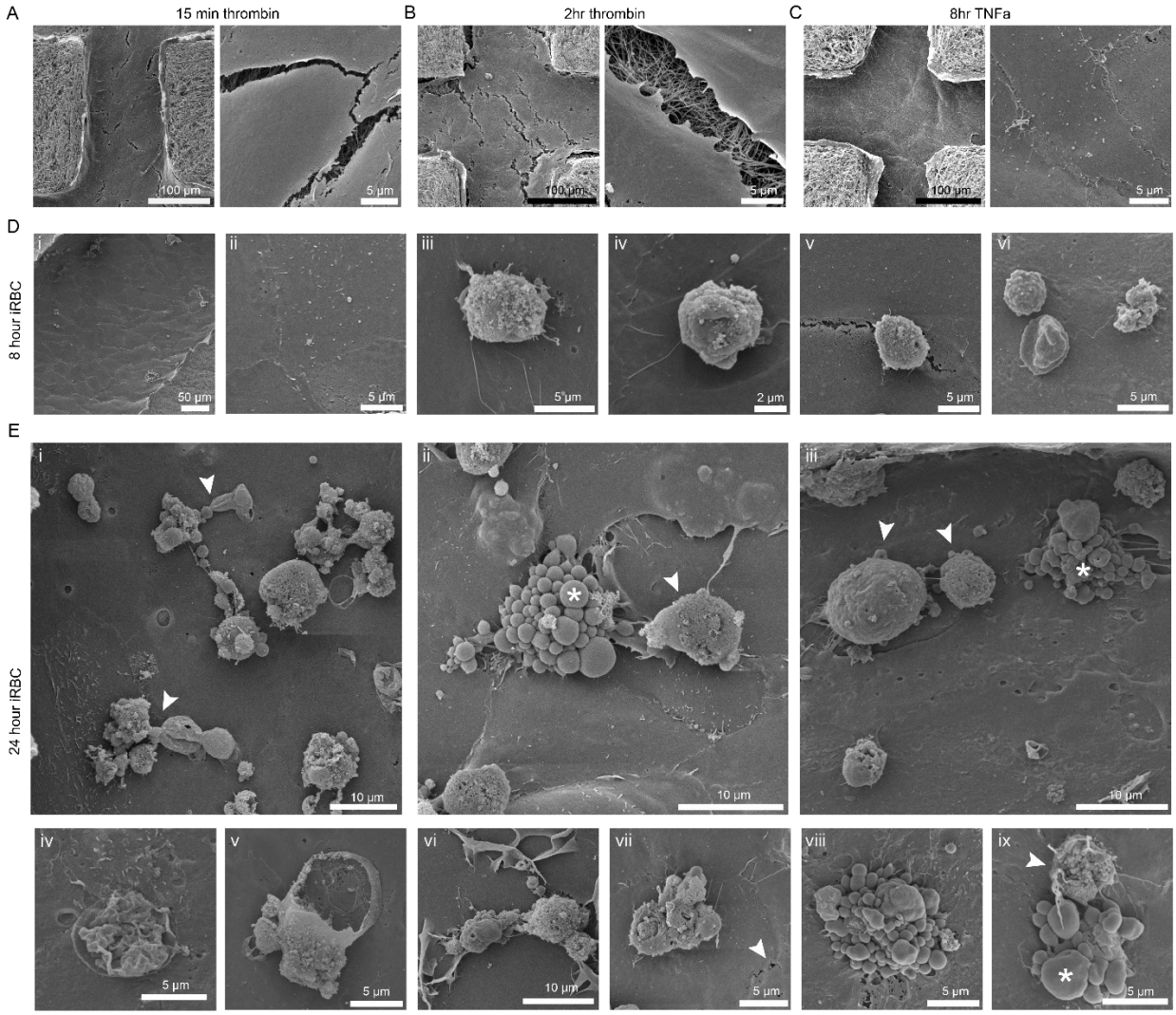

Figure 5.3: Scanning electron microscopy reveals different endothelial cell phenotypes following perfusion of 3D human brain microvessels with thrombin, TNFα, and *P. falciparum*-iRBCs.

(A): Treatment with thrombin for 15 minutes leads to extensive barrier disruption seen as gaps forming between endothelial cell junctions and large fissures between cells. **(B):** Treatment with thrombin for 2 hours further disrupts the barrier as seen by the presence of more and widening gaps between endothelial cell junctions. **(C):** TNFα induces minimal barrier disruption characterized by punctate gaps between cell junctions and cell surface changes characterized by the appearance of microparticles and the appearance

of filamentous cellular extensions arising from the borders of cells. **(D)** By 8 hours of iRBC adherence to the brain microvessel, the endothelial cell morphology has changed. (i): Vessel surface is bumpy with slightly raised endothelial cells. (ii): Some endothelial cells have acquired microparticles on the surface, filamentous cellular extensions arise from the borders of cells, and small punctate holes are found both between cell junctions and within cell bodies. (iii and iv): Filamentous cellular extensions are often reaching towards or making contact with iRBCs. (v): iRBCs are occasionally near minor junctional disruptions. (vi): iRBCs have often flattened with a high surface area of the membrane in direct contact with endothelial cells. **(E):** By 24 hours of iRBC adherence to brain microvessels, endothelial cell morphology has further deteriorated. (i): Field of view depicting heterogeneous appearance of microparticles and cellular extensions on some but not all endothelial cells. iRBCs have grown in size with some rupturing leaving behind ghost iRBC membranes and loose merozoites (arrowhead). (ii and iii): Apoptotic endothelial cells (asterisk) either near or in direct contact with iRBCs (arrowheads). (iv, v, and vi): Ruptured iRBC membrane fragments remain attached to endothelial cells. (vii): iRBCs have grown, have extensions from endothelial cells reaching towards them, and are near microparticles on the surface of endothelial cells and punctate junctional disruptions (arrowhead). (viii): Closeup of apoptotic endothelial cell. (ix): Apoptotic endothelial cell (asterisk) with iRBC (arrowhead) directly attached.

5.2.4. Endothelial cells have distinct transcriptional changes due to stimulation by TNFα and P. falciparum iRBCs

To investigate the transcriptional response of brain endothelial cells to pathological stimulants, we performed RNA sequencing (RNA-seq) on bulk RNA collected from whole vessels from 8 different treatment groups (schematic in Figure 5.4A). To evaluate the response of brain endothelial cells to an inflammatory cytokine present in *P. falciparum* malaria, half of the vessels were treated with TNFα for 18 hours and half were fed regular media to maintain an unstimulated “resting” state. After the 18-hour treatment, vessels were rinsed with media and were perfused with either iRBCs (denoted “parasites”) or normal red blood cells (RBCs) at the same concentrations for 1 hour. Following the 1-hour perfusion, all vessels were rinsed with media to remove unbound RBCs and iRBCs and were left to culture for either 8 or 24 hours. At these timepoints, a lysis buffer was perfused through the vessels to collect the RNA and samples were sequenced by bulk RNA-seq.

Principal component analysis (PCA) of the gene expression data showed that the replicates clustered by treatment condition, with the largest change from baseline occurring by TNFα treatment (Figure 5.4B). Using the K-means clustering algorithm on the 2000 most differentially expressed genes across all conditions, the differentially expressed genes can be clustered into 4 groups (Figure 5.4C). Broadly, clusters A, C, and D have the strongest separation by resting vs. TNFα treatment, and cluster B has separation by RBC vs. parasite perfusion. Gene Ontology (GO)-enriched biological process pathways showed differences in enriched pathways of each cluster (Figure 5.4D). Cluster A, which broadly represents genes downregulated by TNFα treatment compared to resting baseline contains terms such as cell migration, vasculature development, and angiogenesis, indicating that TNFα treatment leads to the downregulation of basic functions of quiescent vasculature. Cluster B, which broadly separates perfusion by RBCs vs parasites within conditions contains terms such as protein targeting to ER, establishment of protein localization to membrane, and ATP metabolic process. These indicate that there are potentially changes in cellular metabolism and protein functions associated with iRBC cytoadherence. Clusters C and D which broadly represent genes upregulated from TNFα treatment compared to baseline contain terms such as defense response, immune response, and cytokine-mediated signaling pathway. This indicates that the TNFα treatment has induced a global inflammatory and defense response which is still present 27 hours after the initial stimulation with TNFα and 8 hours after the stimulation has stopped.

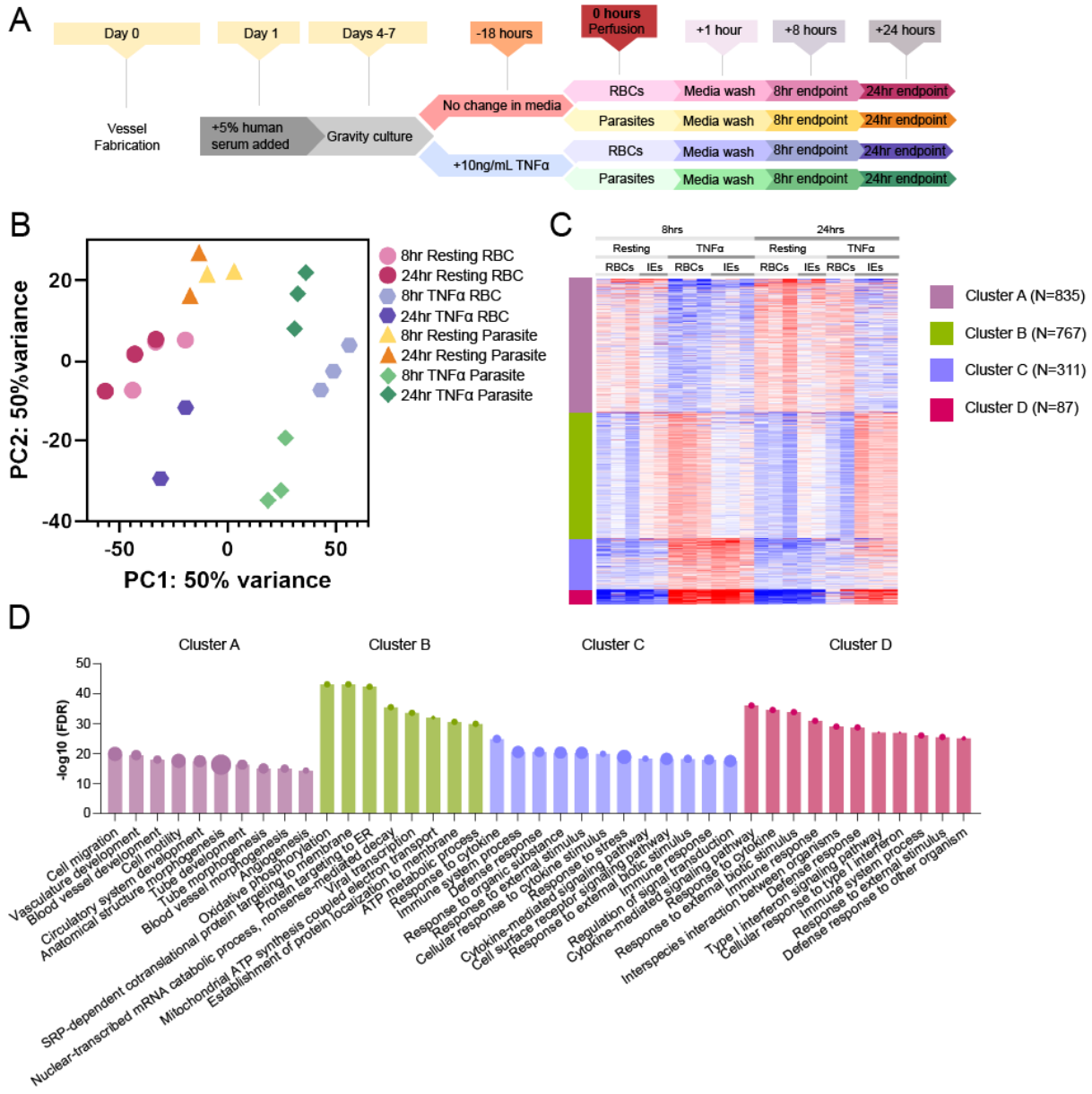

Figure 5.4: 3D brain microvessels have distinct transcriptional changes due to stimulation by TNFα and *P. falciparum*-iRBCs as evaluated by RNA-seq.

(A): Diagram of experimental conditions for the eight groups evaluated. Treatment with TNFα begins 18 hours before perfusion with either RBCs or iRBCs. RBCs and iRBCs are cultured in the vessels for 8 or 24 hours before isolation of RNA. **(B):** Principal component analysis (PCA) plot of RNA-seq data from 8 experimental conditionals (N=2-3). **(C)**: Heatmap of the 2000 most differentially expressed genes divided into 4 clusters by the K-means clustering algorithm. **(D):** GO Biological Process pathways enriched within each cluster.

5.2.5. TNFα stimulation causes a large inflammatory response

We next used the DEseq2 method to identify differential expression between vessels treated with TNFα vs untreated resting vessels that were perfused with normal RBCs at 8 and 24 hours post-perfusion (i.e. the 8 and 24 hours timepoints is equivalent to 27 and 43 hours after initial treatment with TNFα, respectively, Figure 5.4A schematic). At 8 hours post-RBC perfusion, the TNFα stimulated vessels had a large number of differentially expressed genes compared to resting baseline (N=2265 up and N=1807 down). Significant differentially expressed genes (fold change >1.5 and an adjusted p-value <.05) are shown as a volcano plot (Figure 5.5A). GO biological process pathway enrichment analysis of the 2265 upregulated genes selected multiple significant terms including immune regulation terms (e.g., neutrophil migration, leukocyte activation, and innate immune response), inflammatory pathways (e.g., TNF-mediated signaling pathway, cytokine-mediated signaling pathway, and NF-kappaB signaling pathways), and pathways related to protein targeting and translation. Although 8 hours post-perfusion is 27 hours after the initial treatment with TNFα, the effects are still strong. Within the TNFα-mediated signaling pathway, 42 genes are significantly upregulated in the TNFα treated vessels compared to resting baseline (Figure 5.5E).

Comparatively, by 24 hours post-perfusion (43 hours after the initial treatment with TNFα), the vessels have significantly recovered towards baseline. Far fewer genes are differentially expressed compared to resting baseline (N=119 up and N=171 down) (Figure 5.5B). GO biological process pathway enrichment analysis of the 119 significantly upregulated genes revealed fewer significant terms compared to the 8 hour timepoint (Figure 5.5D). The terms still enriched at the 24 hour timepoint include primarily immune

related terms such as innate immune response, antigen processing and presentation, and leukocyte activation. Additional new terms include negative regulation of innate immune response, negative regulation of cell activation, and negative regulation of immune system process. Unlike the 8 hour timepoint, there was no significant enrichment of terms related to protein targeting, translation, or mRNA catabolic processes. Together, this confirms that the initial immune response upregulation is waning and replaced by negative regulation of immune pathways. A comparison of all differentially expressed genes from both time points is shown as a venn diagram (Figure 5.5F) which highlights the regression towards baseline at the 24 hour timepoint.

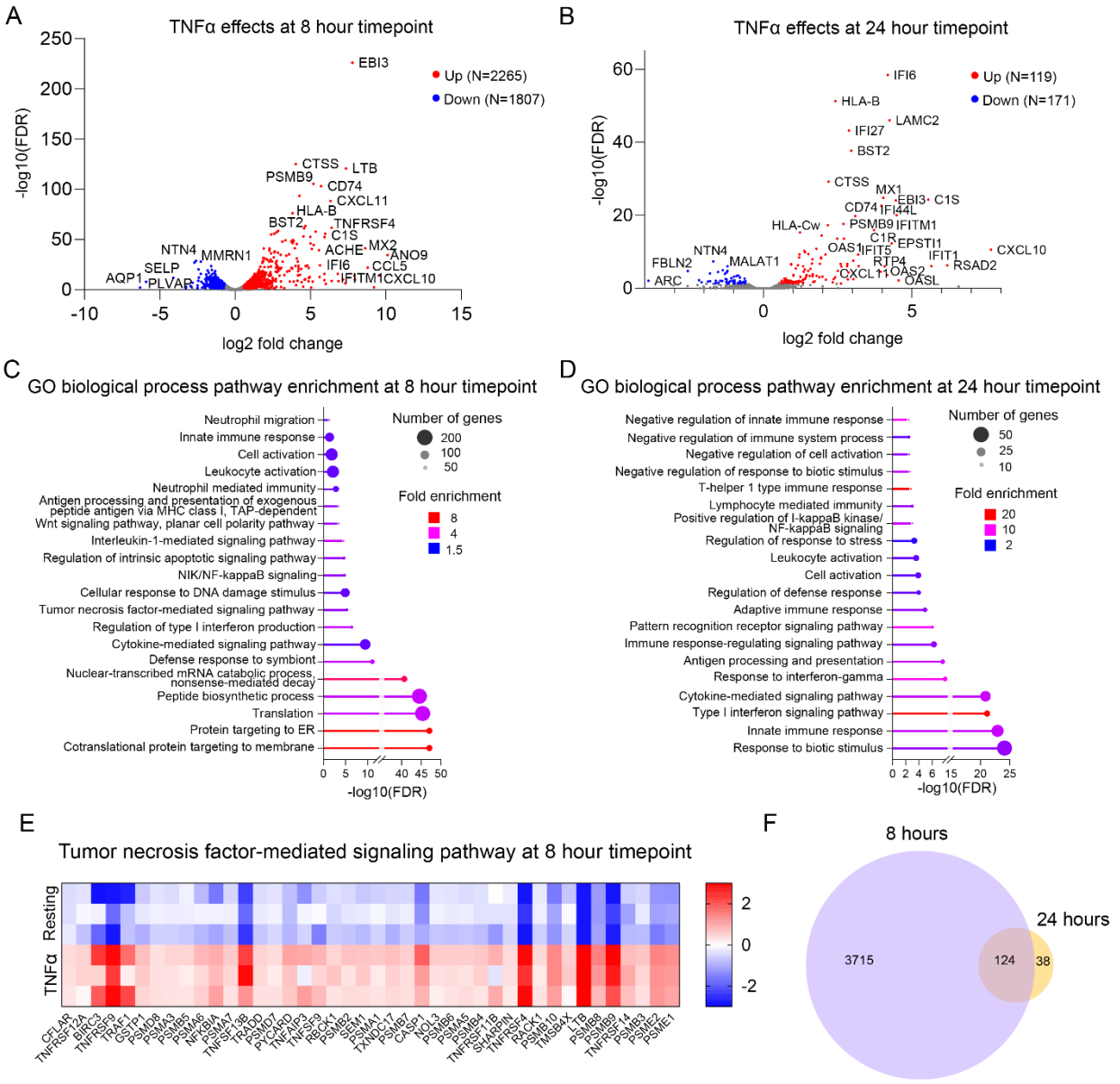

Figure 5.5: Stimulation of 3D brain microvessels by TNFα causes an inflammatory response which is still active 27 hours post-treatment but has regressed towards baseline by 43 hours.

(A): Volcano plot showing the comparison of TNFα treatment vs. resting baseline at 8-hour time point (equivalent to 27 hours post-TNFα treatment, see figure 4 experimental diagram). Significant differential gene expression is defined as a fold change > 1.5 and adjusted p-value <.05. **(B):** Volcano plot showing the comparison of TNFα treatment vs. resting baseline at 24 hours timepoint (equivalent to 43 hours post-TNFα treatment, see figure 4 experimental diagram). **(C):** Selected pathways from GO biological process pathway enrichment analysis of significant upregulated genes (N=2265) at 8 hours. **(D):** Selected pathways from GO biological pathway enrichment analysis of significant upregulated genes (N=119) at 24 hours. In addition to much fewer genes being upregulated, pathways involved in the negative regulation of immune response have been enriched. **(E):** Heatmap of 42 genes significantly upregulated within the tumor necrosis factor-mediated signaling pathway at 8 hours. **(F):** Venn diagram of differentially expressed genes at 8 hours and 24 hours. By 24 hours far fewer genes are differentially expressed.

5.2.6. P. falciparum iRBCs stimulate immune response, apoptosis, and metal ion hemostasis pathways

To next explore the effects of the *P. falciparum* iRBCs on the brain microvessels, we used the DEseq2 method to identify differential expression between vessels perfused with iRBCs compared to vessels perfused with normal RBCs at 8 and 24 hours in resting endothelium (Figure 5.4A schematic). At 8 hours post-perfusion, the iRBCs had a modest amount of differentially expressed genes compared to baseline (N=567 up and N=371 down). Significant differentially expressed genes (fold change > 1.5 and adjusted p-value < .05) are shown on a volcano plot (Figure 5.6A). GO biological process enrichment analysis of the 567 significantly upregulated genes revealed terms related to immune processes (e.g., cell activation involved in immune response, modulation by symbiont of host defense response), terms related to processing inorganic substances (e.g., detoxification of inorganic compound, transition metal ion homeostasis), as well as terms related to protein targeting, translation, viral transcription, and transport (Figure 5.6C). Many of these terms are in common or similar to terms enriched from treatment by TNFα, including protein targeting to ER, nuclear-transcribed mRNA catabolic process, and translation, as well as immune pathways such as leukocyte activation and neutrophil mediated immunity. The leukocyte activation involved in immune response term contains 31 significantly upregulated genes which are shown as a heatmap (Figure 5.6E, left). A comparison of the differentially expressed genes from TNFα stimulation and parasite stimulation are shown as a venn diagram (Figure 5.6F), highlighting that the majority of differentially expressed genes from parasite stimulation overlap with TNFα (792 differentially expressed genes in common, and 118 differentially expressed genes unique to parasite). No significant enrichment was found from the 118 unique to parasite genes,

but of note is the enrichment of the transition metal ion homeostasis term which was not enriched in the TNFα condition and contained 10 significantly upregulated genes (Figure 5.6E, right). This includes a set of metallothionein genes MT1G, MT2A, MT1E, and MT1X which are involved in cellular response to heavy metals and potentially have immune related functions or act as anti-oxidants, protect against hydroxyl free radicals, and play a role in detoxification of heavy metals.

At 24 hours, the total number of differentially expressed genes is similar to what was seen at 8 hours (N=531 up, N=285 down) (Figure 5.6B). GO biological process enrichment analysis of the 531 upregulated genes included numerous terms which were the same or similar to the 8 hour timepoint (Figure 5.6D). These include terms related to protein targeting, viral transcription, and nuclear-transcribed mRNA catabolic processes, as well as several immune related terms such as neutrophil activation involved in immune response and myeloid cell activation. 23 genes were significantly upregulated in the myeloid cell activation involved in immune response term and are shown as a heatmap (Figure 5.6G, left). Unique to the 24 hour timepoint is the enrichment of terms related to apoptosis including positive regulation of intrinsic apoptotic signaling pathway. The 14 genes significantly upregulated in the intrinsic apoptotic signaling pathway are shown as a heatmap (Figure 5.6G, right). The appearance of apoptotic signaling at 24 hours but not at 8 hours is in agreement with the appearance of apoptotic blebs visualized by SEM at 24 hours.

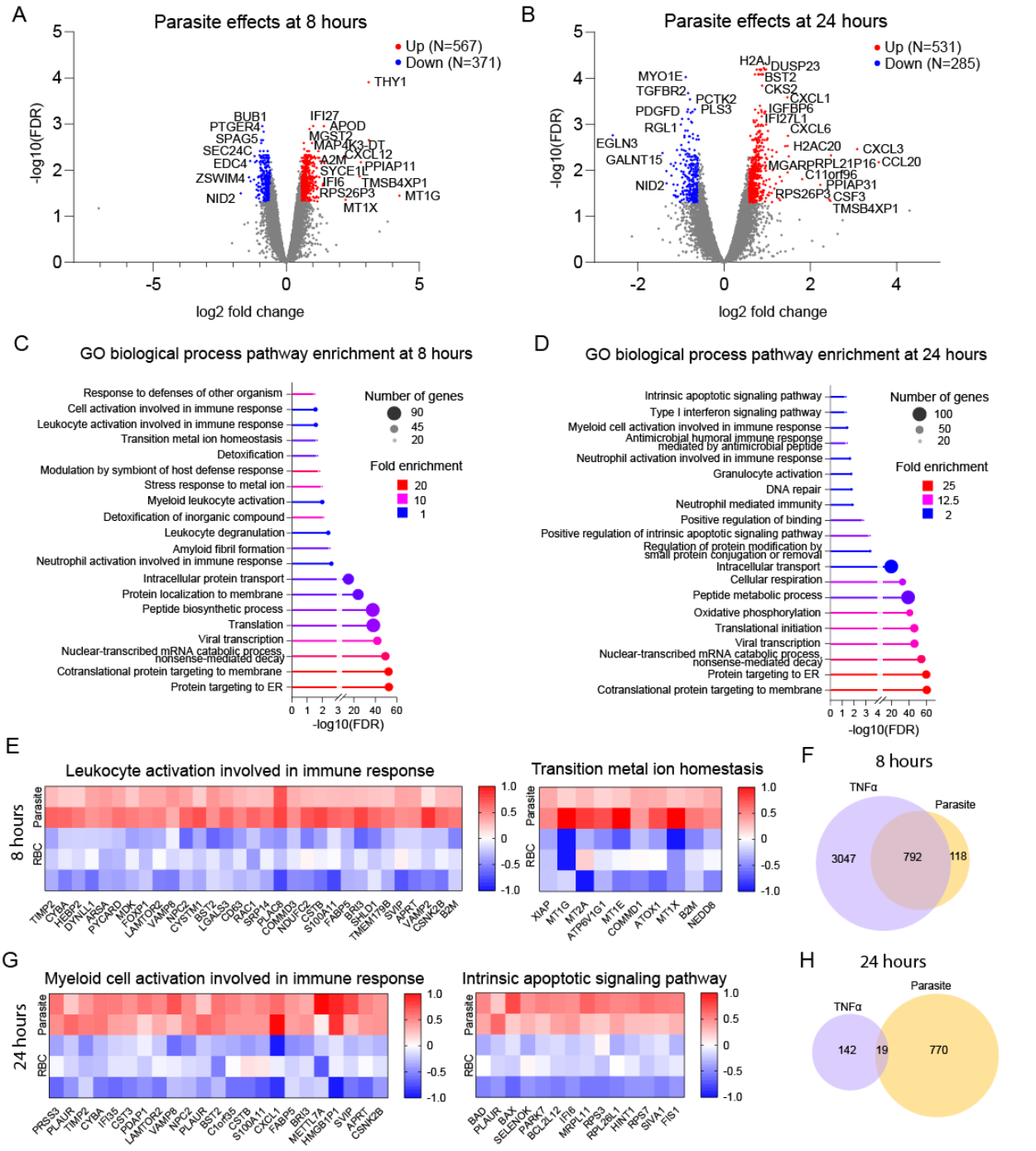

Figure 5.6: *P. falciparum*-iRBCs induce modest activation of endothelial cell pathways involved in immune response and upregulate pathways involved in metal ion detoxification and apoptosis as iRBCs mature in situ.

(A): Volcano plot showing the comparison of parasite vs RBC baseline 8 hours after perfusion. Significant differential gene expression is defined as a fold change > 1.5 and adjusted p-value <.05. **(B):** Volcano plot showing the comparison of parasite vs. RBC 24 hours after perfusion. **(C):** Selected pathways from GO biological process pathway enrichment analysis of significant upregulated genes (N=567) at 8 hours. **(D):**

Selected pathways from GO biological pathway enrichment analysis of significant upregulated genes (N=531) at 24 hours. **(E):** Heatmap of 31 genes significantly upregulated within the leukocyte activation involved in immune response pathway (left) and 10 genes significantly upregulated within the transition metal ion homestasis pathway (right) at 8 hours post perfusion. **(F):** Venn diagram of differentially expressed genes at 8 hours from TNFα (equivalent to 26 hours post TNFα treatment) or parasite stimulations. The majority of differentially expressed genes from parasite stimulation are shared with TNFα stimulation. **(G):** Heatmap of 23 genes significantly upregulated in the myeloid cell activation involved in immune response pathway (left) and 14 genes significantly upregulated in the intrinsic apoptotic signaling pathway (right) at 24 hours post perfusion. **(H):** Venn diagram of differentially expressed genes at 24-hour endpoint from TNFα (equivalent to 42 hours post TNFα treatment) or parasite stimulation. While vessels have recovered significantly from TNFα stimulation, the parasite stimulation has sustained and augmented the endothelial cell response.

5.2.7. P. falciparum iRBCs cause an augmented and enhanced effect on TNFα activated endothelium

Because *P. falciparum* cerebral malaria infection typically includes high systemic levels of TNFα, we next evaluated the effects of iRBC adherence in TNFα stimulated vessels. For this analysis, we compared transcriptional differences between vessels that were pre-stimulated for 18 hours with TNFα and then perfused with either iRBCs or normal RBCs at 8 and 24 hours post-perfusion. At 8 hours post-perfusion, the iRBC vessels had 469 significantly upregulated and 894 significantly downregulated genes compared to normal RBCs (Figure 5.7A). GO biological process enrichment analysis of the 469 upregulated genes showed enrichment of terms related to metabolism, transport, and protein import into nucleus, as well as regulation of toll-like receptor 3 and toll-like receptor 4 signaling pathways. Multiple terms related to apoptosis were enriched and the 26 genes significantly upregulated in the apoptotic signaling pathway are shown as a heatmap (Figure 5.7E).

At 24 hours post-perfusion, there were a substantial number of differentially expressed genes (N=2302 up and N=1976 down) (Figure 5.7B). GO biological process enrichment analysis of the 2302 upregulated genes revealed enrichment of terms related to immune regulation (e.g., activation of innate immune response and antigen processing,

presentation of exogenous peptide antigen via MHC class I), terms related to apoptosis such as intrinsic apoptotic signaling pathway, stress response to metal ions, and terms related to protein targeting, metabolism, and translation. This large number of differentially expressed genes and the enriched pathways suggest that the iRBCs are both inducing unique effects seen in the parasite only conditions (e.g., stress response to metal ions and apoptosis), as well as greatly preventing the waning of the TNFα stimulation effects towards baseline which was seen by 24 hours without iRBCs. The 53 significantly upregulated genes in the intrinsic apoptotic signaling pathway and the 7 genes significantly upregulated in the monocyte chemotactic protein-1 production pathway are shown as heatmaps (Figure 5.7G).

To visualize the relationships between TNFα effects, parasite effects, and parasite + TNFα effects, 3-way venn diagrams of all differentially expressed genes are shown for the 8 and 24 hour timepoints (Figure 5.7F). At 8 hours, TNFα stimulation alone resulted in the largest number of differentially expressed genes. From the TNFα + parasite condition, 757 differentially expressed genes are shared with the TNFα only condition, and 211 are unique. By 24 hours, the TNFα only stimulation has substantially regressed towards baseline with far fewer differentially expressed genes remaining. The TNFα + parasite condition has the largest number of differentially expressed genes from any other comparison, highlighting the combinatorial effects of TNF α and iRBCs both upregulating stress response pathways (metallothionines and apoptosis), as well as preventing the recovery of the endothelium from TNFα stimulation towards baseline.

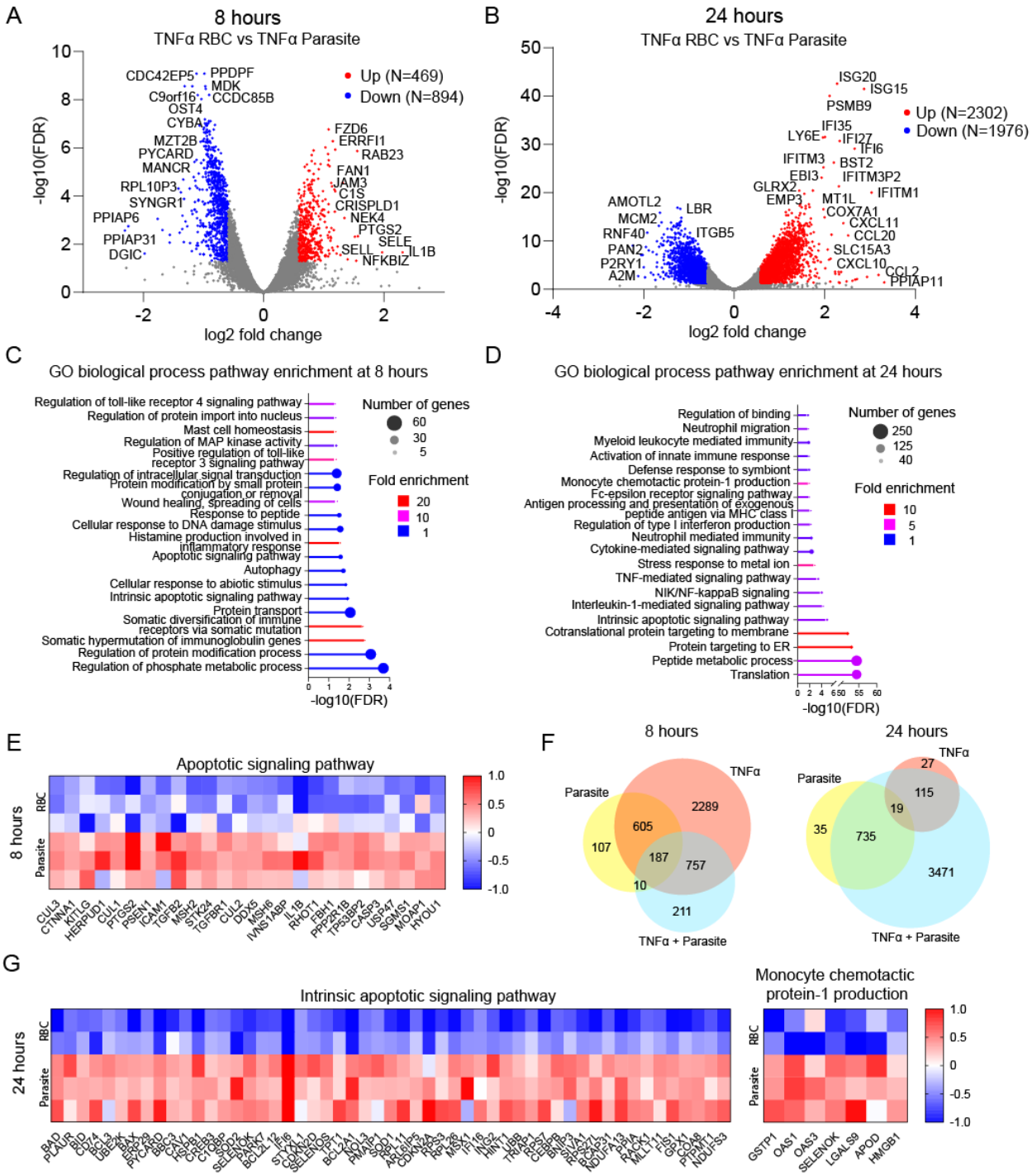

Figure 5.7: *P. falciparum*-iRBC binding in TNFα treated vessels enhances the inflammatory response at 8 hours and prevents the regression towards baseline by 24 hours.

(A): Volcano plot showing the comparison of parasite vs RBC baseline in TNFα pre-treated vessels 8 hours after iRBC perfusion. Significant differential gene expression is defined as a fold change > 1.5 and adjusted p-value <.05. **(B):** Volcano plot showing the comparison of parasite vs. RBC in TNFα pre-treated vessels 24 hours after iRBC perfusion. **(C):** Selected pathways from GO biological process pathway enrichment analysis of significant upregulated genes (N=469) at 8 hours. **(D):** Selected pathways from GO biological

pathway enrichment analysis of significant upregulated genes (N=2302) at 24 hours endpoint. **(E):** Heatmap of 26 genes significantly upregulated within the apoptotic signaling pathway at 8 hours post iRBC perfusion. **(F):** Venn diagrams of differentially expressed genes at 8 (left) and 24 (right) hours from stimulations of TNFα alone, *P. falciparum* IEs alone, and the combination of both. At 8 hours the majority of differentially expressed genes in the combined TNFα and parasite condition are shared with TNFα alone. By 24 hours, the number of differentially expressed genes in the combined TNFα and parasite condition has greatly increased. **(G):** Heatmap of 53 genes significantly upregulated in the intrinsic apoptotic signaling pathway (left) and 7 genes significantly upregulated in the monocyte chemotactic protein-1 production pathway (right) at 24 hours post iRBC perfusion.

5.2.8. P. falciparum iRBCs and TNFα stimulation induces leukocyte recruitment

We next evaluated whether TNFα and parasite treatments enhanced leukocyte recruitment within 3D brain microvessels. Staining for ICAM-1, a cell adhesion molecule involved in immune cell recruitment, showed that TNFα-stimulated vessels had broad and homogeneous increases in surface ICAM-1 expression compared to the resting baseline (Figure 5.8A). By contrast, the iRBC vessels exhibited a much weaker, sparse, and patchwork-pattern of ICAM-1 surface expression. Notably, not every endothelial cell which had a bound iRBC had a higher expression level of ICAM-1 as seen by fluorescent imaging. Staining for VE-cad, a junctional protein, revealed that TNFα treatment induced a global reduction in VE-cad expression as well as a loss of complete continuity around the borders of cells (Figure 5.8B). The iRBC vessels did not exhibit a notable overall decrease in VE-cad expression but did display some potential morphological changes with the VE-cad expression not remaining tightly expressed at the borders but occasionally appearing cytoplasmic or internalized.

To investigate whether TNFα treatment and sequestered iRBC modified leukocyte recruitment, 3D microvessels were perfused with peripheral blood mononuclear cells (PBMCs) that were isolated from whole blood and contained a mixed population of

monocytes, B cells, granulocytes, and T cells (Figure 5.8C). PBMCs were perfused through brain microvessels at the 8 hour timepoint post-iRBC treatment. Following perfusion, the vessels were stained for CD45, a pan leukocyte marker, and CD14, a monocyte marker, to determine the extent of and pattern of PBMC adhesion. In resting 3D brain microvessels, there was minimal adherence of CD45+ or CD14+ cells (Figure 5.8D). By comparison, with TNFα stimulation, there was a uniform increase in the number of adherent PBMCs and the pattern of binding was almost always uniformly scattered throughout all parts of the vessels. Strikingly, the iRBC-perfused vessels also displayed a substantial increase in the number of adherent PBMCs but the binding pattern was distinct from TNFα treated vessels. In vessels with adherent iRBCs, there were vessel regions with negligible amounts of adhered PBMCs and regions which had high concentrations of adhered PBMCs. The PBMCs also often adhered in large aggregates. By video microscopy, a few leukocytes bound at the start of the perfusion and more accumulated to specific areas over time suggesting a localized mechanism of leukocyte recruitment in the parasite vessels.

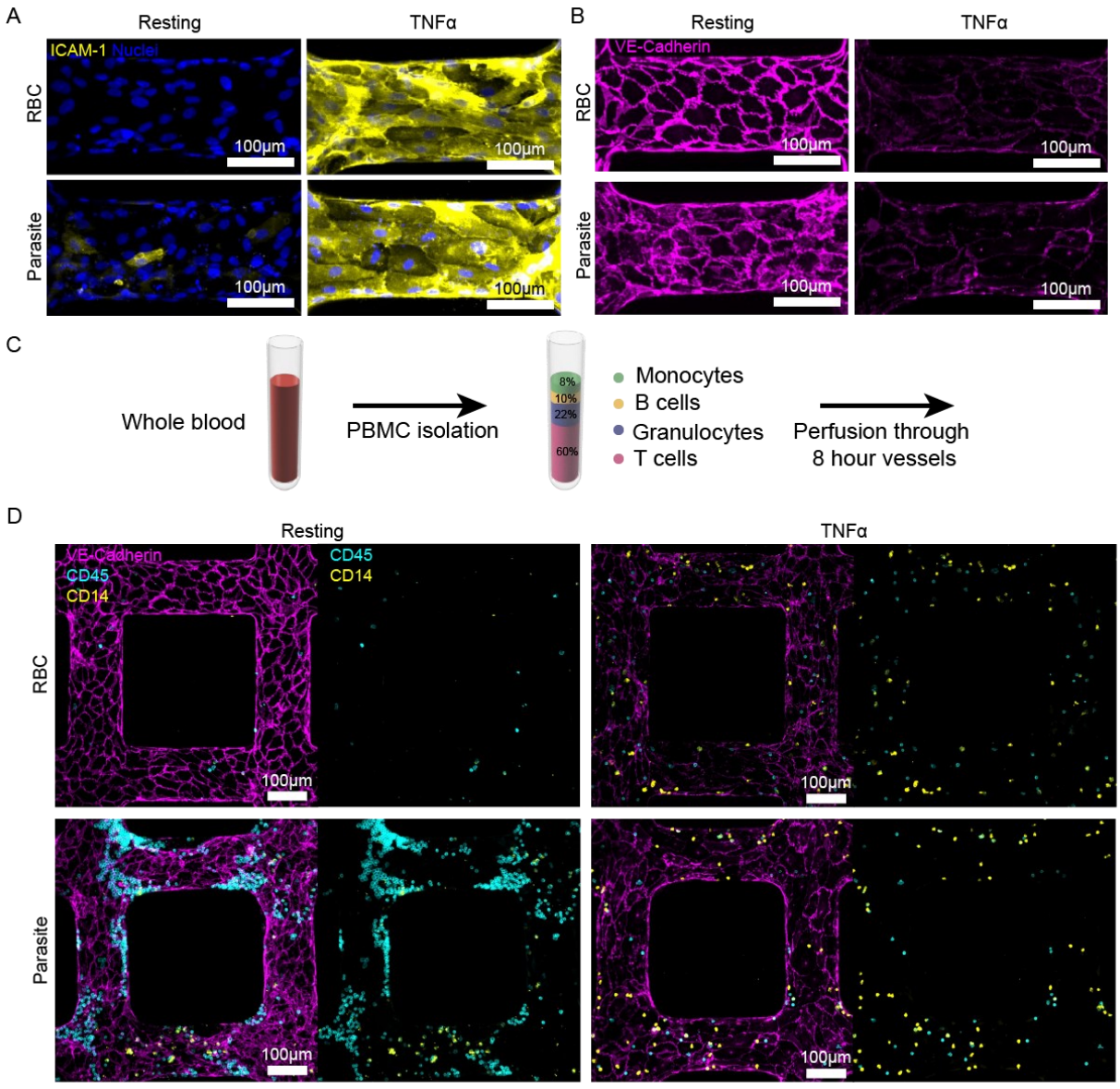

Figure 5.8: Stimulation by TNFα or *P. falciparum*-iRBCs causes distinct upregulation of surface ICAM-1 in brain endothelial cells and both treatments lead to recruitment of peripheral blood mononuclear cells (PBMCs).

(A): Representative images of ICAM-1 expression by immunofluorescence staining. TNFα stimulation leads to uniform high surface expression throughout the microvessels where iRBC stimulation results in a lower and heterogeneous expression. **(B):** Representative images of VE-Cadherin expression by immunofluorescence staining. Both TNFα and iRBC stimulation leads to lower overall surface expression as well as disrupted borders between cells. **(C):** Schematic showing overview of estimated cell populations from PBMC isolation from whole blood used to perfuse through vessels at 8 hours. **(D):** Representative images showing the binding patterns of CD14+ and CD45+ cells after perfusion. There is minimal binding of CD14+ or CD45+ cells to resting 3D brain microvessels. TNFα stimulation results in a uniform homogeneous binding of leukocytes where iRBCs cause heterogeneous clusters of leukocytes.

5.2.9. P. falciparum iRBCs induce a heterogeneous recruitment of leukocytes compared to TNFα stimulation

Because iRBCs were less potent than TNFα in upregulating surface ICAM-1, we studied the spatial relationship of iRBCs and leukocytes. For this analysis, x-y coordinates were determined for iRBCs, CD14+ only cells, and all CD45+ cells in the four conditions. Overall, all three experimental groups (TNFα stimulation, iRBC stimulation, and TNFα + iRBC stimulation) led to a significantly increased average number of adherent PBMCs compared to resting vessels with the combined TNFα + iRBC stimulation having the most followed by TNFα alone then iRBC alone (Figure 5.9A). Additionally, the ratio of CD14+::CD45+ cells was highest for the iRBC treatment, indicating that parasites may preferentially recruit monocytes compared to TNFα. We next mapped out the x-y location of each adhered CD14+ cell and plotted as a scatterplot, then divided these plots into vessel segments to display as a heatmap (Figure 5.9B). The resting RBC condition had uniform low binding throughout. With TNFα stimulation, there was a homogeneous increase in PBMC binding across most vessel regions, with a slight preference for regions in the first half of the vessel. With iRBCs, there was a heterogeneous increase in CD14+ cell binding with regions towards the corners and edges of the grid having higher rates of binding and regions towards the inlet, outlet, and center having lower rates of binding. By comparison, the combined TNFα + iRBC condition had higher levels of PBMC binding uniformly throughout the vessel. Similar trends were seen when analyzing the CD45+ bound cell locations (Figure 5.9D). Whereas TNFα stimulation led to a uniform increase in CD45+ bound cells throughout the entire vessel, iRBC stimulation led to a patchy, hetereogeneous distribution of CD45+ bound cells. The combination of TNFα and iRBC stimulation led to high levels of PBMC binding throughout the entire vessel.

To analyze the spatial relationship between PBMC and iRBC adherence, we mapped each bound iRBC on a scatterplot and divided the plot up into segments to show as a heatmap for iRBC binding in both resting and TNFα-stimulated vessels (Figure 5.9C). In resting vessels, the iRBC binding pattern has a similar trend to CD14+ bound cells with higher degrees of binding towards the corners and lower areas of binding towards the inlets and outlets. Likewise, regions which had CD45+ aggregates were usually directly near or sometimes surrounding the bound iRBCs (Figure 5.9E). While some iRBCs seemed to recruit aggregates of PBMCs, others did not. By plotting the average number of bound iRBCs against the number of bound leukocytes for each vessel segment (N=3 vessels), there is a difference in the distribution between conditions. For resting vessels, there is a positive shift along the iRBC axis, demonstrating there is a minimum number of iRBCs per vessel segment required to recruit leukocytes. For the TNFα-stimulated vessels and especially for CD45+ cells, there is a positive shift along the leukocyte axis, highlighting that there were adhered leukocytes throughout all vessel segments regardless of the number of iRBCs.

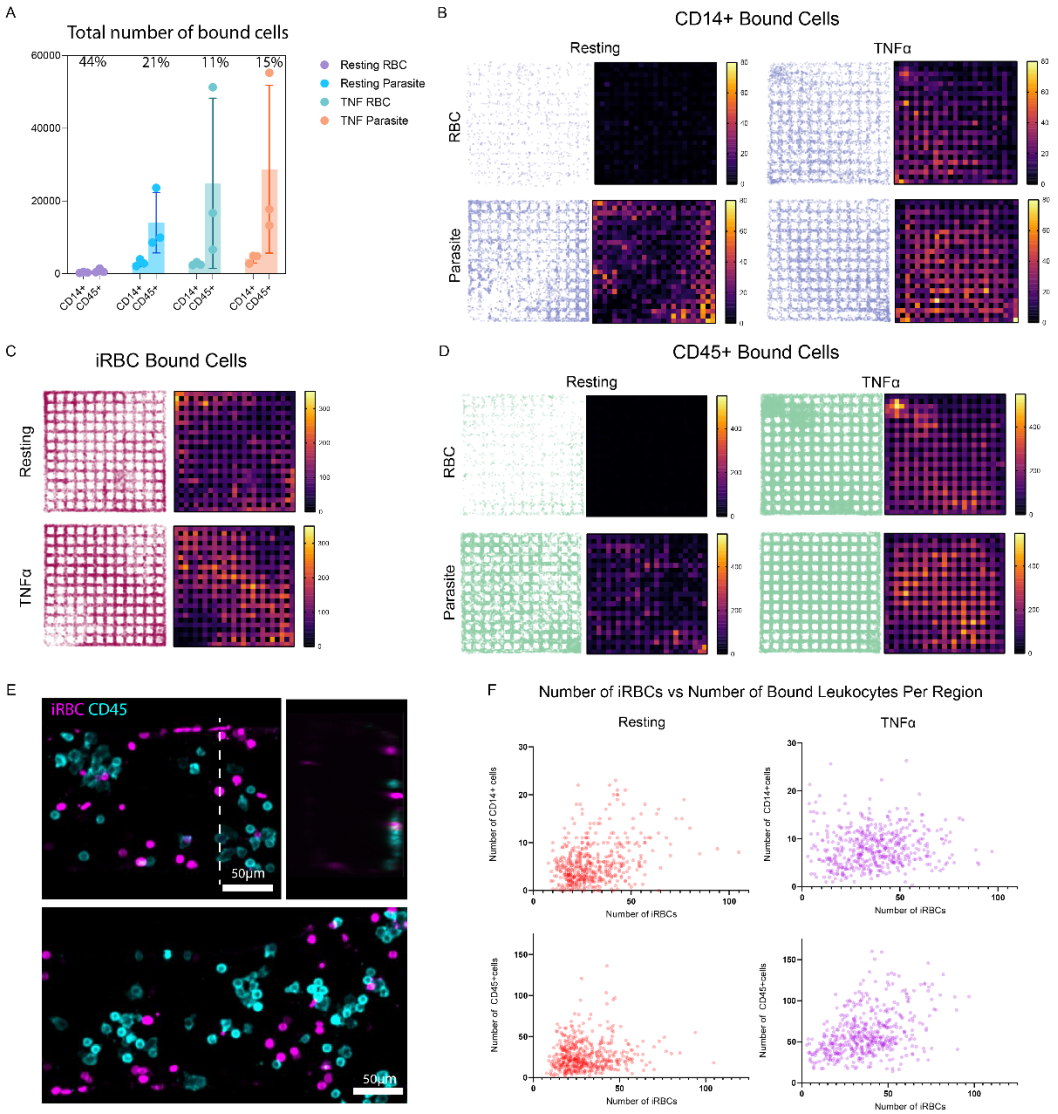

Figure 5.9: Leukocyte binding in vessels stimulated by *P. falciparum*-iRBCs is spatially heterogeneous compared to binding in vessels stimulated by TNFα.

(A): Graph showing the total number of bound CD14+ and CD45+ cells in each condition with N=3 replicates. Percentages are the percentage of CD14+ cells compared to total CD45+ cells in each condition. (B-D) Scatterplots and heatmaps showing the spatial distribution of different cell types across the 3D microvessels (n = 3), cell measurements were done in the same microvessels **(B):** Scatterplots and heatmaps showing the spatial distribution of CD14+ cells. Scatterplots are an overlay of 3 replicates with each point representing one bound CD14+ cell. Heatmaps are showing the sum of CD14+ bound cells in each vessel segment from 3 replicates. **(C):** Scatterplots and heatmaps showing the spatial distribution of adhered iRBCs in resting and TNFα-stimulated vessels from 3 replicates. **(D):** Scatterplots and heatmaps showing the spatial distribution of CD45+ cells from 3 replicates. **(E):** Representative images of the spatial relationship between adhered iRBCs and CD45+ cells. **(F):** Plots showing the average number of bound iRBCs vs the number of bound CD14+ or CD45+ cells per vessel region. Each dot represents the average of N=3 replicates at one vessel region.

5.3. DISCUSSION

Numerous host and parasite factors are implicated in cerebral malaria pathology, but the inaccessibility of the brain has hindered understanding of the molecular pathways of disease. In this study, we exploited an engineered 3D human brain microvessel model to investigate host and parasite factors implicated in cerebral malaria pathology under conditions that allowed the *in situ* maturation of adherent iRBCs. Our analysis indicates that thrombin, TNFα, and iRBCs are each stimulatory for brain endothelial cells but they induce different cellular phenotypes.

Severe brain swelling is the cause of death in pediatric cerebral malaria[123], but the molecular mechanisms leading to breakdown of the blood brain barrier remain incompletely understood. In terms of barrier integrity, thrombin was the most barrier-disruptive stimuli inducing large gaps and fissures between brain endothelial cells. Thrombin[287] and fibrin[278] deposits are prominent in fatal pediatric cerebral malaria cases and EPCR-binding parasites impair pathways that normally counteract thrombin signaling[125,151,229,284], which may lead to excessive thrombin signaling in the microvasculature. By comparison, TNFα and parasites induced small punctate holes either between the cell junctions or within the cell body which could be representative of early barrier disruption. TNFα and parasite stimuli also differed in their effect on the main adherens junction protein VE-cad with TNFα causing a substantial reduction of surface VE-cad and parasite stimuli only leading to subtle morphological changes in surface labeling. In the parasite vessels, punctate disruptions were sometimes near adhered iRBCs or adjacent to an endothelial apoptotic bleb. Notably, iRBCs were the only treatment that led to apoptotic blebs as well as the upregulation of apoptotic signaling

pathways by RNAseq analysis by 24 hours of culture. Similar to previous work from Tripathi et al.[285], parasite exposure also led to transcriptional upregulation of several metallothinein genes, a family of metal-binding proteins that functions in cellular defense against metal toxicity, oxidative damage, and free radicals. These findings indicate that endothelial cells may be responding to parasite exposure by upregulating pathways to counteract damaging parasite products or by undergoing apoptosis. Previous studies have indicated that iRBCs can trigger apoptosis in endothelial cells in vitro[288]. Moreover, CM parasite isolates which can induce apoptosis correlate with neurological symptoms[289–291] and apoptotic pathways are upregulated in brain endothelial cells in fatal CM cases[291]. Collectively, these findings suggest that both the direct triggering of apoptosis in endothelial cells by iRBCs and thrombin-induced barrier disruption may be important contributors to blood-brain barrier breakdown in cerebral malaria.

Systemic endothelial activation occurs in both mild and severe malaria cases[129]. However, the precise mechanisms leading to monocyte recruitment in cerebral microvessels remain unclear. Although it has been reported that iRBCs can induce ICAM-1 on brain endothelial cells[130,278,292], our analysis suggests they are much less potent than TNFα. Nevertheless, we observed upregulation of cell surface changes, pro-inflammatory pathways, and CD14+ and CD45+ cellular recruitment in both TNFα and iRBC treated microvessels. Both TNFα and iRBCs led to the endothelial cell surface display of microparticles, a type of extracellular vesicle produced by activated cells which can act as effectors of coagulation, inflammation, and immune response[293]. In a clinical study of *P. falciparum* malaria, the number of endothelial microparticles circulating in the blood was increased in patients with severe disease[294]. Because iRBCs alone were enough to

induce microparticle formation within 8 hours of culture, these may be an important contributor to CM progression. Analysis of whole vessel transcriptomic signatures highlighted an upregulation of inflammatory and innate immune pathways in TNFα treated vessels at 27 hours that had largely subsided by 43 hours. Transcriptional evaluation of TNFα stimulation showed an upregulation of protein transport, protein targeting, translation, cell activation, immune cell processes, NF-kappaB signaling, and apoptotic signaling, all of which agree with previous findings[295–297]. By contrast, the iRBCs induced a more modest upregulation of inflammatory and innate immune pathways. In a study with HUVECs, no induction of apoptotic pathways or changes in transcription were found by iRBCs alone. However, in that study, the iRBCs did not appear to mature or rupture over 20 hours of culture[298]. In a study done with HBMECs, monolayers of HBMECs covered with iRBCs at a 50:1 ratio and cultured for 6 hours revealed enrichment of many similar pathways as seen in our study including immune response, apoptosis, and metal ion homeostasis[285]. Notably different, in our study we did not observe a widespread induction of ICAM-1 transcriptionally or by immunofluorescent staining in parasite-only vessels. One potential reason for this could be that the ratio of iRBCs used in our study was lower, and previous work has described an iRBC dose-dependent stimulation of ICAM-1[130]. Here we studied parasite effects at binding levels similar to cerebral malaria brain autopsy specimens[120], but we did not observe a strong correlation between number of adhered iRBCs and ICAM-1 expression spatially throughout the vessel. Because of this, it is unclear what factors directly cause the upregulation of ICAM-1 seen spatially by immunofluorescence on some but not all endothelial cells.

Despite the lack of a global induction of ICAM-1 by iRBCs, there was still a strong functional change observed in the ability of the endothelial cells to recruit leukocytes. Vessels treated with either TNFα or iRBCs recruited similar total number of CD14+ cells, and parasite-treated vessels had higher proportions of CD14+::CD45+ cells. This indicates that on a global level, iRBCs are causing an increase in leukocyte recruitment with a preference for monocytes as compared to TNFα stimulation. In patient autopsies from children with CM, accumulations of intravascular monocytes are significantly higher than from children with non-malarial coma, indicating the possible importance of monocytes in disease progression[179]. In addition to the difference in immune cell ratio, the spatial distribution of adhered leukocytes was also different between iRBCs and TNFα. TNFα stimulation caused a homogeneous scattered distribution of leukocytes where iRBCs led to a heterogeneous recruitment of leukocytes with regions of the vessel having no bound leukocytes and regions with large aggregates. This difference in distribution as well as the lack of global ICAM-1 surface expression in the iRBC vessels implies there are possibly different methods of recruitment between the treatments. Given the high levels of iRBC induced apoptosis, it is possible that monocytes and other phagocytic cells may be recruited for clearance of apoptotic endothelial cells[299].

The combination of TNFα and iRBCs enhanced many of the endothelial cell responses seen from either treatment alone. This was seen transcriptionally with the enrichment of NF-kappaB signaling, a pathway previously implicated in CM progression[291]. The combined stimuli also showed enrichment of apoptotic pathways by 8 hours, which wasn't seen by iRBCs alone until 24 hours, indicating that the combined parasite and TNFα stimuli may accelerate apoptotic signaling in endothelial cells. The combination also led

to the highest numbers of leukocyte recruitment compared to either treatment alone, again implying that the two stimuli are potentially causing different methods of recruitment. While the vessels with TNFα stimulation alone had a significant recovery transcriptionally by 43 hours after the initial treatment, the addition of iRBCs into TNFα-stimulated vessels prevented this recovery to baseline. Moreover, the combination of iRBCs and TNFα at the 24 hour timepoint (43 hrs post-TNFα) had the highest number of differentially expressed genes compared to baseline of any of the comparisons, highlighting the combinatorial contributions of iRBCs and host cytokine TNFα in causing sustained endothelial activation, inflammation, and immune response.

A limitation of this study was the use of bulk RNA-seq profiling which may have diluted out more localized transcriptional changes caused by iRBCs. Nevertheless, unique iRBC-induced apoptotic pathways were observed by imaging and by transcriptional profiling. Because parasite-induced alterations in endothelial cell phenotype were heterogeneous (e.g., surface microparticles, endothelial filaments, and surface ICAM-1) it suggests there are likely dose-dependent effects within a defined spatial radius and future work including spatial transcriptomics may provide a better understanding of the changes happening in proximity to sequestered iRBCs. Additionally, the mechanisms by which endothelial cells stimulated with iRBCs can recruit leukocytes is still unclear as the adhesion molecules usually implicated in leukocyte binding ICAM-1 and VCAM-1 were not significantly upregulated. To provide further insight into this, an antibody-blockade of adhesion molecules on endothelial cells or annexin V labeling can be performed to dissect the role of cell adhesion molecules versus apoptotic signaling in parasite leukocyte recruitment.

In conclusion, we demonstrate this 3D brain microvessel model has the potential for studying leukocyte recruitment and the evolution of endothelial phenotypes when exposed to diverse proinflammatory stimuli. Our work opens up future studies involving the perfusion of other blood components such as platelets to probe coagulation effects, or with longer co-culture periods with immune cells to investigate phagocytic clearance of apoptotic endothelial cells and cross-talk between endothelial cells and various blood immune cells. Additionally, because the TNFα stimulated vessels showed recovery towards baseline at the 24 hour timepoint, future work can be done to investigate drug targets and if protecting specific pathways can prevent the progression to endothelial cell dysfunction. Overall, these findings provide new mechanistic insights into vascular dysfunction in cerebral malaria and have implications for hyper-inflammatory processes involving the blood-brain barrier.

5.4. MATERIALS AND METHODS

5.4.1. Human brain microvascular endothelial cell culture

Primary HBMEC (Cell Systems, ACBRI 376) were cultured in EGM-2 Basal Medium (CC-3156) supplemented with EGM-2MV Microvascular Endothelial Cell Growth Medium SingleQuots (Lonza, CC-4147). Cells were grown as a monolayer until seeded in microvessels up to passage 6.

5.4.2. Microvessel fabrication

Microvessels were fabricated using soft lithography methods as previously described[300]. Type I collagen was isolated from rat tails, lyophilized, and resuspended to a concentration of 15 mg/mL in 0.1% acetic acid. This solution was then diluted to 7.5 mg/mL before being used. A polydimethylsiloxane (PDMS) stamp with a positive channel

network is used to pattern the vessel network into collagen which is injected through an acrylic piece with reservoirs for inlets and outlets. Stainless steel dowel pins were placed into the inlets and outlets to maintain open channels before injecting with collagen. A flat PDMS stamp is used to create a flat layer of collagen on a bottom acrylic piece which has an open space covered by a 22- by 22-mm coverslip. The collagen was incubated at 37 °C for 30 minutes until gelled and the PDMS stamps were removed. The top collagen layer is placed on the bottom layer and the acrylic pieces screwed together forming a seal. EGM-2MV media was then added to the channels and incubated for 1 hour prior to HBMEC seeding. HBMECs were isolated at a concentration of 7 x 10^6 cells/mL and 10 µL of solution was perfused through the inlet. After 1 hour of incubation, fresh medium was added to the inlet and microvessels were fed every 12 hours by gravity-driven flow. Microvessels were cultured for 1 day before adding an additional 5% human serum to the media. Microvessels were cultured with this additional human serum for 3-5 days before use in perfusion studies.

5.4.3. Parasite binding and co-culture

P. falciparum parasites were cultured using human erythrocytes in RPMI 1640 medium (GIBCO) supplemented with 10% human serum and grown in a gas mixture of 90% N_2, 5% CO2, and 1% O_2. Mid trophozoite-stage iRBCs (~ 25-33 hpi) were enriched by a MACS cell separator (LD columns, Miltenyi Biotec) and diluted to a concentration 5 x 10^6 in HBMEC media supplemented with an additional 5% human serum. 200 µL of this solution was added to the inlets of the microvessels and allowed to perfuse by gravity driven flow for 1 hour. After 1 hour, the effluent was removed from the outlet and fresh

media was added to the inlet to remove unbound iRBCs. The microvessels were fed by gravity driven perfusion every 12 hours.

5.4.4. Immunofluorescence microscopy

Microvessels were fixed *in situ* in 3.7% paraformaldehyde (PFA) and washed twice with Dulbecco's phosphate buffered saline (DPBS). They were then incubated in a blocking buffer with 2% bovine serum albumin and 0.1% Triton-X in DPBS for 1 hour. Blocked microvessels were incubated overnight in primary antibodies diluted in blocking buffer: 1:100 anti-human ICAM-1 (R&D Systems, BBA3), 1:100 APC conjugated anti-human VE-Cadherin (eBioscience, 17-1449-42), 1:100 Alexa Fluor 488 conjugated anti-human CD14 (eBioscience, 61D3), 1:100 PE conjugated anti-human CD45 (BioLegend, 304008). Microvessels were then washed twice with PBS prior to incubation with secondary antibodies for 1 hour: 1:100 Alexa Fluor 488 Goat Anti-Rabbit (Life Technologies, A-11008), 1:200 Hoechst 33342 (Thermo Fisher, H1399). Microvessels were then washed three times in PBS for 20 minutes each. Vessels were imaged using a Nikon Ti2 microscope or a Nikon Widefield microscope equipped with a Yokogawa W1 spinning disk head. Images were acquired with a 1-3 μm z-step distance between optical slices and cross-sections and projections were produced from z-stacks using Fiji (ImageJ) or Imaris (v9.1.3) software.

5.4.5. Scanning electron microscopy

Microvessels were fixed in ½ strength Karnovsky's fixative (2.5% glutaraldehyde, 2% PFA in 0.1M sodium cacodylate buffer) overnight at 4 °C. The collagen slabs were then removed from the acrylic housing and floated in ½ strength Karnovsky's fixative. For samples with top down imaging, the bottom collagen layer was peeled off leaving open

channels. Vessels were then rinsed with 0.1M cacodylate buffer and dehydrated through a graded series of alcohols and critical point dried using a Autosamdri-815 (Tousimis Corp). Then, vessels were mounted on stubs and sputter coated with gold/palladium using a Denton Desk IV (Denton Vacuum). Samples were imaged on a JSM 6610 LV scanning electron microscope at 5kV (JEOL).

5.4.6. RNA isolation, sequencing, and analysis

RNA from microvessels was collected and processed using an RNAeasy Micro Kit (Qiagen). RNA quality was assessed with an Aligent High Sensitivity RNA ScreenTap System. RNAsamples were prepared using an XT DNA Library Prep Kit (Nextera XT) and a SMART-Seq v4 Ultra Low Input RNA Kit (SMARTv4), a poly-A selection kit using an oligo dTprimer. RNA sequencing was performed on an Illumina NovaSeq 6000 SP with paired-end reads. RNAseq data was analyzed using iDEP.95 (integrated, Differential Expression and Pathway analysis, Bioinformatics Research Group, South Dakota State University). Samples were aligned to the hg38 human genome assembly and genes with > 4 reads per million were kept. DEseq2 was used for differential expression analysis with genes having fold change > 1.5 and FDR < 0.05 considered differentially expressed. ShinyGO v0.75 (Gene Ontology Enrichment Analysis, Bioinformatics Research Group, South Dakota State University) was used for GO term analysis of upregulated genes from pairwise comparisons.

5.4.7. PBMC isolation and perfusion

Whole blood was collected in BD Vacutainer blood collection tubes with sodium citrate (Fisher Scientific) on the day of perfusion experiments (3-8 hours in advance of perfusion). One hour in advance of perfusion, PBMCs were isolated from the whole blood

by density centrifugation in Lymphoprep solution (StemCell Technologies) in SepMate density gradient tubes (StemCell Technologies). Whole blood was layered on top of the Lymphoprep solution and centrifuged at 1,200 x g for 10 minutes. The top layer containing plasma and PBMCs was poured into a new tube and mixed with up to 50 mL of PBS. This solution was centrifuged at 250 x g for 10 minutes, the supernatant was aspirated, and the remaining cells were resuspended in 15 mL of PBS. This wash step was repeated and the washed PBMCs were resuspended in HBMEC media at a concentration of 1 x 10^7 cells/mL. 200 µL of the PBMC solution was perfused through the inlet of each vessel and allowed to flow for 1 hour. At one hour, the effluent was collected from the outlet and fresh media was perfused through the inlet to remove any unbound cells. Vessels were then fixed in 3.7% PFA.

5.4.8. Binding quantification and analysis

Images of entire vessels stained with CD14 and CD45 were used for the PBMC binding quantification. For iRBC binding quantification, light microscope images of entire vessels taken after the vessels were rinsed at 1 hour following iRBC perfusion were used. ImageJ was used to crop, orient, and align all vessel images and to mark the x-y location of each bound cell. Coordinates of each bound cell were then used for creating scatterplots. For heatmaps, the coordinates of bound cells along branches in each vessel image were used to determine histogram bin sizes. The list of coordinates and defined histogram bin sizes were then used with the Hist3 function in Matlab to create a 25 x 25 3D histogram. Scatterplots and heatmaps were created using the raw coordinates and the 3D histogram using GraphPad Prism.

Chapter 6. CONCLUSIONS AND FUTURE DIRECTIONS

Vacsulature is critical for delivering adequate nutrients to tissues, maintaining homeostasis, and for facilitating proper immune responses. Dysfunctional microvasculature is a characteristic of many pathologies and is challenging to study *in vivo* due to its small size, the inaccessibility of organs, and the dynamic nature of its functions. To overcome this obstacle, there is a need to develop better *in vitro* models of vascular systems which accurately recapitulate vessel geometries and the dynamic interactions between endothelial cells and blood components. The above work has established models and methods for generating organ-specific 3D microvasculature with controllable geometry down to the micron scale, mimicking the smallest blood vessels in the body, and the applications of these models for studying cerebral malaria. In Chapter 3, a combination of soft lithography and 2-photon laser ablation was used to create endothelialized channels in collagen hydrogels down to 5 micron in diameter, the size of capillaries. These capillaries were then used to study binding dynamics of *P. falciparum* infected red blood cells, elucidating differences in cytoadherence from different phenotypes of parasites. This study dissected the separate contributions of parasite cytoadhesion and red cell deformability to the sequestration of *P. falciparum*-iRBCs in a microvessel device that mimicked the arteriole-capillary-venule transition. In Chapter 4, the ablation methods were expanded upon and optimized to include different extracellular matrices, diverse endothelial cell types (lung, kidney, brain), and complex 3D geometries mimicking the native organ's microvasculature. As a proof of concept, a 3D glomerulus model structure was patterned and endothelialized at anatomic scale and perfused with red blood cells, demonstrating a potential future direction in using complex models in

blood perfusion studies. ability to make organ-specific microvasculature for lung, kidney, and brain opens up new avenues for disease modeling. In Chapter 5, we used a 3D brain microvessel model to dissect the role of host and parasite factors in cerebral malaria pathology. This study highlighted important distinctions between the response of brain endothelial cells to thrombin, TNFα, and *P. falciparum* infected red blood cells. Together, this work can be used to facilitate better *in vitro* models of vascular dysfunction, and to better understand the molecular mechanisms leading to vascular breakdown in cerebral malaria.

The organ microvasculature exhibits enormous heterogeneity that is critical for specialized functions. This work has had two major focuses: vascular engineering methods and understanding cerebral malaria pathophysiology. Because of this, further advances can be made both in the engineering technologies and in the biological applications. In terms of engineering, we have demonstrated proof-of-concepts for various degrees of increasing complexities in vascular models. While we have made advances in the geometric designs, many of these designs were created using HUVECs only. We have shown compatibility of the ablation methods with different endothelial cell types as well as various bulk stromal cells, so future work should include using organ-specific endothelial cell types and appropriate stromal cells to create more biologically relevant tissues. As an example, optimizing the glomerulus model to be compatible with glomerular endothelial cells as well as podocytes would pave the way for developing a functional filtration assay. Additionally, these methods can be used in other areas of tissue engineering. As vascularization is a critical component in creating thick engineered

tissues and for maintaining viability in large organoids, the ability to create controllable small scale vascular systems could be advantageous in these areas.

In regards to understanding the pathophysiology of cerebral malaria, our work in probing the endothelial cell host response to iRBCs has revealed some directions which should be further explored. In the brain microvessel system, the endothelial cells had a more localized response to iRBC binding, as shown by surface expression of microparticles and ICAM-1 and the ability of the cells to recruit leukocytes. Because of the spatial heterogeneity of parasite binding, performing single cell RNA-seq or spatial transcriptomics analysis would allow for a better understanding of what is happening in regions with higher or lower adherent iRBCs. Additionally, the induction of apoptosis by iRBCs should be further explored to verify if apoptotic signaling has a role in the functional recruitment of leukocytes. The controllable perfusion of this model also lends itself well to perfusing blood components and whole blood could be used in addition to the isolated leukocytes to investigate changes in coagulation. Most of these studies have used just endothelial cells in the vascular models. Increasing the complexity of the model to include perivascular cells such as astrocytes and pericytes will also be an important next step in creating a more realistic blood brain barrier model. Because these cells are critical in maintain vascular barrier function, they are likely important factors to include in investigating vascular breakdown in cerebral malaria.

Altogether this work has established methods and models for creating engineered vascular systems suitable for addressing biological questions. Continued improvements in these methods for creating more physiologically relevant models will allow for a wider range of biological questions to be addressed. This will be particularly advantageous for

understanding the pathophysiology of cerebral malaria which has been long been a challenge to study.

REFERENCES

1. Mandrycky, C. J., Howard, C. C., Rayner, S. G., Shin, Y. J. & Zheng, Y. Organ-on-a-chip systems for vascular biology. *J. Mol. Cell. Cardiol.* **159**, 1–13 (2021).

2. Burggren, W. W. Cardiovascular Development and Angiogenesis in the Early Vertebrate Embryo. *Cardiovasc. Eng. Technol.* **4**, 234–245 (2013).

3. Patel-Hett, S. & D'Amore, P. A. Signal transduction in vasculogenesis and developmental angiogenesis. *Int. J. Dev. Biol.* **55**, 353–369 (2011).

4. J, H., C, P. & M, M. Life is a pattern: vascular assembly within the embryo. *Front. Biosci. (Elite Ed).* **4**, 2269 (2012).

5. Culver, J. C. & Dickinson, M. E. The effects of hemodynamic force on embryonic development. *Microcirculation* **17**, 164–178 (2010).

6. Han, Y., Huang, K., Yao, Q. P. & Jiang, Z. L. Mechanobiology in vascular remodeling. *Natl. Sci. Rev.* **5**, 933–946 (2018).

7. Carmeliet, P. & Jain, R. K. Molecular mechanisms and clinical applications of angiogenesis. *Nature* **473**, 298–307 (2011).

8. Rafii, S., Butler, J. M. & Ding, B. Sen. Angiocrine functions of organ-specific endothelial cells. *Nature* **529**, 316–325 (2016).

9. Betz, C., Lenard, A., Belting, H. G. & Affolter, M. Cell behaviors and dynamics during angiogenesis. *Dev.* **143**, 2249–2260 (2016).

10. Cleaver, O. & Melton, D. A. Endothelial signaling during development. *Nat. Med.* **9**, 661–668 (2003).

11. Zhang, B., Korolj, A., Lai, B. F. L. & Radisic, M. Advances in organ-on-a-chip engineering. *Nat. Rev. Mater.* **3**, 257–278 (2018).

12. Haddrick, M. & Simpson, P. B. Organ-on-a-chip technology: turning its potential for clinical benefit into reality. *Drug Discov. Today* **24**, 1217–1223 (2019).

13. Lin, D. S. Y., Guo, F. & Zhang, B. Modeling organ-specific vasculature with organ-on-a-chip devices. *Nanotechnology* **30**, (2019).

14. Lorthois, S., Lauwers, F. & Cassot, F. Tortuosity and other vessel attributes for arterioles and venules of the human cerebral cortex. *Microvasc. Res.* **91**, 99–109 (2014).

15. Jambusaria, A. *et al.* Endothelial heterogeneity across distinct vascular beds during homeostasis and inflammation. *Elife* **9**, (2020).

16. Marcu, R. *et al.* Human Organ-Specific Endothelial Cell Heterogeneity. *iScience* **4**, 20–35 (2018).

17. Cleuren, A. C. A. *et al.* The in vivo endothelial cell translatome is highly heterogeneous across vascular beds. *Proc. Natl. Acad. Sci. U. S. A.* **116**, 23618–23624 (2019).

18. Aird, W. C. Endothelial cell heterogeneity. *Cold Spring Harb. Perspect. Med.* **2**, (2012).

19. Aird, W. C. Phenotypic heterogeneity of the endothelium: I. Structure, function, and mechanisms. *Circ. Res.* **100**, 158–173 (2007).

20. Poisson, J. *et al.* Liver sinusoidal endothelial cells: Physiology and role in liver diseases. *J. Hepatol.* **66**, 212–227 (2017).

21. Kopp, H. G., Avecilla, S. T., Hooper, A. T. & Rafii, S. The bone marrow vascular niche: Home of HSC differentiation and mobilization. *Physiology* **20**, 349–356 (2005).

22. Inra, C. N. *et al.* A perisinusoidal niche for extramedullary haematopoiesis in the spleen. *Nature* **527**, 466–471 (2015).

23. Alabi, R. O., Farber, G. & Blobel, C. P. Intriguing roles for endothelial ADAM10/ notch signaling in the development of organ-specific vascular beds. *Physiol. Rev.* **98**, 2025–2061 (2018).

24. Chiu, J. J., Wang, D. L., Usami, S., Chien, S. & Skalak, R. Effects of disturbed flow on endothelial cells. *J. Biomech. Eng.* **120**, 2–8 (1998).

25. Chien, S. Mechanotransduction and endothelial cell homeostasis: The wisdom of the cell. in *American Journal of Physiology - Heart and Circulatory Physiology* vol. 292 (Am J Physiol Heart Circ Physiol, 2007).

26. Chen, Z. & Tzima, E. PECAM-1 is necessary for flow-induced vascular remodeling. *Arterioscler. Thromb. Vasc. Biol.* **29**, 1067–1073 (2009).

27. Tzima, E. *et al.* A mechanosensory complex that mediates the endothelial cell

response to fluid shear stress. *Nature* **437**, 426–431 (2005).

28. Coon, B. G. *et al.* Intramembrane binding of VE-cadherin to VEGFR2 and VEGFR3 assembles the endothelial mechanosensory complex. *J. Cell Biol.* **208**, 975–986 (2015).

29. Conway, D. E. *et al.* VE-Cadherin Phosphorylation Regulates Endothelial Fluid Shear Stress Responses through the Polarity Protein LGN. *Curr. Biol.* **27**, 2219-2225.e5 (2017).

30. Hahn, C. & Schwartz, M. A. Mechanotransduction in vascular physiology and atherogenesis. *Nature Reviews Molecular Cell Biology* vol. 10 53–62 (2009).

31. Baeyens, N. & Schwartz, M. A. Biomechanics of vascular mechanosensation and remodeling. *Mol. Biol. Cell* **27**, 7–11 (2016).

32. Pries, A. R., Neuhaus, D. & Gaehtgens, P. Blood viscosity in tube flow: Dependence on diameter and hematocrit. *Am. J. Physiol. - Hear. Circ. Physiol.* **263**, (1992).

33. Coste, B. *et al.* Piezo1 and Piezo2 are essential components of distinct mechanically activated cation channels. *Science (80-.).* **330**, 55–60 (2010).

34. Dumont, O., Loufrani, L. & Henrion, D. Key role of the NO-pathway and matrix metalloprotease-9 in high blood flow-induced remodeling of rat resistance arteries. *Arterioscler. Thromb. Vasc. Biol.* **27**, 317–324 (2007).

35. Min, E. & Schwartz, M. A. Translocating transcription factors in fluid shear stress-

mediated vascular remodeling and disease. *Experimental Cell Research* vol. 376 92–97 (2019).

36. Dimmeler, S. *et al.* Activation of nitric oxide synthase in endothelial cells by Akt-dependent phosphorylation. *Nature* **399**, 601–605 (1999).

37. Tarbell, J. M. Shear stress and the endothelial transport barrier. *Cardiovasc. Res.* **87**, 320–330 (2010).

38. Baeyens, N., Bandyopadhyay, C., Coon, B. G., Yun, S. & Schwartz, M. A. Endothelial fluid shear stress sensing in vascular health and disease. *J. Clin. Invest.* **126**, 821–828 (2016).

39. Conway, D. E. *et al.* Fluid shear stress on endothelial cells modulates mechanical tension across VE-cadherin and PECAM-1. *Curr. Biol.* **23**, 1024–1030 (2013).

40. Kadohama, T., Nishimura, K., Hoshino, Y., Sasajima, T. & Sumpio, B. E. Effects of different types of fluid shear stress on endothelial cell proliferation and survival. *J. Cell. Physiol.* **212**, 244–251 (2007).

41. Moretti, M., Prina-Mello, A., Reid, A. J., Barron, V. & Prendergast, P. J. Endothelial cell alignment on cyclically-stretched silicone surfaces. *J. Mater. Sci. Mater. Med.* **15**, 1159–1164 (2004).

42. Frangos, J. A., Eskin, S. G., McIntire, L. V. & Ives, C. L. Flow effects on prostacyclin production by cultured human endothelial cells. *Science (80-.).* **227**, 1477–1479 (1985).

43. Wang, C., Baker, B. M., Chen, C. S. & Schwartz, M. A. Endothelial cell sensing of flow direction. *Arterioscler. Thromb. Vasc. Biol.* **33**, 2130–2136 (2013).

44. Kalucka, J. *et al.* Single-Cell Transcriptome Atlas of Murine Endothelial Cells. *Cell* **180**, 764-779.e20 (2020).

45. Chavkin, N. W. & Hirschi, K. K. Single Cell Analysis in Vascular Biology. *Front. Cardiovasc. Med.* **7**, (2020).

46. Qiu, J. & Hirschi, K. K. Endothelial cell development and its application to regenerative medicine. *Circulation Research* vol. 125 489–501 (2019).

47. Mandrycky, C., Hadland, B. & Zheng, Y. 3D curvature-instructed endothelial flow response and tissue vascularization. *Sci. Adv.* **6**, 3629–3645 (2020).

48. Nguyen, D. H. T. *et al.* Biomimetic model to reconstitute angiogenic sprouting morphogenesis in vitro. *Proc. Natl. Acad. Sci. U. S. A.* **110**, 6712–6717 (2013).

49. Song, J. W. & Munn, L. L. Fluid forces control endothelial sprouting. *Proc. Natl. Acad. Sci. U. S. A.* **108**, 15342–15347 (2011).

50. Polacheck, W. J. *et al.* A non-canonical Notch complex regulates adherens junctions and vascular barrier function. *Nature* **552**, 258 (2017).

51. Gerhardt, H. VEGF and endothelial guidance in angiogenic sprouting. *Organogenesis* **4**, 241–246 (2008).

52. Ribatti, D. & Crivellato, E. 'Sprouting angiogenesis', a reappraisal. *Dev. Biol.* **372**, 157–165 (2012).

53. Rouwkema, J. & Khademhosseini, A. Vascularization and Angiogenesis in Tissue Engineering: Beyond Creating Static Networks. *Trends Biotechnol.* **34**, 733–745 (2016).

54. Saberianpour, S. *et al.* Tissue engineering strategies for the induction of angiogenesis using biomaterials. *J. Biol. Eng.* **12**, (2018).

55. Tien, J. Microfluidic approaches for engineering vasculature. *Curr. Opin. Chem. Eng.* **3**, 36–41 (2014).

56. Kim, S., Kim, W., Lim, S. & Jeon, J. S. Vasculature-on-a-chip for in vitro disease models. *Bioengineering* **4**, (2017).

57. Chung, S., Sudo, R., Vickerman, V., Zervantonakis, I. K. & Kamm, R. D. Microfluidic platforms for studies of angiogenesis, cell migration, and cell-cell interactions: Sixth international bio-fluid mechanics symposium and workshop March 28-30, 2008 Pasadena, California. *Ann. Biomed. Eng.* **38**, 1164–1177 (2010).

58. Wong, K. H. K., Chan, J. M., Kamm, R. D. & Tien, J. Microfluidic models of vascular functions. *Annu. Rev. Biomed. Eng.* **14**, 205–230 (2012).

59. Kim, S., Chung, M., Ahn, J., Lee, S. & Jeon, N. L. Interstitial flow regulates the angiogenic response and phenotype of endothelial cells in a 3D culture model. *Lab Chip* **16**, 4189–4199 (2016).

60. Conway, D. E. *et al.* Fluid shear stress on endothelial cells modulates mechanical tension across VE-cadherin and PECAM-1. *Curr. Biol.* **23**, 1024–1030 (2013).

61. Fang, J. S. *et al.* Shear-induced Notch-Cx37-p27 axis arrests endothelial cell cycle to enable arterial specification. *Nat. Commun.* **8**, 1–14 (2017).

62. Mack, J. J. *et al.* NOTCH1 is a mechanosensor in adult arteries. *Nat. Commun.* **8**, 1620 (2017).

63. Rayner, S. G. & Zheng, Y. Engineered Microvessels for the Study of Human Disease. *J. Biomech. Eng.* **138**, (2016).

64. Griffith, L. G. & Naughton, G. Tissue engineering - Current challenges and expanding opportunities. *Science (80-.).* **295**, (2002).

65. Pober, J. S. & Sessa, W. C. Evolving functions of endothelial cells in inflammation. *Nat. Rev. Immunol.* **7**, 803–815 (2007).

66. Yau, J. W., Teoh, H. & Verma, S. Endothelial cell control of thrombosis. *BMC Cardiovasc. Disord.* **15**, (2015).

67. Rodrigues, M., Kosaric, N., Bonham, C. A. & Gurtner, G. C. Wound healing: A cellular perspective. *Physiol. Rev.* **99**, 665–706 (2019).

68. Song, H. H. G., Rumma, R. T., Ozaki, C. K., Edelman, E. R. & Chen, C. S. Vascular Tissue Engineering: Progress, Challenges, and Clinical Promise. *Cell Stem Cell* **22**, 340–354 (2018).

69. Fleischer, S., Tavakol, D. N. & Vunjak-Novakovic, G. From Arteries to Capillaries: Approaches to Engineering Human Vasculature. *Adv. Funct. Mater.* **30**, (2020).

70. Huh, D. *et al.* Reconstituting organ-level lung functions on a chip. *Science (80-.).*

328, 1662–1668 (2010).

71. Huh, D. *et al.* Microfabrication of human organs-on-chips. *Nat. Protoc.* **8**, 2135–2157 (2013).

72. Jalili-Firoozinezhad, S. *et al.* A complex human gut microbiome cultured in an anaerobic intestine-on-a-chip. *Nat. Biomed. Eng.* **3**, 520–531 (2019).

73. Musah, S. *et al.* Mature induced-pluripotent-stem-cell-derived human podocytes reconstitute kidney glomerular-capillary-wall function on a chip. *Nat. Biomed. Eng.* **1**, (2017).

74. Novak, R. *et al.* Robotic fluidic coupling and interrogation of multiple vascularized organ chips. *Nat. Biomed. Eng.* **4**, 407–420 (2020).

75. Rayner, S. G. *et al.* Reconstructing the Human Renal Vascular–Tubular Unit In Vitro. *Adv. Healthc. Mater.* **7**, 1801120 (2018).

76. Lee, A. *et al.* 3D bioprinting of collagen to rebuild components of the human heart. *Science* **365**, 482–487 (2019).

77. Heintz, K. A. *et al.* Fabrication of 3D Biomimetic Microfluidic Networks in Hydrogels. *Adv. Healthc. Mater.* **5**, 2153–2160 (2016).

78. Nguyen, D. H. T. *et al.* A biomimetic pancreatic cancer on-chip reveals endothelial ablation via ALK7 signaling. *Sci. Adv.* **5**, (2019).

79. Zheng, Y. *et al.* In vitro microvessels for the study of angiogenesis and thrombosis. *Proc. Natl. Acad. Sci. U. S. A.* **109**, 9342–9347 (2012).

80. Kotha, S. S. *et al.* Engineering a multicellular vascular niche to model hematopoietic cell trafficking. *Stem Cell Res. Ther.* **9**, (2018).

81. Redd, M. A. *et al.* Patterned human microvascular grafts enable rapid vascularization and increase perfusion in infarcted rat hearts. *Nat. Commun.* **10**, (2019).

82. Zhang, B. *et al.* Biodegradable scaffold with built-in vasculature for organ-on-a-chip engineering and direct surgical anastomosis. *Nat. Mater.* **15**, 669–678 (2016).

83. Miller, J. S. *et al.* Rapid casting of patterned vascular networks for perfusable engineered three-dimensional tissues. *Nat. Mater.* **11**, 768–774 (2012).

84. Lin, N. Y. C. *et al.* Renal reabsorption in 3D vascularized proximal tubule models. *Proc. Natl. Acad. Sci. U. S. A.* **116**, 5399–5404 (2019).

85. Arakawa, C. *et al.* Biophysical and biomolecular interactions of malaria-infected erythrocytes in engineered human capillaries. *Sci. Adv.* **6**, (2020).

86. Qiu, Y. *et al.* Microvasculature-on-a-chip for the long-term study of endothelial barrier dysfunction and microvascular obstruction in disease HHS Public Access Author manuscript. **2**, 453–463 (2018).

87. Hesh, C. A., Qiu, Y. & Lam, W. A. Vascularized microfluidics and the blood-endothelium interface. *Micromachines* vol. 11 (2020).

88. Moses, S. R., Adorno, J. J., Palmer, A. F. & Song, J. W. Vessel-on-a-chip models for studying microvascular physiology, transport, and function in vitro. *Am. J.*

Physiol. Cell Physiol. **320**, C92–C105 (2021).

89. Zheng, Y., Chen, J. & López, J. A. Flow-driven assembly of VWF fibres and webs in in vitro microvessels. *Nat. Commun.* **6**, (2015).

90. Bernabeu, M. *et al.* Binding heterogeneity of plasmodium falciparum to engineered 3d brain microvessels is mediated by EPCR and ICAM-1. *MBio* **10**, (2019).

91. Arakawa, C. *et al.* Biophysical and biomolecular interactions of malaria-infected erythrocytes in engineered human capillaries. *Sci. Adv.* **6**, (2020).

92. Palpant, N. J. *et al.* Generating high-purity cardiac and endothelial derivatives from patterned mesoderm using human pluripotent stem cells. *Nat. Protoc.* **12**, 15–31 (2017).

93. Roberts, M. A. *et al.* Stromal Cells in Dense Collagen Promote Cardiomyocyte and Microvascular Patterning in Engineered Human Heart Tissue. *Tissue Eng. Part A* **22**, 633–644 (2016).

94. Lee, C. S. & Leong, K. W. Advances in microphysiological blood-brain barrier (BBB) models towards drug delivery. *Curr. Opin. Biotechnol.* **66**, 78–87 (2020).

95. Petrosyan, A. *et al.* A glomerulus-on-a-chip to recapitulate the human glomerular filtration barrier. *Nat. Commun. 2019 101* **10**, 1–17 (2019).

96. Wilmer, M. J. *et al.* Kidney-on-a-Chip Technology for Drug-Induced Nephrotoxicity Screening. *Trends Biotechnol.* **34**, 156–170 (2016).

97. Freag, M. S. *et al.* Human Nonalcoholic Steatohepatitis on a Chip. *Hepatol.*

Commun. **5**, 217–233 (2021).

98. March, S., Hui, E. E., Underhill, G. H., Khetani, S. & Bhatia, S. N. Microenvironmental regulation of the sinusoidal endothelial cell phenotype in vitro. *Hepatology* **50**, 920–928 (2009).

99. Norona, L. M., Nguyen, D. G., Gerber, D. A., Presnell, S. C. & LeCluyse, E. L. Editor's Highlight: Modeling Compound-Induced Fibrogenesis In Vitro Using Three-Dimensional Bioprinted Human Liver Tissues. *Toxicol. Sci.* **154**, 354–367 (2016).

100. Norona, L. M. *et al.* Bioprinted liver provides early insight into the role of Kupffer cells in TGF-β1 and methotrexate-induced fibrogenesis. *PLoS One* **14**, e0208958 (2019).

101. Zamani, M., Karaca, E. & Huang, N. F. Multicellular Interactions in 3D Engineered Myocardial Tissue. *Front. Cardiovasc. Med.* **5**, 147 (2018).

102. Chen, H., Zhang, A. & Wu, J. C. Harnessing cell pluripotency for cardiovascular regenerative medicine. *Nat. Biomed. Eng. 2018 26* **2**, 392–398 (2018).

103. Blanchard, J. W. *et al.* Reconstruction of the human blood–brain barrier in vitro reveals a pathogenic mechanism of APOE4 in pericytes. *Nat. Med. 2020 266* **26**, 952–963 (2020).

104. Qian, T. *et al.* Directed differentiation of human pluripotent stem cells to blood-brain barrier endothelial cells. *Sci. Adv.* **3**, (2017).

105. Lu, T. M. *et al.* Human Induced Pluripotent Stem Cell-Derived Brain Endothelial

Cells: Current Controversies. *Front. Physiol.* **12**, 402 (2021).

106. Ligresti, G. *et al.* A novel three-dimensional human peritubular microvascular system. *J. Am. Soc. Nephrol.* **27**, 2370–2381 (2016).

107. Bovard, D. *et al.* A lung/liver-on-a-chip platform for acute and chronic toxicity studies. *Lab Chip* **18**, 3814–3829 (2018).

108. Vanlandewijck, M. *et al.* A molecular atlas of cell types and zonation in the brain vasculature. *Nature* **554**, 475–480 (2018).

109. Meng, H., Tutino, V. M., Xiang, J. & Siddiqui, A. High WSS or Low WSS? Complex Interactions of Hemodynamics with Intracranial Aneurysm Initiation, Growth, and Rupture: Toward a Unifying Hypothesis. *Am. J. Neuroradiol.* **35**, 1254–1262 (2014).

110. Davis, G. E. & Senger, D. R. Endothelial extracellular matrix: Biosynthesis, remodeling, and functions during vascular morphogenesis and neovessel stabilization. *Circ. Res.* **97**, 1093–1107 (2005).

111. Saldin, L. T., Cramer, M. C., Velankar, S. S., White, L. J. & Badylak, S. F. Extracellular matrix hydrogels from decellularized tissues: Structure and function. *Acta Biomater.* **49**, 1–15 (2017).

112. Nagao, R. J. *et al.* Decellularized Human Kidney Cortex Hydrogels Enhance Kidney Microvascular Endothelial Cell Maturation and Quiescence. *Tissue Eng. Part A* **22**, 1140–1150 (2016).

113. Williamson, A., Singh, S., Fernekorn, U. & Schober, A. The future of the patient-

specific Body-on-a-chip. *Lab Chip* **13**, 3471–3480 (2013).

114. Cochrane, A. *et al.* Advanced in vitro models of vascular biology: Human induced pluripotent stem cells and organ-on-chip technology. *Adv. Drug Deliv. Rev.* **140**, 68–77 (2019).

115. Jang, S., Collin de l'Hortet, A. & Soto-Gutierrez, A. Induced Pluripotent Stem Cell–Derived Endothelial Cells: Overview, Current Advances, Applications, and Future Directions. *Am. J. Pathol.* **189**, 502–512 (2019).

116. Wimmer, R. A. *et al.* Human blood vessel organoids as a model of diabetic vasculopathy. *Nature* **565**, 505–510 (2019).

117. Nagao, R. J. *et al.* Transforming Endothelium with Platelet-Rich Plasma in Engineered Microvessels. *Adv. Sci.* **6**, 1901725 (2019).

118. Bernabeu, M., Howard, C., Zheng, Y. & Smith, J. D. Bioengineered 3D Microvessels for Investigating Plasmodium falciparum Pathogenesis. *Trends Parasitol.* **37**, 401–413 (2021).

119. WHO. WHO World Malaria Report 2020. *Malar. Rep.* 299 (2020).

120. Taylor, T. E. *et al.* Differentiating the pathologies of cerebral malaria by postmortem parasite counts. *Nat. Med.* **10**, 143–145 (2004).

121. Miller, L. H., Baruch, D. I., Marsh, K. & Doumbo, O. K. The pathogenic basis of malaria. *Nature* **415**, 673–679 (2002).

122. Dorovini-Zis, K. *et al.* The neuropathology of fatal cerebral malaria in malawian

children. *Am. J. Pathol.* **178**, 2146–2158 (2011).

123. Seydel, K. B. *et al.* Brain swelling and death in children with cerebral malaria. *N. Engl. J. Med.* **372**, 1126–1137 (2015).

124. Smith, J. D., Rowe, J. A., Higgins, M. K. & Lavstsen, T. Malaria's deadly grip: cytoadhesion of Plasmodium falciparum-infected erythrocytes. *Cell. Microbiol.* **15**, 1976–1983 (2013).

125. Turner, L. *et al.* Severe malaria is associated with parasite binding to endothelial protein C receptor. *Nat. 2013 4987455* **498**, 502–505 (2013).

126. Kessler, A. *et al.* Linking EPCR-Binding PfEMP1 to Brain Swelling in Pediatric Cerebral Malaria. *Cell Host Microbe* **22**, 601-614.e5 (2017).

127. Lennartz, F. *et al.* Structure-Guided Identification of a Family of Dual Receptor-Binding PfEMP1 that Is Associated with Cerebral Malaria. *Cell Host Microbe* **21**, 403–414 (2017).

128. Storm, J. *et al.* Cerebral malaria is associated with differential cytoadherence to brain endothelial cells. *EMBO Mol. Med.* **11**, (2019).

129. Turner, G. D. H. *et al.* Systemic endothelial activation occurs in both mild and severe malaria. Correlating dermal microvascular endothelial cell phenotype and soluble cell adhesion molecules with disease severity. *Am. J. Pathol.* **152**, 1477 (1998).

130. Tripathi, A. K., Sullivan, D. J. & Stins, M. F. Plasmodium falciparum-Infected

Erythrocytes Increase Intercellular Adhesion Molecule 1 Expression on Brain Endothelium through NF-κB. *Infect. Immun.* **74**, 3262 (2006).

131. Gillrie, M. R. *et al.* Diverse functional outcomes of Plasmodium falciparum ligation of EPCR: potential implications for malarial pathogenesis. *Cell. Microbiol.* **17**, 1883–1899 (2015).

132. Bouwens, E. A. M., Stavenuiter, F. & Mosnier, L. O. Mechanisms of anticoagulant and cytoprotective actions of the protein C pathway. *J. Thromb. Haemost.* **11 Suppl 1**, 242–253 (2013).

133. Mantel, P. Y. *et al.* Infected erythrocyte-derived extracellular vesicles alter vascular function via regulatory Ago2-miRNA complexes in malaria. *Nat. Commun. 2016 71* **7**, 1–15 (2016).

134. Moxon, C. A. *et al.* Parasite histones are toxic to brain endothelium and link blood barrier breakdown and thrombosis in cerebral malaria. *Blood Adv.* **4**, 2851–2864 (2020).

135. Pal, P. *et al.* Plasmodium falciparum histidine-rich protein II compromises brain endothelial barriers and may promote cerebral malaria pathogenesis. *MBio* **7**, (2016).

136. Kwiatkowski, D. *et al.* TNF concentration in fatal cerebral, non-fatal cerebral, and uncomplicated Plasmodium falciparum malaria. *Lancet (London, England)* **336**, 1201–1204 (1990).

137. Vanderberg, J. P. & Frevert, U. Intravital microscopy demonstrating antibody-mediated immobilisation of Plasmodium berghei sporozoites injected into skin by mosquitoes. *Int. J. Parasitol.* **34**, 991–996 (2004).

138. Tavares, J. *et al.* Role of host cell traversal by the malaria sporozoite during liver infection. *J. Exp. Med.* **210**, 905–915 (2013).

139. Burda, P. C., Caldelari, R. & Heussler, V. T. Manipulation of the Host Cell Membrane during Plasmodium Liver Stage Egress. *MBio* **8**, (2017).

140. Sturm, A. *et al.* Manipulation of host hepatocytes by the malaria parasite for delivery into liver sinusoids. *Science (80-.).* **313**, 1287–1290 (2006).

141. Baer, K., Klotz, C., Kappe, S. H. I., Schnieder, T. & Frevert, U. Release of hepatic Plasmodium yoelii merozoites into the pulmonary microvasculature. *PLoS Pathog.* **3**, 1651–1668 (2007).

142. Venugopal, K., Hentzschel, F., Valkiūnas, G. & Marti, M. Plasmodium asexual growth and sexual development in the haematopoietic niche of the host. *Nat. Rev. Microbiol.* **18**, 177–189 (2020).

143. Andrade, C. M. *et al.* Increased circulation time of Plasmodium falciparum underlies persistent asymptomatic infection in the dry season. *Nat. Med.* **26**, 1929–1940 (2020).

144. Topper, J. N. & Gimbrone, M. A. Blood flow and vascular gene expression: Fluid shear stress as a modulator of endothelial phenotype. *Mol. Med. Today* **5**, 40–46

(1999).

145. Marti, M., Good, R. T., Rug, M., Knuepfer, E. & Cowman, A. F. Targeting malaria virulence and remodeling proteins to the host erythrocyte. *Science (80-.).* **306**, 1930–1933 (2004).

146. Hiller, N. L. *et al.* A host-targeting signal in virulence proteins reveals a secretome in malarial infection. *Science (80-.).* **306**, 1934–1937 (2004).

147. Maier, A. G. *et al.* Exported Proteins Required for Virulence and Rigidity of Plasmodium falciparum-Infected Human Erythrocytes. *Cell* **134**, 48–61 (2008).

148. Smith, J. D. The role of PfEMP1 adhesion domain classification in Plasmodium falciparum pathogenesis research. *Mol. Biochem. Parasitol.* **195**, 82–87 (2014).

149. Barnwell, J. W. *et al.* A human 88-kD membrane glycoprotein (CD36) functions in vitro as a receptor for a cytoadherence ligand on Plasmodium falciparum-infected erythrocytes. *J. Clin. Invest.* **84**, 765–772 (1989).

150. Hsieh, F. L. *et al.* The structural basis for CD36 binding by the malaria parasite. *Nat. Commun.* **7**, (2016).

151. Lau, C. K. Y. *et al.* Structural conservation despite huge sequence diversity allows EPCR binding by the pfemp1 family implicated in severe childhood malaria. *Cell Host Microbe* **17**, 118–129 (2015).

152. Turner, L. *et al.* Severe malaria is associated with parasite binding to endothelial protein C receptor. *Nature* **498**, 502–505 (2013).

153. Ockenhouse, C. F., Betageri, R., Springer, T. A. & Staunton, D. E. Plasmodium falciparum-infected erythrocytes bind ICAM-1 at a site distinct from LFA-1, Mac-1, and human rhinovirus. *Cell* **68**, 63–69 (1992).

154. Brazier, A. J., Avril, M., Bernabeu, M., Benjamin, M. & Smith, J. D. Pathogenicity Determinants of the Human Malaria Parasite Plasmodium falciparum Have Ancient Origins. *mSphere* **2**, (2017).

155. Bernabeu, M. *et al.* Severe adult malaria is associated with specific PfEMP1 adhesion types and high parasite biomass. *Proc. Natl. Acad. Sci. U. S. A.* **113**, E3270–E3279 (2016).

156. Lavstsen, T. *et al.* Plasmodium falciparum erythrocyte membrane protein 1 domain cassettes 8 and 13 are associated with severe malaria in children. *Proc. Natl. Acad. Sci. U. S. A.* **109**, (2012).

157. Kessler, A. *et al.* Linking EPCR-Binding PfEMP1 to Brain Swelling in Pediatric Cerebral Malaria. *Cell Host Microbe* **22**, 601-614.e5 (2017).

158. Mehta, D. & Malik, A. B. Signaling mechanisms regulating endothelial permeability. *Physiol. Rev.* **86**, 279–367 (2006).

159. Tripathi, A. K., Sullivan, D. J. & Stins, M. F. Plasmodium falciparum-infected erythrocytes decrease the integrity of human blood-brain barrier endothelial cell monolayers. *J. Infect. Dis.* **195**, 942–950 (2007).

160. Gillrie, M. R. & Ho, M. Dynamic interactions of Plasmodium spp. with vascular

endothelium. *Tissue Barriers* **5**, (2017).

161. Bernabeu, M. & Smith, J. D. EPCR and Malaria Severity: The Center of a Perfect Storm. *Trends Parasitol.* **33**, 295–308 (2017).

162. Avril, M., Benjamin, M., Dols, M. M. & Smith, J. D. Interplay of Plasmodium falciparum and thrombin in brain endothelial barrier disruption. *Sci. Rep.* **9**, (2019).

163. Craig, A. G., Storm, J., Wu, Y., Davies, J. & Moxon, C. A. Testing the effect of PAR1 inhibitors on Plasmodium falciparum-induced loss of endothelial cell barrier function. *Wellcome open Res.* **5**, (2020).

164. Zhao, Z., Nelson, A. R., Betsholtz, C. & Zlokovic, B. V. Establishment and Dysfunction of the Blood-Brain Barrier. *Cell* **163**, 1064–1078 (2015).

165. Lindahl, P., Johansson, B. R., Levéen, P. & Betsholtz, C. Pericyte loss and microaneurysm formation in PDGF-B-deficient mice. *Science* **277**, 242–245 (1997).

166. Abbott, N. J., Rönnbäck, L. & Hansson, E. Astrocyte-endothelial interactions at the blood-brain barrier. *Nat. Rev. Neurosci.* **7**, 41–53 (2006).

167. Noumbissi, M. E., Galasso, B. & Stins, M. F. Brain vascular heterogeneity: implications for disease pathogenesis and design of in vitro blood-brain barrier models. *Fluids Barriers CNS* **15**, (2018).

168. Mohanty, S. *et al.* Magnetic Resonance Imaging of Cerebral Malaria Patients Reveals Distinct Pathogenetic Processes in Different Parts of the Brain. *mSphere* **2**, (2017).

169. Potchen, M. J. *et al.* 1.5 tesla magnetic resonance imaging to investigate potential etiologies of brain swelling in pediatric cerebral malaria. *Am. J. Trop. Med. Hyg.* **98**, 497–504 (2018).

170. Sahu, P. K. *et al.* Brain Magnetic Resonance Imaging Reveals Different Courses of Disease in Pediatric and Adult Cerebral Malaria. *Clin. Infect. Dis.* **73**, e2387–e2396 (2021).

171. Maude, R. J. *et al.* Magnetic resonance imaging of the brain in adults with severe falciparum malaria. *Malar. J.* **13**, (2014).

172. Dorovini-Zis, K. *et al.* The neuropathology of fatal cerebral malaria in Malawian children. *Am. J. Pathol.* **178**, 2146–2158 (2011).

173. Taylor, T. E. *et al.* Differentiating the pathologies of cerebral malaria by postmortem parasite counts. *Nat. Med.* **10**, 143–145 (2004).

174. SPITZ, S. The pathology of acute falciparum malaria. *Mil. Surg.* **99**, 555–572 (1946).

175. Vera, I. M. *et al.* Plasma cell-free DNA predicts pediatric cerebral malaria severity. *JCI insight* **5**, (2020).

176. Milner, D. A. *et al.* Quantitative assessment of multiorgan sequestration of parasites in fatal pediatric cerebral malaria. *J. Infect. Dis.* **212**, 1317–1321 (2015).

177. Barrera, V. *et al.* Neurovascular sequestration in paediatric P. Falciparum malaria is visible clinically in the retina. *Elife* **7**, (2018).

178. Maccormick, I. J. C. *et al.* Cerebral malaria in children: Using the retina to study the brain. *Brain* **137**, 2119–2142 (2014).

179. Hochman, S. E. *et al.* Fatal pediatric cerebral malaria is associated with intravascular monocytes and platelets that are increased with HIV coinfection. *MBio* **6**, (2015).

180. Grau, G. E. *et al.* Platelet accumulation in brain microvessels in fatal pediatric cerebral malaria. *J. Infect. Dis.* **187**, 461–466 (2003).

181. Grau, G. E. *et al.* Tumor necrosis factor and disease severity in children with falciparum malaria. *N. Engl. J. Med.* **320**, 1586–1591 (1989).

182. Garraud, O., Hamzeh-Cognasse, H. & Cognasse, F. Platelets and cytokines: How and why? *Transfus. Clin. Biol.* **19**, 104–108 (2012).

183. McMorran, B. J. *et al.* Platelet factor 4 and duffy antigen required for platelet killing of Plasmodium falciparum. *Science (80-.).* **338**, 1348–1351 (2012).

184. Wassmer, S. C. *et al.* Platelets reorient Plasmodium falciparum-infected erythrocyte cytoadhesion to activated endothelial cells. *J. Infect. Dis.* **189**, 180–189 (2004).

185. Chotivanich, K. *et al.* Platelet-induced autoagglutination of Plasmodium falciparum-infected red blood cells and disease severity in Thailand. *J. Infect. Dis.* **189**, 1052–1055 (2004).

186. Bridges, D. J. *et al.* Rapid activation of endothelial cells enables Plasmodium falciparum adhesion to platelet-decorated von Willebrand factor strings. *Blood* **115**,

1472–1474 (2010).

187. Milner, D. A. *et al.* The systemic pathology of cerebral malaria in African children. *Front. Cell. Infect. Microbiol.* **4**, (2014).

188. Avril, M. *et al.* A restricted subset of var genes mediates adherence of Plasmodium falciparum-infected erythrocytes to brain endothelial cells. *Proc. Natl. Acad. Sci. U. S. A.* **109**, (2012).

189. Claessens, A. *et al.* A subset of group A-like var genes encodes the malaria parasite ligands for binding to human brain endothelial cells. *Proc. Natl. Acad. Sci. U. S. A.* **109**, (2012).

190. Udeinya, I. J., Schmidt, J. A., Aikawa, M., Miller, L. H. & Green, I. Falciparum malaria-infected erythrocytes specifically bind to cultured human endothelial cells. *Science (80-.).* **213**, 555–557 (1981).

191. Berendt, A. R., Simmons, D. L., Tansey, J., Newbold, C. I. & Marsh, K. Intercellular adhesion molecule-1 is an endothelial cell adhesion receptor for Plasmodium falciparum. *Nature* **341**, 57–59 (1989).

192. Avril, M., Brazier, A. J., Melcher, M., Sampath, S. & Smith, J. D. DC8 and DC13 var Genes Associated with Severe Malaria Bind Avidly to Diverse Endothelial Cells. *PLoS Pathog.* **9**, (2013).

193. Cooke, B. M. *et al.* Rolling and stationary cytoadhesion of red blood cells parasitized by Plasmodium falciparum: Separate roles for ICAM-1, CD36 and

thrombospondin. *Br. J. Haematol.* **87**, 162–170 (1994).

194. Wick, T. M. & Louis, V. Cytoadherence of Plasmodium falciparum-infected erythrocytes to human umbilical vein and human dermal microvascular endothelial cells under shear conditions. *Am. J. Trop. Med. Hyg.* **45**, 578–586 (1991).

195. Chen, X. *et al.* Prevascularization of a fibrin-based tissue construct accelerates the formation of functional anastomosis with host vasculature. *Tissue Eng. - Part A* **15**, 1363–1371 (2009).

196. Whisler, J. A., Chen, M. B. & Kamm, R. D. Control of perfusable microvascular network morphology using a multiculture microfluidic system. *Tissue Eng. - Part C Methods* **20**, 543–552 (2014).

197. Collen, A. *et al.* Membrane-type matrix metalloproteinase-mediated angiogenesis in a fibrin-collagen matrix. *Blood* **101**, 1810–1817 (2003).

198. Depond, M., Henry, B., Buffet, P. & Ndour, P. A. Methods to Investigate the Deformability of RBC During Malaria. *Front. Physiol.* **10**, (2020).

199. Barker, K. R. *et al.* miR-155 modifies inflammation, endothelial activation and blood-brain barrier dysfunction in cerebral malaria. *Mol. Med.* **23**, 24–33 (2017).

200. Raghavan, S., Nelson, C. M., Baranski, J. D., Lim, E. & Chen, C. S. Geometrically controlled endothelial tubulogenesis in micropatterned gels. *Tissue Eng. - Part A* **16**, 2255–2263 (2010).

201. Kinstlinger, I. S. *et al.* Generation of model tissues with dendritic vascular networks

via sacrificial laser-sintered carbohydrate templates. *Nat. Biomed. Eng.* **4**, 916–932 (2020).

202. Kolesky, D. B. *et al.* 3D bioprinting of vascularized, heterogeneous cell-laden tissue constructs. *Adv. Mater.* **26**, 3124–3130 (2014).

203. Campisi, M. *et al.* 3D self-organized microvascular model of the human blood-brain barrier with endothelial cells, pericytes and astrocytes. *Biomaterials* **180**, 117–129 (2018).

204. Park, T. E. *et al.* Hypoxia-enhanced Blood-Brain Barrier Chip recapitulates human barrier function and shuttling of drugs and antibodies. *Nat. Commun.* **10**, (2019).

205. Bouhrira, N. *et al.* Disturbed flow disrupts the blood-brain barrier in a 3D bifurcation model. *Biofabrication* **12**, (2020).

206. Merkel, K. H. H., Ginsberg, P. L., Parker, J. C. & Post, M. J. D. Cerebrovascular disease in sickle cell anemia: A clinical, pathological and radiological correlation. *Stroke* **9**, 45–52 (1978).

207. Buys, A. V. *et al.* Changes in red blood cell membrane structure in type 2 diabetes: A scanning electron and atomic force microscopy study. *Cardiovasc. Diabetol.* **12**, (2013).

208. Chiodini, J. Apps from the World Health Organization – The World Malaria Report and more. *Travel Med. Infect. Dis.* **22**, 82–84 (2018).

209. White, N. J., Turner, G. D. H., Day, N. P. J. & Dondorp, A. M. Lethal Malaria:

Marchiafava and Bignami Were Right. *J. Infect. Dis.* **208**, 192–198 (2013).

210. Kilejian, A. Characterization of a protein correlated with the production of knob-like protrusions on membranes of erythrocytes infected with Plasmodium falciparum. *Proc. Natl. Acad. Sci. U. S. A.* **76**, 4650–4653 (1979).

211. Zhang, Y. *et al.* Multiple stiffening effects of nanoscale knobs on human red blood cells infected with Plasmodium falciparum malaria parasite. *Proc. Natl. Acad. Sci. U. S. A.* **112**, 6068–6073 (2015).

212. Baruch, D. I. *et al.* Cloning the P. falciparum gene encoding PfEMP1, a malarial variant antigen and adherence receptor on the surface of parasitized human erythrocytes. *Cell* **82**, 77–87 (1995).

213. Crabb, B. S. *et al.* Targeted gene disruption shows that knobs enable malaria-infected red cells to cytoadhere under physiological shear stress. *Cell* **89**, 287–296 (1997).

214. David, P. H., Hommel, M., Miller, L. H., Udeinya, I. J. & Oligino, L. D. Parasite sequestration in Plasmodium falciparum malaria: Spleen and antibody modulation of cytoadherence of infected erythrocytes. *Proc. Natl. Acad. Sci. U. S. A.* **80**, 5075–5079 (1983).

215. Dondorp, A. M. *et al.* Prognostic significance of reduced red blood cell deformability in severe falciparum malaria. *Am. J. Trop. Med. Hyg.* **57**, 507–511 (1997).

216. Raventos-Suarez, C., Kaul, D. K., Macaluso, F. & Nagel, R. L. Membrane knobs

are required for the microcirculatory obstruction induced by Plasmodium falciparum-infected erythrocytes. *Proc. Natl. Acad. Sci. U. S. A.* **82**, 3829–3833 (1985).

217. Smith, J. D. *et al.* Switches in expression of plasmodium falciparum var genes correlate with changes in antigenic and cytoadherent phenotypes of infected erythrocytes. *Cell* **82**, 101–110 (1995).

218. Dondorp, A. M. *et al.* Artesunate versus quinine in the treatment of severe falciparum malaria in African children (AQUAMAT): An open-label, randomised trial. *Lancet* **376**, 1647–1657 (2010).

219. Miller, L. H. Distribution of mature trophozoites and schizonts of Plasmodium falciparum in the organs of Aotus trivirgatus, the night monkey. *Am. J. Trop. Med. Hyg.* **18**, 860–865 (1969).

220. Skalak, R. & Branemark, P. I. Deformation of red blood cells in capillaries. *Science (80-.).* **164**, 717–719 (1969).

221. Shelby, J. P., White, J., Ganesan, K., Rathod, P. K. & Chiu, D. T. A microfluidic model for single-cell capillary obstruction by Plasmodium falciparum-infected erythrocytes. *Proc. Natl. Acad. Sci. U. S. A.* **100**, 14618–14622 (2003).

222. Tsukada, K., Sekizuka, E., Oshio, C. & Minamitani, H. Direct measurement of erythrocyte deformability in diabetes mellitus with a transparent microchannel capillary model and high-speed video camera system. *Microvasc. Res.* **61**, 231–239 (2001).

223. Higgins, J. M., Eddington, D. T., Bhatia, S. N. & Mahadevan, L. Sickle cell vasoocclusion and rescue in a microfluidic device. *Proc. Natl. Acad. Sci. U. S. A.* **104**, 20496–20500 (2007).

224. Noguchi, H. & Gompper, G. Shape transitions of fluid vesicles and red blood cells in capillary flows. *Proc. Natl. Acad. Sci. U. S. A.* **102**, 14159–14164 (2005).

225. Herricks, T., Seydel, K. B., Molyneux, M., Taylor, T. & Rathod, P. K. Estimating physical splenic filtration of Plasmodium falciparum-infected red blood cells in malaria patients. *Cell. Microbiol.* **14**, 1880–1891 (2012).

226. Keller, T. T. *et al.* Infections and endothelial cells. *Cardiovasc. Res.* **60**, 40–48 (2003).

227. Yalcin, O., Jani, V. P., Johnson, P. C. & Cabrales, P. Implications enzymatic degradation of the endothelial glycocalyx on the microvascular hemodynamics and the arteriolar red cell free layer of the rat cremaster muscle. *Front. Physiol.* **9**, (2018).

228. Yipp, B. G. *et al.* Synergism of multiple adhesion molecules in mediating cytoadherence of Plasmodium falciparum-infected erythrocytes to microvascular endothelial cells under flow. *Blood* **96**, 2292–2298 (2000).

229. Gillrie, M. R. *et al.* Diverse functional outcomes of Plasmodium falciparum ligation of EPCR: Potential implications for malarial pathogenesis. *Cell. Microbiol.* **17**, 1883–1899 (2015).

230. Zheng, Y. *et al.* In vitro microvessels for the study of angiogenesis and thrombosis. *Proc. Natl. Acad. Sci. U. S. A.* **109**, 9342–9347 (2012).

231. Arakawa, C. K. *et al.* Multicellular Vascularized Engineered Tissues through User-Programmable Biomaterial Photodegradation. *Adv. Mater.* **29**, 1703156 (2017).

232. Escaned, J. *et al.* Assessment of microcirculatory remodeling with intracoronary flow velocity and pressure measurements: Validation with endomyocardial sampling in cardiac allografts. *Circulation* **120**, 1561–1568 (2009).

233. Hudetz, A. G. Blood flow in the cerebral capillary network: A review emphasizing observations with intravital microscopy. *Microcirculation* **4**, 233–252 (1997).

234. Secomb, T. W. Blood Flow in the Microcirculation. *Annu. Rev. Fluid Mech.* **49**, 443–461 (2017).

235. Kleinfeld, D., Mitra, P. P., Helmchen, F. & Denk, W. Fluctuations and stimulus-induced changes in blood flow observed in individual capillaries in layers 2 through 4 of rat neocortex. *Proc. Natl. Acad. Sci. U. S. A.* **95**, 15741–15746 (1998).

236. Mauer, J. *et al.* Flow-Induced Transitions of Red Blood Cell Shapes under Shear. *Phys. Rev. Lett.* **121**, (2018).

237. Lanotte, L. *et al.* Red cells' dynamic morphologies govern blood shear thinning under microcirculatory flow conditions. *Proc. Natl. Acad. Sci. U. S. A.* **113**, 13289–13294 (2016).

238. Hanssen, E. *et al.* Soft X-ray microscopy analysis of cell volume and hemoglobin

content in erythrocytes infected with asexual and sexual stages of Plasmodium falciparum. *J. Struct. Biol.* **177**, 224–232 (2012).

239. Horrocks, P., Pinches, R., Christodoulou, Z., Kyes, S. A. & Newbold, C. I. Variable var transition rates underlie antigenic variation in malaria. *Proc. Natl. Acad. Sci. U. S. A.* **101**, 11129–11134 (2004).

240. Yipp, B. G. *et al.* Differential roles of CD36, ICAM-1, and p-selectin in Plasmodium falciparum cytoadherence in vivo. *Microcirculation* **14**, 593–602 (2007).

241. Hou, H. W. *et al.* Deformability based cell margination - A simple microfluidic design for malaria-infected erythrocyte separation. *Lab Chip* **10**, 2605–2613 (2010).

242. Imai, Y. *et al.* Margination of red blood cells infected by Plasmodium falciparum in a microvessel. *J. Biomech.* **44**, 1553–1558 (2011).

243. Jambou, R. *et al.* Plasmodium falciparum adhesion on human brain microvascular endothelial cells involves transmigration-like cup formation and induces opening of intercellular junctions. *PLoS Pathog.* **6**, 1–13 (2010).

244. Hutchings, C. L. *et al.* New insights into the altered adhesive and mechanical properties of red blood cells parasitized by Babesia bovis. *Mol. Microbiol.* **65**, 1092–1105 (2007).

245. Langreth, S. G. & Peterson, E. Pathogenicity, stability, and immunogenicity of a knobless clone of Plasmodium falciparum in Colombian owl monkeys. *Infect. Immun.* **47**, 760–766 (1985).

246. Glenister, F. K., Coppel, R. L., Cowman, A. F., Mohandas, N. & Cooke, B. M. Contribution of parasite proteins to altered mechanical properties of malaria-infected red blood cells. *Blood* **99**, 1060–1063 (2002).

247. Chen, L. T. & Weiss, L. The role of the sinus wall in the passage of erythrocytes through the spleen. *Blood* **41**, 529–537 (1973).

248. Rigat-Brugarolas, L. G. *et al.* A functional microengineered model of the human splenon-on-a-chip. *Lab Chip* **14**, 1715–1724 (2014).

249. Sanchez, C. P. *et al.* Single-molecule imaging and quantification of the immune-variant adhesin VAR2CSA on knobs of Plasmodium falciparum-infected erythrocytes. *Commun. Biol.* **2**, (2019).

250. Lou, J., Lucas, R. & Grau, G. E. Pathogenesis of cerebral malaria: Recent experimental data and possible applications for humans. *Clin. Microbiol. Rev.* **14**, 810–820 (2001).

251. Duffy, F. *et al.* Meta-analysis of plasmodium falciparum var signatures contributing to severe Malaria in African children and Indian adults. *MBio* **10**, (2019).

252. Quadt, K. A. *et al.* The Density of Knobs on Plasmodium falciparum-Infected Erythrocytes Depends on Developmental Age and Varies among Isolates. *PLoS One* **7**, (2012).

253. Lee, H. J. *et al.* Integrated pathogen load and dual transcriptome analysis of systemic host-pathogen interactions in severe malaria. *Sci. Transl. Med.* **10**, (2018).

254. Janes, J. H. *et al.* Investigating the host binding signature on the Plasmodium falciparum PfEMP1 protein family. *PLoS Pathog.* **7**, (2011).

255. Rayner, S. G. *et al.* Multiphoton-Guided Creation of Complex Organ-Specific Microvasculature. *Adv. Healthc. Mater.* **10**, (2021).

256. Bhatia, S. N. & Ingber, D. E. Microfluidic organs-on-chips. *Nat. Biotechnol.* **32**, 760–772 (2014).

257. Marx, V. Tissue engineering: Organs from the lab. *Nature* **522**, 373–377 (2015).

258. Lewis, M. C., MacArthur, B. D., Malda, J., Pettet, G. & Please, C. P. Heterogeneous proliferation within engineered cartilaginous tissue: the role of oxygen tension. *Biotechnol. Bioeng.* **91**, 607–615 (2005).

259. Rakusan, K., Flanagan, M. F., Geva, T., Southern, J. & Van Praagh, R. Morphometry of human coronary capillaries during normal growth and the effect of age in left ventricular pressure-overload hypertrophy. *Circulation* **86**, 38–46 (1992).

260. Neal, C. R. *et al.* Novel hemodynamic structures in the human glomerulus. *Am. J. Physiol. Renal Physiol.* **315**, F1370–F1384 (2018).

261. Chrobak, K. M., Potter, D. R. & Tien, J. Formation of perfused, functional microvascular tubes in vitro. *Microvasc. Res.* **71**, 185–196 (2006).

262. Kolesky, D. B., Homan, K. A., Skylar-Scott, M. A. & Lewis, J. A. Three-dimensional bioprinting of thick vascularized tissues. *Proc. Natl. Acad. Sci. U. S. A.* **113**, 3179–3184 (2016).

263. Grigoryan, B. *et al.* Multivascular networks and functional intravascular topologies within biocompatible hydrogels. *Science* **364**, 458–464 (2019).

264. Ilina, O., Bakker, G. J., Vasaturo, A., Hofmann, R. M. & Friedl, P. Two-photon laser-generated microtracks in 3D collagen lattices: principles of MMP-dependent and -independent collective cancer cell invasion. *Phys. Biol.* **8**, (2011).

265. Brandenberg, N. & Lutolf, M. P. In Situ Patterning of Microfluidic Networks in 3D Cell-Laden Hydrogels. *Adv. Mater.* **28**, 7450–7456 (2016).

266. Applegate, M. B. *et al.* Laser-based three-dimensional multiscale micropatterning of biocompatible hydrogels for customized tissue engineering scaffolds. *Proc. Natl. Acad. Sci. U. S. A.* **112**, 12052–12057 (2015).

267. Kloxin, A. M., Kasko, A. M., Salinas, C. N. & Anseth, K. S. Photodegradable hydrogels for dynamic tuning of physical and chemical properties. *Science* **324**, 59–63 (2009).

268. DeForest, C. A. & Anseth, K. S. Cytocompatible click-based hydrogels with dynamically tunable properties through orthogonal photoconjugation and photocleavage reactions. *Nat. Chem.* **3**, 925–931 (2011).

269. Pradhan, S. *et al.* Biofabrication Strategies and Engineered In Vitro Systems for Vascular Mechanobiology. *Adv. Healthc. Mater.* **9**, 1901255 (2020).

270. Sarig-Nadir, O., Livnat, N., Zajdman, R., Shoham, S. & Seliktar, D. Laser photoablation of guidance microchannels into hydrogels directs cell growth in three

dimensions. *Biophys. J.* **96**, 4743–4752 (2009).

271. Culver, J. C. *et al.* Three-dimensional biomimetic patterning in hydrogels to guide cellular organization. *Adv. Mater.* **24**, 2344–2348 (2012).

272. Lavender, M. D., Pang, Z., Wallace, C. S., Niklason, L. E. & Truskey, G. A. A system for the direct co-culture of endothelium on smooth muscle cells. *Biomaterials* **26**, 4642–4653 (2005).

273. Raub, C. B., Putnam, A. J., Tromberg, B. J. & George, S. C. Predicting bulk mechanical properties of cellularized collagen gels using multiphoton microscopy. *Acta Biomater.* **6**, 4657–4665 (2010).

274. Liu, J., Zheng, H., Poh, P. S. P., Machens, H. G. & Schilling, A. F. Hydrogels for Engineering of Perfusable Vascular Networks. *Int. J. Mol. Sci.* **16**, 15997–16016 (2015).

275. Cross, V. L. *et al.* Dense type I collagen matrices that support cellular remodeling and microfabrication for studies of tumor angiogenesis and vasculogenesis in vitro. *Biomaterials* **31**, 8596–8607 (2010).

276. Holtmaat, A. *et al.* Long-term, high-resolution imaging in the mouse neocortex through a chronic cranial window. *Nat. Protoc.* **4**, 1128–1144 (2009).

277. Moxon, C. A., Gibbins, M. P., McGuinness, D., Milner, D. A. & Marti, M. New Insights into Malaria Pathogenesis. *https://doi.org/10.1146/annurev-pathmechdis-012419-032640* **15**, 315–343 (2020).

278. Dorovini-Zis, K. *et al.* The neuropathology of fatal cerebral malaria in Malawian children. *Am. J. Pathol.* **178**, 2146–2158 (2011).

279. Seydel, K. B. *et al.* Brain swelling and death in children with cerebral malaria. *N. Engl. J. Med.* **372**, 1126–1137 (2015).

280. Milner, D. A. *et al.* The systemic pathology of cerebral malaria in African children. *Front. Cell. Infect. Microbiol.* **4**, (2014).

281. Hermsen, C. C. *et al.* Circulating concentrations of soluble granzyme A and B increase during natural and experimental Plasmodium falciparum infections. *Clin. Exp. Immunol.* **132**, 467–472 (2003).

282. Wilson, N. O. *et al.* CXCL4 and CXCL10 predict risk of fatal cerebral malaria. *Dis. Markers* **30**, 39–49 (2011).

283. Moxon, C. A. *et al.* Loss of endothelial protein C receptors links coagulation and inflammation to parasite sequestration in cerebral malaria in African children. *Blood* **122**, 842–851 (2013).

284. Petersen, J. E. V. *et al.* Protein C system defects inflicted by the malaria parasite protein PfEMP1 can be overcome by a soluble EPCR variant. *Thromb. Haemost.* **114**, 1038–1048 (2015).

285. Tripathi, A. K., Sha, W., Shulaev, V., Stins, M. F. & Sullivan, D. J. Plasmodium falciparum–infected erythrocytes induce NF-κB regulated inflammatory pathways in human cerebral endothelium. *Blood* **114**, 4243–4252 (2009).

286. Buffet, P. A. *et al.* The pathogenesis of Plasmodium falciparum malaria in humans: insights from splenic physiology. *Blood* **117**, 381–392 (2011).

287. Gillrie, M. R. *et al.* Thrombin Cleavage of Plasmodium falciparum Erythrocyte Membrane Protein 1 Inhibits Cytoadherence. *MBio* **7**, (2016).

288. Essone, J. C. B. B. *et al.* Comparison of apoptosis in human primary pulmonary endothelial cells and a brain microvascular endothelial cell line co-cultured with Plasmodium falciparum field isolates. *BMC Infect. Dis.* **17**, 1–10 (2017).

289. Touré, F. S. *et al.* Apoptosis: a potential triggering mechanism of neurological manifestation in Plasmodium falciparum malaria. *Parasite Immunol.* **30**, 47–51 (2008).

290. N'Dilimabaka, N. *et al.* P. falciparum isolate-specific distinct patterns of induced apoptosis in pulmonary and brain endothelial cells. *PLoS One* **9**, (2014).

291. Punsawad, C., Maneerat, Y., Chaisri, U., Nantavisai, K. & Viriyavejakul, P. Nuclear factor kappa B modulates apoptosis in the brain endothelial cells and intravascular leukocytes of fatal cerebral malaria. *Malar. J.* **12**, (2013).

292. Hochman, S. E. *et al.* Fatal pediatric cerebral malaria is associated with intravascular monocytes and platelets that are increased with HIV coinfection. *MBio* **6**, (2015).

293. Curtis, A. M. *et al.* Endothelial microparticles: Sophisticated vesicles modulating vascular function. *Vasc. Med. (United Kingdom)* **18**, 204–214 (2013).

294. Combes, V. *et al.* Circulating Endothelial Microparticles in Malawian Children With Severe Falciparum Malaria Complicated With Coma. *JAMA* **291**, 2542–2544 (2004).

295. Min, J.-K. *et al.* TNF-related activation-induced cytokine enhances leukocyte adhesiveness: induction of ICAM-1 and VCAM-1 via TNF receptor-associated factor and protein kinase C-dependent NF-kappaB activation in endothelial cells. *J. Immunol.* **175**, 531–540 (2005).

296. Stins, M. F., Gilles, F. & Kim, K. S. Selective expression of adhesion molecules on human brain microvascular endothelial cells. *J. Neuroimmunol.* **76**, 81–90 (1997).

297. Marcos-Ramiro, B., García-Weber, D. & Millán, J. TNF-induced endothelial barrier disruption: Beyond actin and Rho. *Thromb. Haemost.* **112**, 1088–1102 (2014).

298. Chakravorty, S. J. *et al.* Altered phenotype and gene transcription in endothelial cells, induced by Plasmodium falciparum-infected red blood cells: Pathogenic or protective? *Int. J. Parasitol.* **37**, 975–987 (2007).

299. Erwig, L. P. & Henson, P. M. Clearance of apoptotic cells by phagocytes. *Cell Death Differ.* **15**, 243–250 (2008).

300. Zheng, Y. *et al.* In vitro microvessels for the study of angiogenesis and thrombosis. *Proc. Natl. Acad. Sci. U. S. A.* **109**, 9342–7 (2012).